Design Feasibility of a Deployable Membrane Reflectarray Antenna for Space Applications

Niels Donners

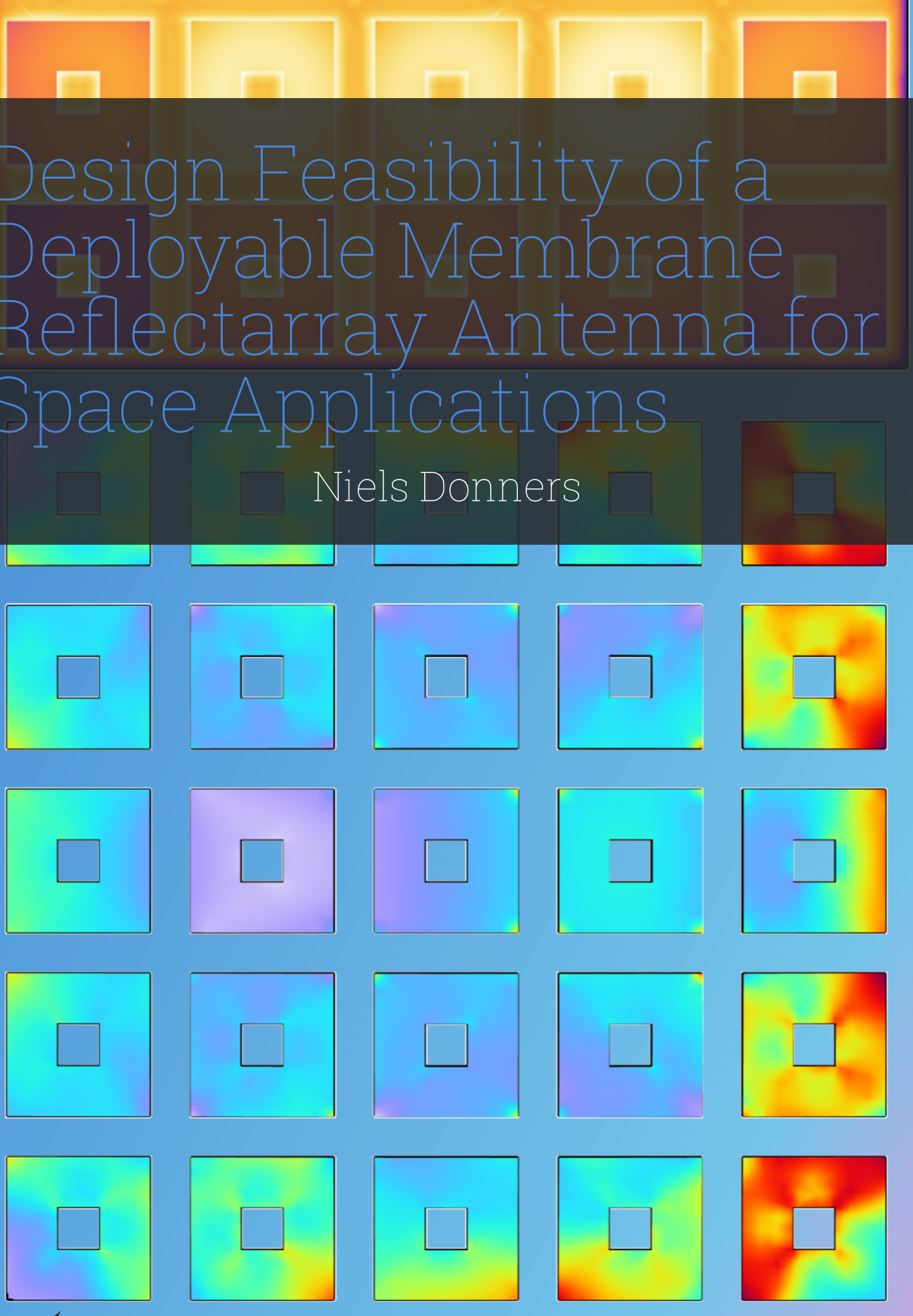

Delft University of Technology

TU Delft

TNO innovation for life

Design Feasibility of a Deployable Membrane Reflectarray Antenna for Space Applications

by

Niels Donners

To obtain the degree of Master of Science at the Delft University of Technology,
to be defended publicly on September 19, 2025 at 10:30

Student Name	Niels Donners
Student Number	5048761

Chair:	I. Uriol-Balbin
Independent Examiner	S. Speretta
Supervisor TU Delft:	P.P Sundaramoorthy
Supervisor TNO:	R.J. Bolt
Faculty:	Aerospace Engineering, TU Delft

TU Delft

Abstract

High-gain satellite antennas are traditionally realized as parabolic reflector antennas. These have good flight heritage and offer high directivity, but they suffer from some drawbacks including structural mass, inefficient volume usage and costs. Reflectarray antennas, and in particular flat deployable reflectarrays, have emerged as a promising alternative, having potential to reduce weight, lower costs and be more volume efficient. This thesis investigates the feasibility of designing a deployment mechanism for a two membrane reflectarray antenna that can meet mission requirements with Synthetic Aperture Radar (SAR) applications.

Reflectarrays, though introduced in 1963, have only recently been considered for space applications, with limited European involvement. Through the use of trade-offs, a design is proposed that is deployable but with limited influence on the antenna performance by using panels connected by spring activated hinges. This design is simulated in a space environment to quantify the temperature variation in orbit and the impact of coatings on the temperature.

Thermo-elastic simulations showed that a $5\,^{\circ}\mathrm{C}$ increase already violated one antenna performance requirement. Deployment analysis identified the risk of membranes impacting each other and causing potential damage to each other. In order to mitigate both the violation of the performance requirement as well as deployment, additional support structure or pre-tensions are proposed as potential solutions. An other kind of deployment instead of torsional springs is also suggested, as with torsional springs the impact speed during deployment was found to be to high.

Results show that a deployable reflectarray antenna is feasible, provided that key issues such as membrane spacing, thermal management, and deployment dynamics are addressed. Proposed solutions to these problems include: thermal coatings, structural supports, and pre-tensioning of the membranes. This thesis concludes that with further design iterations, a two-membrane deployable reflectarray can meet mission requirements and offer a promising alternative to conventional antenna systems.

Recommendations for future work include, coupling mechanical and RF simulations to better evaluate deformation tolerances, expand thermo-elastic simulations to a broader range of temperatures, and simulate multiple panels deploying at the same time.

Acknowledgments

This thesis marks the end of my TU Delft journey. Starting in 2019 with my bachelor in Aerospace Engineering, my fellow students and I went almost straight into COVID, lockdowns, and studying from home. In 2023 I graduated, and started the my master in Aerospace Structures and Materials, of which this thesis is the final work.

First and foremost, I would like to express my deepest gratitude to my two supervisors, Prem Sundaramoorthy as my TU Delft supervisor, and Roland Bolt as my TNO supervisor. Prem gave me lots of important insights on the thesis topic of which I would not have thought of and I value his advice highly. Roland give me a deep dive into the workings of antennas, but most specifically into reflectarrays. I would like to thank him for all of the knowledge I gained on how antennas work and guiding me towards this thesis report as the end result.

I would like to thank the entire radar department of TNO for the amazing time I have had at TNO. Even though I was officially an intern, I felt like I was part of the team. I also want to thank some people by name. So first, I would like to thank Cristina, Martijn, Rob, Maaike and (my favorite Italian college) Giuseppe for listening to and answering all my questions I asked over the time I was at TNO. I also like to thank Karin, Imke and Arjette for all the help and guidance they gave me.

I would also like to thank the COMSOL help desk for their help with the questions I asked on my COMSOL models.

Lastly I would like to thank my family and friends, specifically my parents, sister and of course my girlfriend, for all the support, of any kind, they gave me during my studies and during the process of this thesis.

Niels Donners
Delft, August 2025

Contents

List of Figures

List of Tables

List of Symbols and Abbreviations

Symbols

a	Semi-major axis
a	Albedo reflection coefficient
A	Area
c	Speed of sound in vacuum
d	Torsional spring wire diameter
D	Directivity
D_a	Diameter of the aperture
D_m	Main loop diameter
E	Elastic young's modulus
E_{tot}	Total amount of energy in the system
f	Frequency
f_d	Focal distance
F_{a_b}	View factor of a onto b
h	Height change
i	Inclination of the orbit
I	Moment of inertia
I_{yy}	Moment of inertia around the y axis
J_2	coefficient of second zonal term related to the oblateness of the earth
k	thermal conductivity
k_n	Wave number
l	length of one panel
L_{12}	Length from 1 to 2
L_0	Original length
N_a	Amount of loops in torsional spring
p	Semi-latus rectum
P_{in}	Power going into the system
P_{rad}	Power radiated by the system
Q_{in}	Heat going into the system
Q_{out}	Heat going out of the system
Q_{sun}	Heat going into the system originating from the sun
Q_{albedo}	Heat going into the system originating from albedo
Q_{IR}	Heat going into the system originating from earth infrared radiation
Q_{DS}	Heat ejected by the system to deep space
$\vec{r}_{mn}$	Position of the mn^{th} element relative to the origin of the array
$\vec{r}_f$	Vector pointing from feed to center of array
R_e	Radius of earth
R_{spring}	Distance of torsional spring acting on other body
T	Temperature
T_1	Temperature of element 1
T_2	Temperature of element 2
T_o	Orbital period

T_q	Torque
T_{ES}	Orbital period of earth around the sun
U	Radiation intensity
U_0	Radiation intensity of an isotropic source
x_{mn}	x coordinate of the mn^{th} patch
y_{mn}	y coordinate of the mn^{th} patch
z_{mn}	z coordinate of the mn^{th} patch
α	Absorptivity
α	Coefficient of thermal expansion
α_r	α coefficient used in Rayleigh damping
β_r	β coefficient used in Rayleigh damping
ΔT	Change in temperature
ΔL	Change in length
ϵ	Emissivity
$\epsilon_{effective}$	Effective emissivity taking into account the emissivity of two bodies
ζ	Damping factor
θ_0	Spherical coordinate theta for pointing of main beam
λ	Wavelength
μ	Standard gravitational constant of the planet
ν	Poisson ratio
ρ	Density
σ	Stephan-Boltzmann constant
σ	Stress
σ_y	Yield strength
υ_0	True anomaly
ϕ	Solar zenith angle
ϕ_0	Spherical coordinate phi for pointing of main beam
ϕ_{mn}	Excited phase of each mn^{th} patch
ω	Angular velocity
ω_o	Argument of periapsis
ω_1	Natural frequency 1
ω_2	Natural frequency 2
Ω	Longitude of the ascending node
$\dot{\Omega}$	Angular precession rate

Abbreviations

AO	Atomic Oxygen
ESA	European Space Agency
CTE	Coefficient of Thermal Expansion
DARPA	Defense Advanced Research Projects Agency
DaHGR	Deployable High Gain Reflectarray
EM	Electromagnetic
GCR	Galatic Cosmic Radiation
GOM5-X	GomSpace Express-5
HPBW	Half Power Beam Width
IKAROS	Interplanetary Kite-craft Accelerated by Radiation Of the Sun
IR	Infrared
ISARA	Integrated Solar Array & Reflectarray Antenna
LADeR	Large-Area Deployable Reflectarray
LEO	Low Earth Orbit

MaLDO	Magnetic lateral/depth offset
MaLO	Magnetic Longitudinal Offset
MarCO	Mars Cube One
M-Argo	Miniaturized Asteroid Remote Geophysical Observer
MMOD	Micro Meteoroids and Orbital Debris
NASA	National Aeronautics and Space Administration
OMERA	One Meter Reflectarray Antenna
OSS	Oxford Space Systems
PCB	Printed Circuit Board
PTR	Perimeter Truss Reflector
R3D2	Radio Frequency Risk Reduction Deployment Demonstration
RA	Reflectarray
RainCube	Radar in CubeSat
RF	Radio Frequency
SAR	Synthetic Aperture Radar
SC	Solar Constant
SLL	Side Lobe Level
SPE	Solar Partical Event
SSO	Sun-Synchronous Orbit
SWOT	Surface Water Ocean Topography
TE	Thermo-Elastics
TNO	Nederlandse Organisatie voor Toegepast Natuurwetenschappelijk Onderzoek
UV	Ultra Violet
VEMO	Very Efficient Miura-ori

Chapter 1

Introduction

High gain antennas on satellites are commonly fulfilled by parabolic reflector antennas. While current high gain parabolic reflector antennas have good flight heritage, high gain, high directivity and simplicity, they also have some disadvantages. One limitation is the parabolic shape itself. This design makes the satellite structure heavy, since it is usually built from a single large piece or several bulky sections. To preserve the required geometry the reflector is typically made from solid materials or from large sections. It becomes expensive due to the high surface accuracy that is required. In addition, the parabolic shape leads to inefficient use of volume. This inefficient use of space could be mitigated by making the parabolic shape deployable, but few research examples exist for current implementations [1]. Apart from its shape, the system itself has two further disadvantages. The first being the feed support structure blocking part of the signal causing a decrease in efficiency. Secondly the parabolic antenna requires pointing. This means the antenna must be mounted in specific positions and actively pointed toward its target.

A solution proposed for some of these problems is the reflectarray (RA) antenna. More specifically: a flat deployable membrane RA antenna. RAs, first introduced in 1963 [2], have seen a significant rise in interest in recent years. RA antennas can be potentially advantageous for Synthetic Aperture Radar (SAR) applications on a satellite. It is believed that RAs can have multiple significant advantages over more conventional high gain parabolic reflector antennas [3].

Due to the RA being flat it is cheaper to manufacture compared to a parabolic antenna [4]. Next to this it can become much lighter since only a little bit of material is needed to have a working RA surface. By having it deployable, it is believed to become much more volume efficient and hence saving on costs even more.

The first RA was only recently launched into space in 2017, so this application of this technology is less than ten years old [5]. And almost all current RAs with a space application are from the US. The EU is behind on the US and needs more experience on this kind of technology. This is especially relevant with the current vision of EU being more independent of the US.

It is however not straight forward to design a flat deployable RA antenna. First of all, RAs are normally not designed to be deployable. By making the RA deployable, and thus splitting it into multiple sections, several issues arise that need to be addressed. An ideal RA consists of reflective elements in a grid pattern. By splitting the RA into multiple parts this grid pattern is easily distorted. Besides this, there some other issues as well: the material restrictions limit the kind of usable materials for the deployment system, the flatness of each section needs to be sufficient, the separation between the two membrane layers must remain within tight tolerances, and the RA surface (the part of the RA illuminated by the feed) needs to survive deployment. In addition to these challenges, the harsh space environment further complicates the design. Materials need to be carefully selected for outgassing and cold welding, space radiation and atomic oxygen. Thermal cycling caused by orbital day-night transitions can induce significant temperature variations. Lastly there are Micro Meteoroids and Orbital Debris (MMOD) flying around that could impact and damage the surfaces.

Nederlandse Organisatie voor Toegepast Natuurwetenschappelijk Onderzoek (TNO) has recently designed a RA with a size of 55x$55\,\mathrm{cm}^2$ using two membranes [6]. They are investigating whether it would be possible to design an even larger RA of around 2.5x$2.5\,\mathrm{m}^2$ made deployable for a SAR application on a satellite. Based on all the information given above the following research question was therefor posed:

Main research questions:

Is it possible to design a deployment mechanism for a two membrane reflectarray antenna that still satisfies the mission requirements?

To answer this research question the following sub research questions have been posed which each of these also have again sub questions.

Q-100 *What are the possible configurations of deployment option and position for the deployable reflectarray and how does one trade these off to each other?*
- **Q-101** *What are the current deployable options for high gain (reflectarray) antennas?*
- **Q-102** *What are possible configurations for the system considering the satellite, reflectarray surface and feed?*
- **Q-103** *What parameters are important for a trade-off on a deployable reflectarray and how does one obtain these parameters?*

Q-200 *What is the impact of the environment during the lifetime of the reflectarray once in orbit?*
- **Q-201** *How does the environment influence the system on thermal aspects?*
- **Q-202** *How does the system respond to the different encountered temperatures?*
- **Q-203** *How does the environment influence the system during deployment on stress/deformation level?*
- **Q-204** *How can the conversion of the non-deployable to a deployable reflectarray surface be done such that structurally introduced changes have limited influence on the Radio Frequency (RF) performance of the reflectarray?*

This thesis focuses on the conceptual development and mechanical analysis of the orbital thermal loads and deployment mechanisms associated with a RA antenna system. The scope is limited to the RA surface itself; the feed deployment and design of structural feed support structure are excluded from this thesis. The analysis emphasizes in-orbit conditions, as these were deemed more critical than launch-induced loads or vibrations.

No RF design aspects of the reflectarray are addressed, such as element layout, phase tuning, or electromagnetic performance. Instead, the work concentrates on the mechanical behaviour and thermal response of the reflectarray during deployment and operation in orbit.

The structure of this thesis is as follows. In Chapter 2, a literature study is conducted to gain a better understanding of the functioning of a RA. Additionally, the state of the art in deployable RAs is presented, and the space environment is discussed, addressing question Q-101. In Chapter 3, two different concept generations and their respective trade-offs are presented. This chapter addresses questions Q-102 and Q-103. Based on these trade-offs, one concept is selected for further development throughout the remainder of the thesis. Chapter 4 outlines the methodology used to answer question Q-200, and the corresponding results are presented in Chapter 5. In Chapter 6, the conclusions of the thesis are summarized and includes the answer to the main research question. Finally, Chapter 7 provides recommendations for future work with summarized priority recommendations for the near future.

Chapter 2

Literature Study

In order to get a good grasp on the subject of deployable RAs a literature study has been performed. The focus of the literature study is on background knowledge of RAs, space missions using a RA, Folding techniques, any state of the art work and the relevant space environment in which the deployable RA will be present. Section 2.1 introduces general background knowledge on RAs and the current prototype of TNO. Secondly, recent and future space missions will be presented in Section 2.2 and Section 2.3 which used or will use a (deployable) RA. In Section 2.4 potential folding techniques will be discussed for solid panels. Section 2.5 will then present state of the art published solutions for deployable large aperture antennas. Section 2.6 will discuss the relevant space environment and Section 2.7 present requirements of the system. Lastly Section 2.8 will give a short conclusion which can be drawn from the literature.

2.1 Reflectarray Background Knowledge and the Current Prototype

In recent years, RAs have gained more attention in literature, as illustrated in Figure 2.1. A RA combines elements of a traditional reflector antenna, like a parabolic dish, with elements of a printed antenna. Similar to a conventional parabolic dish antenna, a RA uses an illuminating feed antenna to direct Electromagnetic (EM) waves towards a reflective surface. Upon reaching the RA surface, these waves are reflected by individual elements, each acting as its own radiating source.

To steer the (reflected) beam in a specific direction, each element must introduce a relative phase shift to the EM waves it reflects. This process is similar to the operation of a phased array antenna, where the beam direction is controlled by carefully designing the phase shifts of each reflective element. An example of a steered beam formed by a 1D phased array is shown in Figure 2.2.

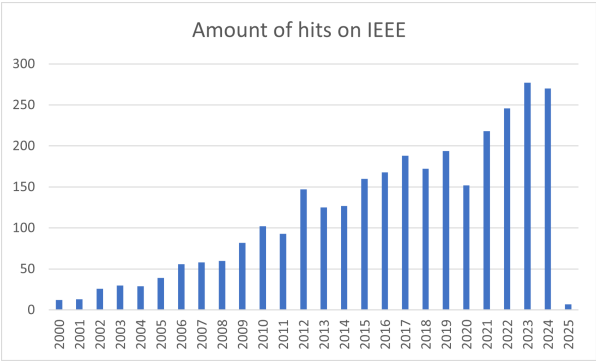

Figure 2.1: Annual number of search results for the term ”reflectarray” on IEEE Xplore. Data retrieved on January 17, 2025.

While a phased array uses electronics behind each element to actively change the phase of the excited signal, a RA is a passive system. One disadvantage of RAs compared to phased arrays is that the phase shifts cannot be altered once the patches are manufactured, hence their passive nature. Phased arrays are typically heavier due to the electronics that are required to actively steer the beam, whereas RAs use passive hardware to induce phase changes, making them substantially lighter. The most common method for inducing phase shifts in RAs is by using patches of various sizes, although there are multiple options available, including phase/time delay lines and also rotated elements.

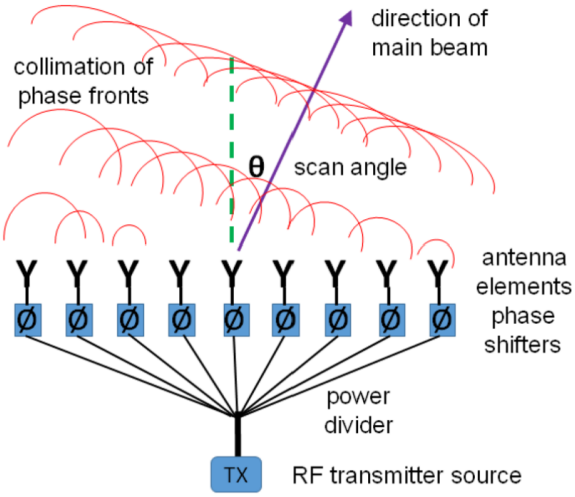

Figure 2.2: Beam steering in a phased array is achieved by radiating elements with slightly different phases, enabling directional control of the emitted signal [7].

Once the EM waves are reflected off the RA surface, they form a radiation pattern once in the far field. This introduces a minimum distance required between the feed and the RA surface, since the signal needs space to form into a proper radiation pattern. A typical radiation pattern consists of a main beam and several side lobes, which have lower intensity compared to the main lobe, as shown in Figure 2.3.

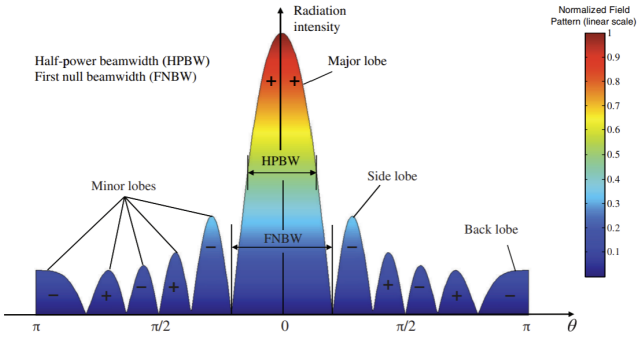

Figure 2.3: Example of a far-field radiation pattern illustrating the main lobe, side lobes, and the Half Power Beam Width (HPBW) [8].

It is important to understand the definition of the Half Power Beam Width (HPBW), see Figure 2.3. The HPBW is the angular width of the main beam where the intensity drops by 50% (or 3 dB) compared to the peak intensity of the main lobe [8]. To achieve a lower HPBW, more radiating elements are required since better beam forming can be achieved. Increasing the number of elements not only narrows the lobes but also increases the number of lobes.

Next to that directivity and gain are crucial terms. Directivity is defined as ”the ratio of the radiation intensity in a given direction from the antenna to the radiation intensity averaged over all directions” [8]. Mathematically, this can be expressed as [8]:

$$D = \frac{U(\theta,\phi)}{U_0} = \frac{4\pi U(\theta,\phi)}{P_{rad}} \tag{2.1}$$

Here U is the radiation intensity, U_0 is the radiation intensity of an isotropic source and P_{rad} is the total radiated power. The gain of an antenna is closely related to the directivity, but directivity also takes into account the losses of the antenna whereas the gain does not. Directivity is defined as "the ratio of the intensity, in a given direction, to the radiation intensity that would be obtained if the power accepted by the antenna were radiated isotropically" [8]. In mathematical form this can be written as [8]:

$$Gain = 4\pi \frac{U(\theta,\phi)}{P_{in}} \tag{2.2}$$

The first concept on RAs antennas was introduced in 1963 using variable lengths short□ended waveguide elements [2]. The lengths of the elements were carefully chosen to achieve different phase shifts. This ensures that the reradiated signals from each element combine to form a collimated beam in the far field. A downside of this initial concept was its very bulky and heavy design. Nowadays the phase shifts can be obtained with different kind of elements resulting in lighter and slimmer designs due to the use of printed antenna technology. In general there are three kind of element groups that can induce a phase shift to the EM waves [9]:

- Elements with phase/time - delay lines
- Elements with variable rotation angles
- Elements with variable sizes

The elements with phase/time-delay lines use a concept similar to waveguide elements. The incoming EM wave is received by an element and then phase-shifted using a delay line. By changing the length of the delay line a different distance is travelled by the EM wave. The wave is reflected at the end of the delay line and finally reradiated outwards by the element with a phase shift. One can then tune the length of these lines to get the desired phase shift for each element. The elements with variable rotation angles have limited applications, since they can only be used with circularly polarized waves. By rotating the element itself, the phase tuning can be performed. Lastly there are the elements with variable sizes. By changing the length and thus the size, the element changes its resonant frequency, which results in a radiated phase shift at a certain frequency. Basic examples of the different elements can be observed in Figure 2.4.

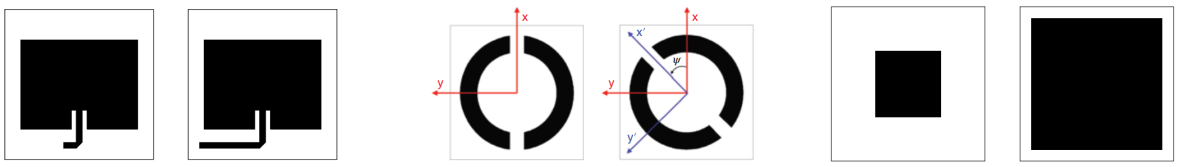

(a) Elements with phase/time□delay lines **(b)** Elements with variable rotation angles **(c)** Elements with variable sizes

Figure 2.4: Different types of phase-shifting elements. All subfigures (a–c) are taken from [9].

TNO created a prototype of a RA using radiating elements where phase shifts are induced by patches with variable sizes. To determine the required phase shifts that each patch needs to achieve, it is important to know the distance between the patch and the feed source point, and the required direction of the main beam. The required phase shift of each patch can be calculated with the following equation [9]:

$$\phi_{mn} = k_n \left(|\vec{r}_{mn} - \vec{r}_f| - x_{mn}\sin(\theta_0)\cos(\phi_0) - y_{mn}\sin(\theta_0)\sin(\phi_0) - z_{mn}\cos(\theta_0) \right) \tag{2.3}$$

In this equation k is the wave number ϕ_0, θ_0 are the spherical angles of the direction of the main beam, x_i, y_i and z_i are the Cartesian coordinates of the mn^{th} patch and $|\vec{r}_{mn} - \vec{r}_f|$ is the distance between the mn^{th} patch and the illuminating feed source. Once the phase shifts are known for each patch the

size can be determined by a so-called S-curve. Figure 2.5 shows the S-curve corresponding to the elements used in the prototype of TNO for different frequencies. A phase jump happens when the difference in size of two adjacent patches is substantially large. This is a general feature of RAs which uses elements with variable sizes, which can be observed as (partial) circles on the RA.

Besides the size of the patches also their spacing is of importance. As stated before the more radiating elements the smaller the lobes will be and hence the lower the HPWB will become. The spacing between the patches are determined by the wavelength and thus by the frequency at which the RA operates. This results in the current size of the RA prototype of 55cm x 55cm while only having 12 x 12 radiating elements.

It is also important to know the required distance between the illuminating feed source and the RA surface. For the electromagnetic field to form properly, a certain distance is necessary for the transition from the near field to the far field of the EM waves. This depends on the size of feed antenna and on the wavelength of the signal. The distance of the feed relative to the diameter of the array is typically expressed as an $\frac{f_d}{D}$ factor, where f_d is the distance of the feed orthogonal to the RA, and D is the diameter of the aperture of the RA. In the case of the prototype, the $\frac{f_d}{D}$ ratio is set to 0.85. It should thus be noted that when a larger RA surface is required, with more patches, also a bigger distance is needed between the surface and the illuminating feed source.

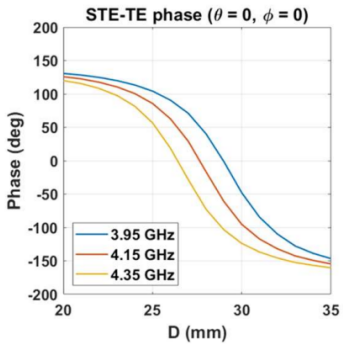

Figure 2.5: Example of an S-curve used to determine the patch diameter corresponding to a given phase shift [6]. The x-axis represents the patch diameter, while the y-axis shows the resulting phase of the radiating element.

Lastly the cross section of the prototype is of importance. This is shown in Figure 2.6 for the current prototype. A total of five layers are used consisting of polyimide, copper and an air cavity. The copper is used for its electrical properties while the polyimide is used for its structural properties and is only used to support the shape and position of the copper. These layers are all very thin, $17\,\mu\mathrm{m}$ and $50\,\mu\mathrm{m}$ for the copper and polyimide, respectively. This means a total thickness of $3.844\,\mathrm{mm}$ is required due to the air cavity of $3.71\,\mathrm{mm}$.

Layer stack

Name	Type	Material	Description	Thickness
Layer 5	Metal	Copper	Patches	17 µm
Layer 4	Dielectric	Polyimide	Membrane	50 µm
Layer 3	Dielectric	Air	Air Cavity	3.71 mm
Layer 2	Metal	Copper	Ground Plane	17 µm
Layer 1	Dielectric	Polyimide	Membrane	50 µm

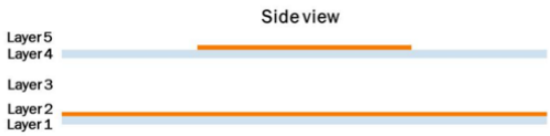

Figure 2.6: Cross-sectional view of the prototype reflectarray designed by TNO visualizing the different material layers [6].

2.2 Recent Space Missions using a (Deployable) Reflectarray

One of the advantages of RAs is that they can have a lot of different shapes. This includes also a flat shape, as the patches can be phase tuned such that the flat shape is accounted for. This has some

significant advantages compared to traditional parabolic dish reflectors. First of all, manufacturing is easier and cheaper due to Printed Circuit Board (PCB) technology. It is also more lightweight compared to the bulky dish reflectors. The final major advantage is that its flat design allows for easier deployment compared to parabolic dish antennas. This would save precious space, for example, inside the launch vehicle fairing.

In 1996, John Huang proposed the concept of using deployable RAs made up of flat panels for large space deployments [10]. He also suggested that these RAs could be combined with solar cells on their reverse side. Several years later the first RA was launched into space on the Integrated Solar Array & Reflectarray Antenna (ISARA) mission in 2017 [5]. ISARA and numerous other missions have been launched with RAs which will be presented in this section.

2.2.1 Integrated Solar Array & Reflectarray Antenna (ISARA)

ISARA was a Cubesat with a bus size of 3U (1U = $10\,\mathrm{cm}$x$10\,\mathrm{cm}$x$10\,\mathrm{cm}$). It was launched in 2017 and was the first satellite to use a RA in space. As can be observed in Figure 2.7 it consisted of three panels, with each having a RA on one side and solar panels on the other side, maximizing use of the deployed area. The feed is located on the small flap on the other side of the CubeSat. The panels folded around ISARA to save space and were deployed with the use of a spring hinge. It should be noted that there were quite large gaps between the panels. Each panel had a size of $33.9\,\mathrm{cm}$ x $8.26\,\mathrm{cm}$, which resulted in a total aperture area of $0.0891\,\mathrm{m}^2$ [11]. Also a gain of $33\,\mathrm{dBic}$ at a frequency of $26\,\mathrm{GHz}$ was obtained, resulting in an aperture efficiency of 26%. This efficiency is rather low, due to the large gaps between the panels.

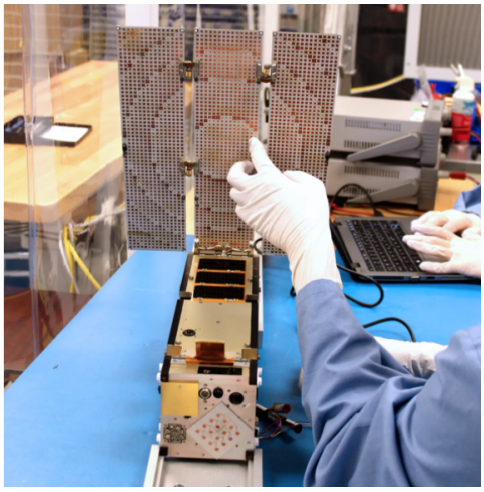

Figure 2.7: The ISARA CubeSat in its deployed configuration, showing the reflectarray with its individual patches clearly visible [5].

2.2.2 Mars Cube One (MarCO)

MarCO was the next mission using a RA after ISARA and was launched in 2018 [12]. It consisted of two identical CubeSats both being used as a X-band telecommunication system. These provided auxiliary telecommunications during the entry, descent and landing portion of the NASA InSIGHT Mars lander mission. It was successfully deployed and was also the first CubeSat used in a deep space mission. It uses a similar deployment as ISARA, also with the use of spring hinges, but as can be observed in Figure 2.8a, the gaps are almost not visible between the panels. This increased aperture efficiency to 42%. It had a total aperture size of $0.2178\,\mathrm{m}^2$ but on an increased bus size of 6U compared to the 3U of ISARA. It realized a gain of $29.2\,\mathrm{dBic}$ at a frequency of $8.4\,\mathrm{GHz}$.

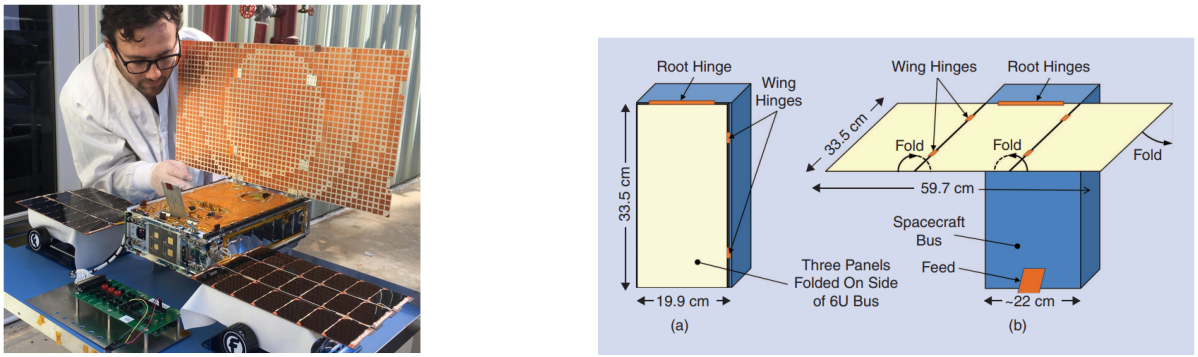

(a) (b)

Figure 2.8: MarCO CubeSat in deployed configuration. (a) One of the MarCO CubeSats in its deployed configuration [13]. (b) Schematic view of the MarCO deployment mechanism [12].

2.2.3 Capella-1 and -2

In 2018 the Capella-1 satellite launched with on board a $8\,\mathrm{m}^2$ sized origami like membrane antenna according to [14]. Information about the antenna is very limited but the idea of a membrane antenna looks forsaken, since the follow-up Capella-2 mission uses a deployable mesh antenna.

2.2.4 Radio Frequency Risk Reduction Deployment Demonstration (R3D2)

The mission R3D2 from Defense Advanced Research Projects Agency (DARPA), launched in 2019, had a prototype RA on board [15]. Not a lot of information is available on this RA, but it is the first on-orbit membrane RA. It had a deployed size of $2.25\,\mathrm{m}$ diameter, but was tightly wrapped and stored on the satellite during launch. It was made of thin Kapton and the membrane was supported by booms to stay in the desired shape, see Figure 2.9. There is no detailed RF data available to the public [14], but a paper is published where prototypes are mentioned in [16] .

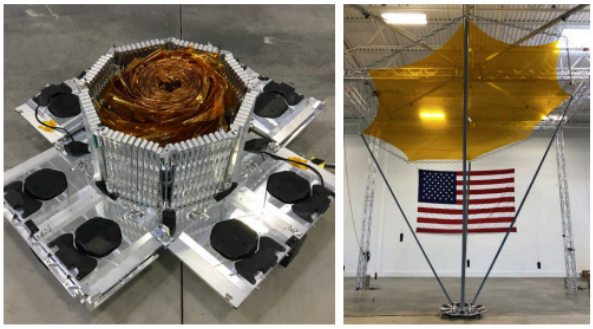

Figure 2.9: The R3D2 mission in its stowed and deployed configurations [15]

2.2.5 Surface Water Ocean Topography (SWOT)

SWOT is a big satellite (with a size of 14.9 x 5 x $5\,\mathrm{m}$ [17]) used for collecting data on water bodies across earth. Despite the bigger size compared to the other satellites it is still mentioned here, since there are currently so few space missions that have used a RA. SWOT uses two big RAs on each side of its bus to collect data, these are currently the biggest RAs launched to space with each a size of 0.5 x $5\,\mathrm{m}$ [18]. SWOTs deployment includes the extension of the arms on which the RAs are connected to instead of the RAs itself. It was launched in 2022 and designed to last for 3 years.

2.3 Future Missions using a Deployable Reflectarray

ISARA, MarCO, Capella-1 and R3D2 are the only few missions which used a deployable RA as an antenna. There are two missions planned to have a deployable RA as well.

Miniaturised Asteroid Remote Geophysical Observer (M-Argo) is planned to be a 12U CubeSat with a RA consisting of three panels, as can be seen in Figure 2.10. Not a lot of information is given by the European Space Agency (ESA), but doing some rudimentary calculations based on the figure and the known size of 22 x 22 x $34\,\mathrm{cm}$ of the CubeSat bus the RA will have an area of around $0.2244\,\mathrm{m}^2$ [19]. Latest info suggest that M-Argo will launch in 2026 according to one of the subcontractors [20]. The mission of M-Argo includes the study of asteroids and the identification of the materials it consists of.

Secondly, there is the GomSpace Express-5 (GOM5-X) CubeSat. There is unfortunately even less information available to the public compared to M-Argo. One off the subcontractors posted on their website that a RA will be on the satellite, to be designed by TICRA [21]. Online renders indicates that the RA is most likely going to be of rectangular shape. No other information was provided about the actual RA. This means that the size, frequency and gain are still unknown.

Figure 2.10: The M-Argo CubeSat in its deployed configuration [19].

2.4 Folding Techniques for Solid Panels

Relevant folding techniques can be divided in three techniques for deployable solid panels:

- Regular folding
- Miura-ori
- The flasher concept

With regular folding, the not complex or not origami inspired folding is meant. This includes the folding and deployment of for example MarCO and ISARA. These use plain straight folds and have a limited amount of fold lines to reduce complexity and points of failure.

Miura-ori is a folding scheme where a rectangular membrane is folded into a package of flat shape [22]. The most basic and easy folding patterns can be seen in Figure 2.11. The standard way of folding is the letter folding. It can however be seen that the mountain and valley folds are fairly random. It should also be noted that the deployment sequence of the letter folding consist of multiple steps, which is undesirable for a self-deploying system. Using a different folding techniques that is also used for folding road maps gives the bottom figure of Figure 2.11. This has as advantage over the letter folding technique that the mountain and valley folds are more repetitive and the deployment sequence is much simpler. It can be deployed by just pulling on the opposite corners limiting the multiple steps needed for the letter folding.

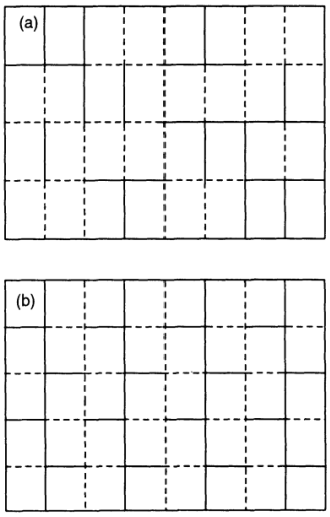

Figure 2.11: Basic Miura-ori folds. Subfigure (a) illustrates the letter fold, and (b) shows the map folding technique. Dashed lines indicate valley folds, while solid lines represent mountain folds [22].

By introducing an angle $\pm\alpha$ between the vertical folds in a zigzag pattern the Miura-ori pattern can be obtained. An example can be seen in Figure 2.12. A big advantage of this folding technique is that the deployment of the Miura-ori pattern is synchronous whereas the map folding is more sequentially. Another advantage is the small offset of the nested folds, reducing the maximum curvature and with that the stress level of the crease [22].

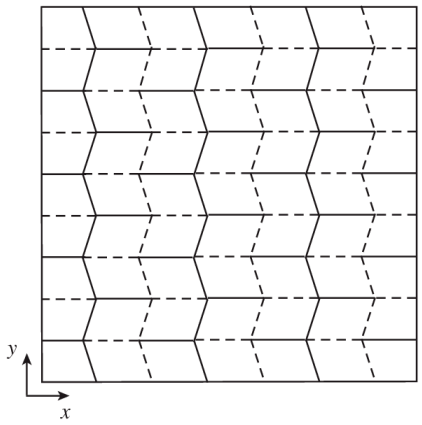

Figure 2.12: Miura-ori folding pattern with angled vertical folds. Dashed lines indicate valley folds, while solid lines represent mountain folds [23].

Unlike the Miura-ori fold, which remains flat when folded, the flasher fold results in a 3D shape when stored, as shown in Figure 2.13. This fold can be deployed using centrifugal forces, as demonstrated by the Interplanetary Kite-craft Accelerated by Radiation Of the Sun (IKAROS) mission [24]. Besides the storage state the unit-cell panels are also different for the flasher compared to the Miura-ori. Where the Miura-ori sub-panels are almost all parallelogram shaped the flasher has a lot of different sized and shaped panels. This is also highly depend on the actual folding used since there are a lot of options available and each can be unique.

For all origami techniques, the flatness of the deployed state must be considered. It is undesirable for the RA to revert to its folded state, so structural support is necessary to maintain the deployed configuration.

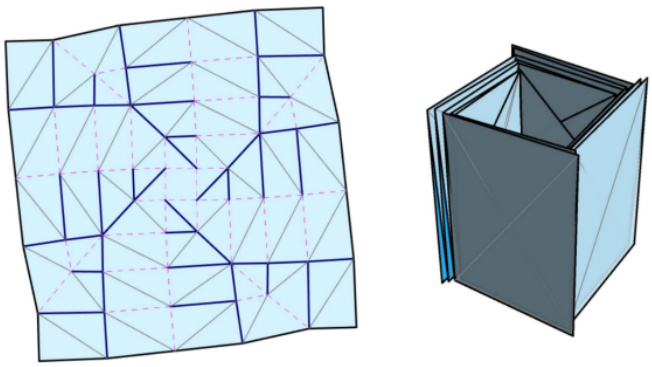

Figure 2.13: Flasher folding model illustrating the creased and folded configurations, addapted from [25].

2.5 State of the Art Deployable antennas

This section will present different kind state of the art antennas as published in literature. Since there are many different kind of antennas a focus is laid on solid panel reflectarrays, mesh antennas, membrane antennas and other reflectarrays.

2.5.1 Solid Panel Reflectarray Antenna

The first group is the group of RAs that consists of patches on a support panel. Already stated examples for this are the ISARA, MarCO, SWOT, M-argo and GOM5-X missions. They have a solid support plate and cannot wrinkle because of this. The solid panel RAs can be subdivided on deployment choice:

- Regular folding
- Origami inspired folding

Regular folding consist of for example the ISARA and MarCO missions. These use simple folding techniques to limit the amount of failure points. Also no diagonal-axis folding is performed with a limited amount of hinges, commonly spring hinges are used as activation mechanisms.

Next are the origami-inspired deployment systems. One of the simpler examples is OMERA (One Meter Reflectarray Antenna) [26], see Figure 2.14a. It consists of 16 individual RA panels folded around the CubeSat bus. The feed then deploys outward from the center of the RA, achieving the required distance between the feed and the RA, as needed for the $\frac{f_d}{D}$ ratio. OMERA reported a gain of $47.4\,\mathrm{dBi}$ at $35.75\,\mathrm{GHz}$, with a total size of 98.6 x $82.1\,\mathrm{cm}$.

Then there is the Oxford Space Systems (OSS) RA [27]. This is a big RA of around $12\,\mathrm{m}^2$. Instead of using vertical or horizontal creases like ISARA and OMERA, it uses diagonal creases, which may allow it to be more easily folded onto itself rather than wrapped around the satellite. They reported a gain of $31.6\,\mathrm{dB}$ at $9.65\,\mathrm{GHz}$ with a total size of the array of 424 x $283\,\mathrm{cm}$.

The Hexagon twist is an other option proposed for a deployable RA[28]. It would be stowed outside the CubeSat and than first be erected and than the sides will fold open revealing all the patches, see Figure 2.14b. It was reported to have a size of $58\,\lambda_0^2$, meaning that it had a size of 58 electrical units, converting it to centimeters with the known frequency of $16\,\mathrm{GHz}$ gives $203\,\mathrm{cm}^2$. A gain of $26.6\,\mathrm{dBi}$ was reported.

Next there are two designs published who use the Miura-ori folding pattern for the deployable RA. One focuses on the different angles of the unit cells of the Miura-ori [29], while the other focuses on the amount of unit cells for a specific area, the design in this paper is called Very Efficient Miura-ori (VEMO) [30]. The first design reports a gain of $26.2\,\mathrm{dBi}$ at a frequency of $8.42\,\mathrm{GHz}$. The total size of this design is 35.5 x $35.2\,\mathrm{cm}$ meaning it is close to square. It does not specify a proposed way of deploying the RA. VEMO has a deployed size of 24.8 x $24.8\,\mathrm{cm}$ meaning the end shape is square. At a frequency of $38\,\mathrm{GHz}$ a gain is reported of $37.1\,\mathrm{dB}$. VEMO does provide an idea on how to deploy the RA: with the use of Magnetic Longitudinal Offset (MaLO) hinge. In [31], the MaLO hinge and magnetic

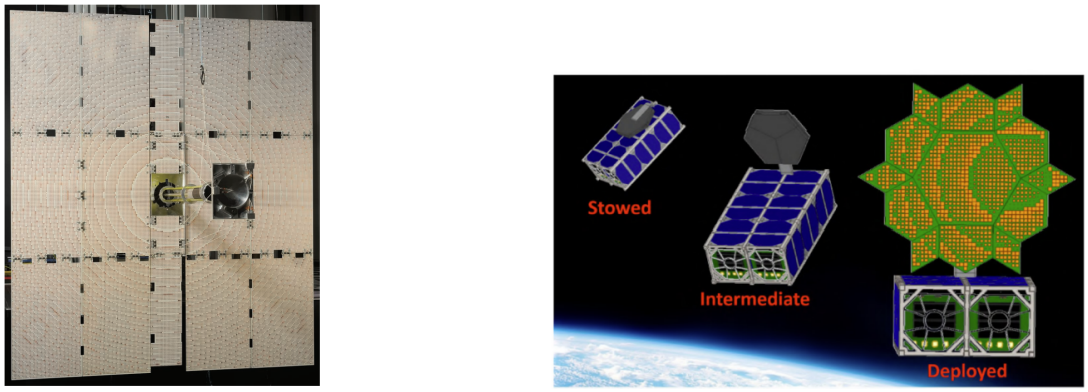

(a) (b)

Figure 2.14: Examples of deployable reflectarray designs. (a) The OMERA reflectarray in its deployed configuration, adapted from [26]. (b) The hexagon twist reflectarray, adapted from [28].

lateral/depth offset (MaLDO) hinge are discussed in more detail. These hinges enable self-actuation and stabilization making them ideal for compact space structures.

Lastly, there is the flasher folding model with solid panels [32]. It consists completely of triangular RA panels as can be seen in Figure 2.15. The feed is deployed outwards away from the RA, similarly as OMERA did. It is supposed to be used on a 3U CubeSat and the deployed size of the RA is equal to $4100\,\mathrm{cm}^2$. A gain of $29.7\,\mathrm{dBi}$ at $7.5\,\mathrm{GHz}$ was reported.

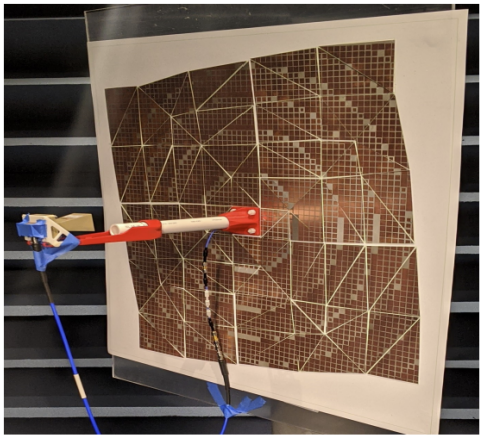

Figure 2.15: Solid-panel deployable flasher reflectarray designed for small satellite applications [32].

2.5.2 Mesh Reflector

A mesh reflector works similarly to a normal parabolic antenna, but can be made from a fine low weight mesh instead of solid material. This can be done due to fact that the EM waves respond to the mesh as if it would have been of solid material. For this to happen, the distance needs to be smaller than $0.5\,\lambda$ of the EM wave. Even though it is not a RA, mesh reflectors are still relevant due to deployment of a large surface area on a small bus.

The first example is the mission Radar in CubeSat (RainCube). This is a CubeSat of 6U launched in 2018 which uses a mesh antenna. The mesh antenna is illuminated by a feed and a sub reflector (Cassegrain design) and had a parabolic shape with a diameter of $50\,\mathrm{cm}$. It got the desired shape with the use of support ribs along the parabolic shaped mesh. The deployment steps can be seen in Figure 2.16 where the final step is the fully deployed state. It was designed to have a gain of $42.6\,\mathrm{dBi}$ at $35.75\,\mathrm{GHz}$.

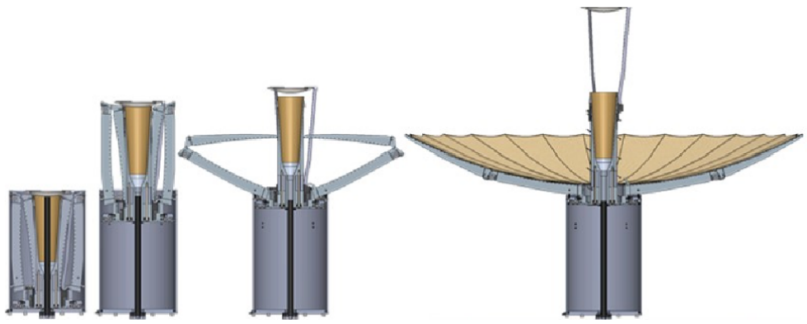

Figure 2.16: Deployment sequence of the RainCube satellite, illustrating the unfolding of its antenna system. Adapted from [33].

A mesh antenna that can be used in both the X- and Ka-band is proposed in [34]. It is a Tendeg patented technology but it was funded by National Administration for Space Administration (NASA). The diameter of this antenna is $1\,\mathrm{m}$ and the mesh is tensioned by a tensegrity system. It can be observed in Figure 2.17. Since the diameter of the antenna is large also the distance between the feed and the antenna needs to be big. This results in the deployment of the reflector at a large distance from the CubeSat. Since it can operate at two frequencies also two different gain values are presented: $36.8\,\mathrm{dBic}$ at X-band and $48.7\,\mathrm{dBic}$ at K_a-band.

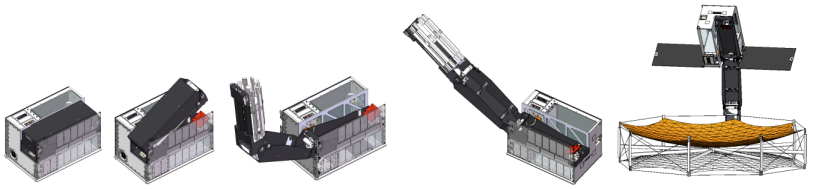

Figure 2.17: Deployment sequence of a 1-meter deployable mesh antenna, illustrating the transformation from stowed to fully deployed configuration [34].

Tendeg has two other mesh antennas available according to their website [35]. They are called kaTENna and the PTR (Perimeter Truss Reflector). They both have the same kind of design as the antenna shown in Figure 2.17. They state that the kaTENna has a gain of $49.2\,\mathrm{dB}$ at $36\,\mathrm{GHz}$ with a diameter of also $1\,\mathrm{m}$. The PTR has a gain of $48.9\,\mathrm{dB}$ at $9.6\,\mathrm{GHz}$ with a diameter of $3\,\mathrm{m}$.

2.5.3 Membrane Reflectarray Antenna

The membrane RA antennas works the same as the solid panel planar RAs. However, these consist most of the time of two thin membranes, saving weight compared to the solid panel RAs. It should be noted that the current prototype of TNO is also a membrane RA. Since it is a membrane, it does not have inherent stiffness. To achieve the required flatness, the membrane needs to be tensioned in some way. This requires a support structure, which adds weight to the design.

The first mention of a tensioned RA is for the torus and horseshoe inflatable support structures [36]. These try to implement a lightweight solution by using a inflatable that is very thin but keeps it shape due to the internal pressure. The torus has a diameter of $1\,\mathrm{m}$ and the feed is exactly in the middle above the RA. The support structure of the feed is also an inflatable where each part of the support structure is spaced evenly around the feed, see Figure 2.18a. A gain of $33.7\,\mathrm{dBi}$ at $8.3\,\mathrm{GHz}$ was reported. The horseshoe is also an inflatable but with an increased diameter of $3\,\mathrm{m}$. Also the feed of this design is supported by inflatables. However, these are not equally distributed around the feed. They are concentrated on one side, this is done to point the beam in the other direction and have a clear view without obstructions that reduce the gain, see Figure 2.18b. It had a gain of $54.4\,\mathrm{dBic}$ at $32\,\mathrm{GHz}$.

Since these approaches using inflatables require a system for gas storage and inflation, which compro-

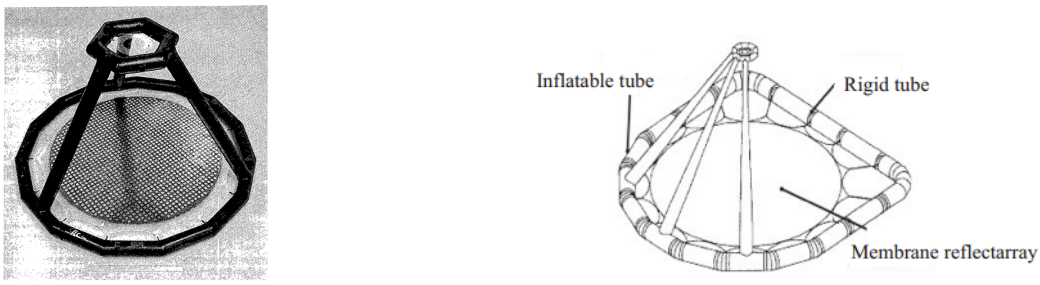

(a) (b)

Figure 2.18: Two inflatable membrane reflectarray designs. (a) Torus configuration, adapted from [36]. (b) Horseshoe configuration, adapted from [37].

mises lightweight and reliability, new deployment mechanisms have been proposed. This includes the membrane antenna Deployable High Gain Reflectarray (DaHGR) by MMA Design LLC and Northrop Grumman. The RA is tensioned with the use of structural deployment elements, as can be seen in Figure 2.19. They reported a gain of $34\,\mathrm{dBi}$ at $10\,\mathrm{GHz}$ for a diameter of $61\,\mathrm{cm}$ [38].

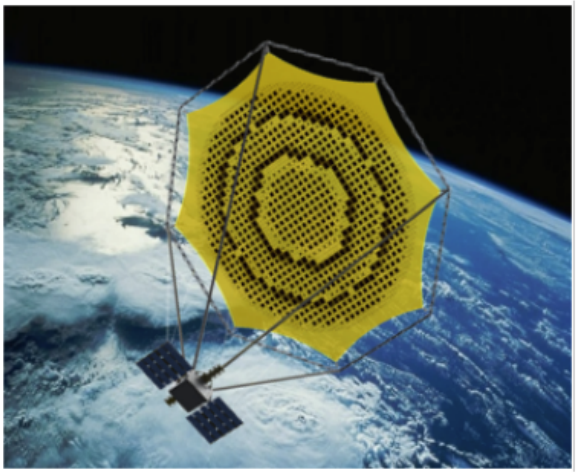

Figure 2.19: The DaHGR antenna in its deployed configuration, adapted from [38].

Another membrane antenna is proposed called Large-Area Deployable Reflectarray (LADeR) [39]. This concept does not use a support structure around the membrane to tension it. It is based on a flasher origami technique but deployment consist of two steps. First, arms are deployed to unwrap the membrane and than the membrane is unfolded completely. The steps for a prototype can be seen in Figure 2.20a. An interesting system has been designed to get the required distance between the membranes. So-called S-springs are reported to activate during deployment to achieve the necessary spacing; however, the exact mechanism of their activation is not mentioned. The S-springs can be observed in Figure 2.20b. They reported a gain of $39.6\,\mathrm{dB}$ at $8.4\,\mathrm{GHz}$ for a square shape with sides of 1.5 x $1.5\,\mathrm{m}$.

Lastly there is the membrane antenna mentioned before with the R3D2 mission by DARPA. But there is little information available to the public except for the circular shape and its diameter of $2.25\,\mathrm{m}$.

2.5.4 Other Reflectarrays

Since a RA is a passive system (it can not change the angle of the pointing beam) some of the research is performed on trying to scan the beam of a RA. Since the size of the patches can not be altered for this, the research focuses on the physical movement of the RA itself.

One example is an array consisting of foldable parts [40]. It can switch between two arrays designed

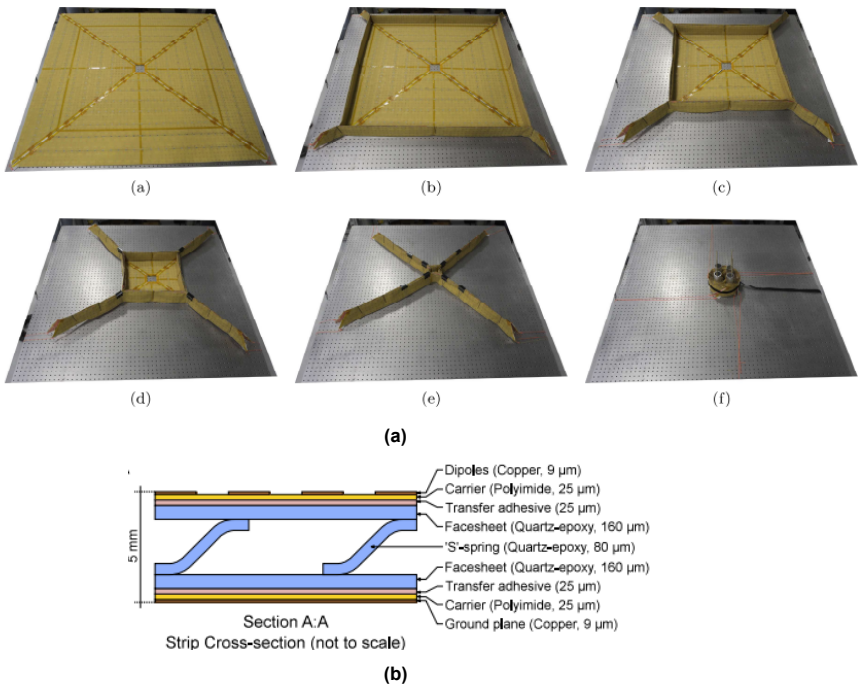

Figure 2.20: (a) Sequential deployment steps of the LADeR system. (b) Illustration of the S-spring element used in the deployment process. Both subfigures adapted from [39].

for the beam to be pointed in different directions. Depending on the folding direction different patches will be visible for the feed. The concept can be observed in Figure 2.21a.

Also a rollable RA surface is being considered [41]. This design consists of a flexible RA, see Figure 2.21b. When physically rolling the RA new patches will be visible for the feed resulting in a new beam direction. This results in some way of beam scanning, but not as good as the phased arrays can have.

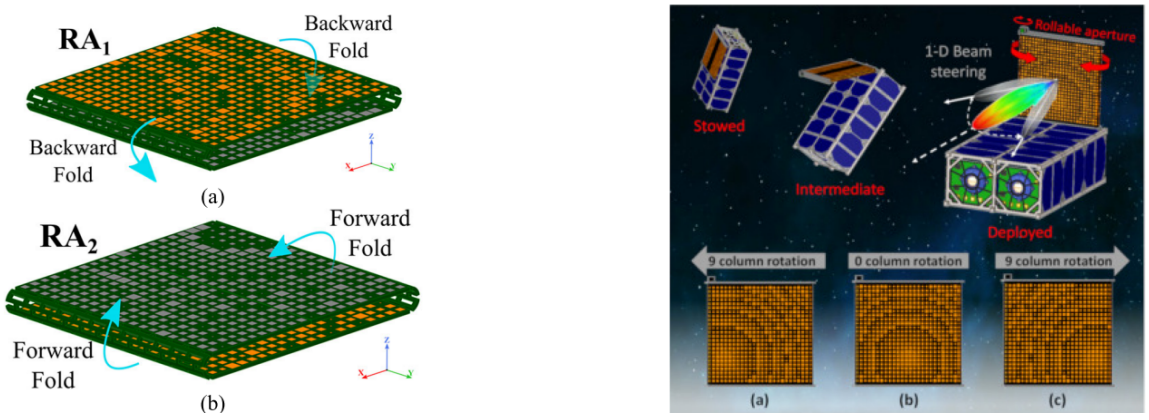

Figure 2.21: Two reflectarray designs with beam scanning capabilities. (a) Beam-scanning reflectarray consisting of two patch arrays, adapted from [40]. (b) Rollable aperture reflectarray antenna for beam scanning, adapted from [41].

Besides beam scanning RAs, also a interesting radiating multipurpose element design is proposed in [42]. Here the unit cell allows creases diagonally through the unit cell, as can be seen in Figure 2.22. This design results in radiating elements being able to be on the crease lines, where otherwise these

would be removed. This can be seen with other examples like the hexagon twist RA, here patches are removed on the fold lines. A square RA with sides of $45.9\,\mathrm{cm}$ was build and tested. For this RA a gain was reported of $23.6\,\mathrm{dBi}$ at a frequency of $5.79\,\mathrm{GHz}$. There is however no mention on how this would be deployed.

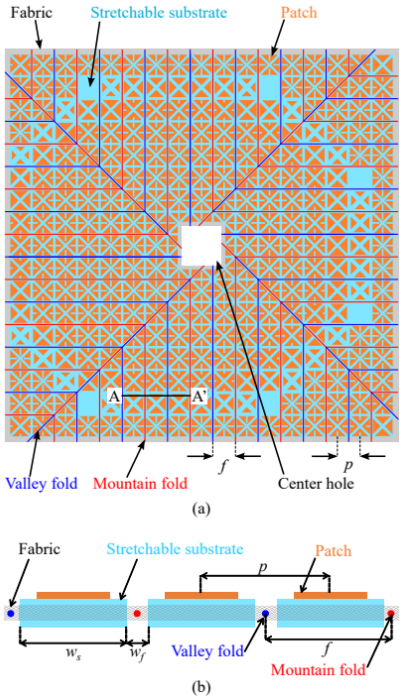

Figure 2.22: Views of the foldable reflectarray structure with radiating multipurpose elements. (a) Top view of the reflectarray. (b) Cross-sectional view of the reflectarray. Both subfigures adapted from [42].

Lastly there is the prototype of TNO but this is not deployable yet. The membrane RA of TNO currently has a gain of $25\,\mathrm{dBi}$ at $4.15\,\mathrm{GHz}$ [6]. The prototype can be observed in Figure 2.23 and has a size of 55 x $55\,\mathrm{cm}$.

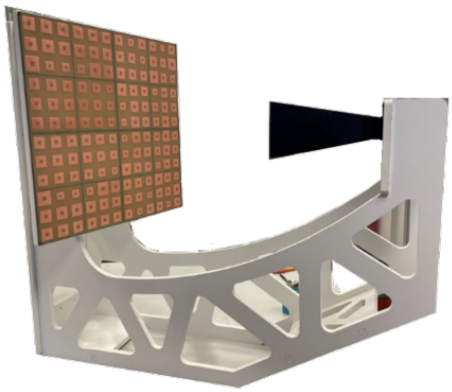

Figure 2.23: Prototype membrane reflectarray developed by TNO, adapted from [6].

A summary with all of the important parameters of relevant antennas can be found in Table 2.1. The parameters include: relevant year, if it was launched to space, type of antenna, bus size or relevant storage, antenna shape, antenna size, gain, frequency and frequency band.

To convert the units of length in cm to λ_0, as used in the table, one uses the following conversion:

$$x[\lambda_0] = \frac{x[cm]}{\lambda} \tag{2.4}$$

Here λ is the wavelength which can be calculated with:

$$\lambda = \frac{f}{c} \tag{2.5}$$

Here f is the relevant frequency and c the speed of sound in a vacuum.

Table 2.1: Summary of antenna characteristics, including launch year (if applicable), antenna type, bus size or storage requirements, antenna shape and size, gain, frequency, and frequency band. A dash (–) indicates unavailable data.

Reference	Year published	Launched?	Type	Bus size	Shape	Mass [kg]	Antenna size [cm]	Antenna size [λ_0]	Gain	Freq [GHz]	Freq band
ISARA [11]	-	2017	Panel RA	3 U	Rectangle	5 bus	33.9 x 24.8	29.4 x 21.5	33.5 dBic	26	K-band
MarCO [12]	-	2018	Panel RA	6 U	Rectangle	1	33.5 x 58.7	9.4 x 16.4	29 dBic	8.4	X-band
Solid panel flasher [32]	2020	No	Flasher based RA	1U stowage	Square	-	64.2 x 64.2	16.1 x 16.1	29.7 dBi	7.5	C-band
Deployable Miura-Ori [29]	2020	No	Miura-ori RA	-	Square	-	35.5 x 35.2	10.0 x 9.9	26.2 dBi	8.42	X-band
OMERA [26]	2021	No	Panel RA with sub-reflector	6 U	Rectangle	-	98.6 x 82.1	117.5 x 97.8	47.4 dBi	35.75	K_a-band
Hexagonal twist [28]	2021	No	Panel RA	75% volume pack eff	Hexagon star	-	14 x 14	7.6 x 7.6	26.6 dBi	16	K_u-band
SWOT [18]	-	2022	Panel RA	14.9x5x5m	Rectangle	600	2 x 500 x 26	2 x 595.8 x 31.0	-	35.75	K_a-band
VEMO [30]	2023	No	Miura-ori RA	16% of 1U stowage	Square	-	24.8 x 24.8	31.4 x 31.4	35.3 dBi	38	K_a-band
OSS Large [27]	2023	No	Panel RA	-	Rectangle	26	424 x 283	136.4 x 91.0	31.6 dB	9.65	X-band
GOM5-X [21]	-	due 2025	Panel RA	8 U	Rectangle	-	-	-	-	-	-
M-argo [20]	-	due 2027	Panel RA	12 U	Rectangle	-	2244	-	-	3	X-band
KaTENna [35]	2017	2017	Mesh reflector	3 U stowage	Parabolic	2.5	100	120	49.2 dB	36	K_a-band
Raincube [33]	-	2018	Mesh reflector	6 U	Parabolic	12 bus	50	59.6	42.6 dBi	35.75	K_a-band
Two freq mesh [34]	2021	No	Mesh reflector	12 U	Parabolic	-	100	23.9	36.1 dBic	7.1675	X-band
								106.7	48.4 dBic	32	K_a-band
PTR [35]	2023	No	Mesh reflector	-	Parabolic	-	300	96	48.9 dB	9.6	X-band
Torus inflatable [36]	2001	No	Membrane RA	-	Circle	1.25	100	27.7	33.7 dBi	8.3	X-band
Horseshoe [36]	2001	No	Membrane RA	-	Circle	12.8	300	320	54.4 dBic	32	K_a-band
DaHGR [38]	2016	No	Membrane RA	1.5 U stowage	Circle	-	61	20.3	34 dBi	10	X-band
Capella-1 [14]	-	2018	Membrane RA	-	-	40 (bus)	80000	-	-	-	-
R3D2 [14]–[16]	-	2019	Membrane RA	-	Circle	150 (bus)	500	-	-	-	-
LADeR [39]	2019	No	Flasher membrane RA	6U	Square	1.75	150 x 150	42 x 42	39.6 dB	8.4	X-band
Fold unit-cell[42]	2016	No	Impregnated substrate RA	under 1 U stowage	square	-	45.9 x 45.9	8.85 x 8.85	34 dBi	5.79	C-band
Double scanning RA [40]	2020	No	Solid panel RA	-	square	-	37.5 x 37.5	20 x 20	25 dB	16	K_u-band
Rollable [41]	2022	No	Membrane RA	-	Square	-	25.7 x 25.7	12 x 12	25.1 dBi	14	K_u-band
TNO membrane [6]	2024	No	Membrane RA	-	Square	0.188	55 x 55	7.6 x 7.6	25 dBi	4.15	C-band

2.6 Space Environment

Since the proposed deployable RA will be on a satellite in Low Earth Orbit (LEO) it is important to know what the expected environment is. There are several important environmental factors that play a role for the design of the deployable RA.

Thermal Cycling

Due to the satellite rotating around earth and being in and out of the eclipse shadow of earth and rotating in space thermal cycling occurs. Thermal cycling results in temperature variations during the lifetime of a satellite most of the time going within one orbit from cold to hot for example. This is something to keep in mind, especially since the area of the RA is large and most likely consists of multiple materials. To reduce thermal stresses it is thus important to choose materials with a comparable coefficient of thermal expansion (CTE) for interfaces. This results in similar deformations with the same temperature change reducing the stress.

Space Vacuum

Secondly, the near vacuum is present in space. This is relevant for outgassing of materials [43]. When the materials send to space containing trapped gas the gas wants to escape due to the pressure difference. This can be of important for sensitive instruments but also for lenses, since the gas can be ejected on the lens and contaminate the surface. In order to mitigate the outgassing there are two options. One is to only use materials with low outgas properties and the second one is a technique called outbaking. During outbaking the materials are put in near vacuum and heated above their expected temperatures, this lets the material outgas already on the ground before launch instead of in space [43]. Even though the RA itself will most likely not have issues with outgassing, other instruments on the CubeSat might be influenced by the outgassing of the RA.

Space Radiation

Besides thermal cycling and the near vacuum there is also space radiation. There are several kind of radiation present in space. UV radiation, Solar Partical Events (SPE), Galactic Cosmic Radiation (GCR) and the radiation belts are the relevant kinds of radiation [43].

UV radiation mostly only darkens the materials, but it can have a bigger impact on polymers. UV has a energy range from 3 - $125\,\mathrm{eV}$, hence it is high enough to break the most typical molecular bonds but especially the weakest type of bonds which are present in polymers [44]. UV radiation can either cross-link (strengthen) or chain scission (weaken) the polymer. Since this radiation comes from the sun and is only influenced by the suns activity the RA will almost constantly be subjected to this kind of radiation except when being in eclipse.

Besides the constant UV radiation the sun also ejects corona mass ejections. These irregularly eject a composition of protons and heavy particles which result in a SPE. SPE energy can range from 10-$1000\,\mathrm{MeV}$, much higher than the constant UV radiation. GCR is constantly present in space. This is low flux but very consistent compared to SPE. These have extremely high energy, GeV (10^9)- TeV (10^{12}), and mostly consist of protons.

The last type of radiation are the radiation belts around earth also called the van Allen Belts. It consist of two belts, the inner and outer belt and are situated rotational around the earths axis. The inner belt consist primarily out of protons, while the outer belt consist mainly out of electrons. These belts contain particles due to the sun radiation and they are trapped due to earths magnetic field. Their altitude varies due to the intensity of the sun. Various numbers are mentioned ranging from $600\,\mathrm{km}$ to $6000\,\mathrm{km}$ [45] -[46].

In general, one can protect to a certain extent against space radiation. The easiest way is by applying a thick layer of material, but it is hard to protect against the high energy particles when using a small amount of mass. The more energy a particle has the more material is needed to stop it, but since the

array is lightweight and has a high surface area a lot of weight needs to be added if one wants to protect against all kind of radiation.

Other possible issues that can arise from space radiation are: spacecraft charging, total ionising dose limit, single event effects, displacement damage and polymer cracking [44]. Spacecraft charging happens due to the electrons that build up on the outside of the spacecraft. Once the external or internal charging reaches a threshold electric current can be generated. These can cause short-circuit or glitches in electronic systems but also physical damage to coatings and materials. One cannot prevent the build up of charge but might limit its effects by choosing conductive materials where possible and opt for a defensive design.

Total ionining dose is the long-term effect of radiation energy build-up over time in electronics altering the charge of circuits and is the primary degradation mechanism for circuits in space.

When a charged particle passes through electronics it can disrupt electrons and this can cause a unpredictable glitch. Different events include: a temporary glitch, a permanent glitch and the destruction of the device.

Displacement damage is caused by protons and heavy ions. These hit atoms in the material causing the displacement of these atoms and to move location. On bulk materials this has a negligible effect but on sensitive electronics this might cause significant effects.

Heavy particle radiation can result in the cracking of polymer films. The thinner the film the easier cracks occur. Polymer films are frequently applied on the outside of the spacecraft as for example coatings or insulation. The cracking of polymer films can be enhanced by atomic oxygen (AO).

Atomic Oxygen

Due to the light in the atmosphere there is AO present in LEO. As can be seen in Figure 2.24, the amount of AO is still significant till higher LEO altitudes, while other sorts of atmospheric components are decreasing in density. AO is formed due to light that has a high enough energy to break the O_2 bond. Once broken AO is formed. AO can react with materials causing oxidation with metals but also erosion on polymers. The oxidation erosion yield is used to quantify the reaction of materials with AO. The AO erosion yield is the volume of a material that is removed (through oxidation) per incident oxygen atom, according to [47]. When a low AO reaction is desired a low erosion yield is needed. A coating with a low erosion yield could however be applied such that the underlying material is protected from the AO.

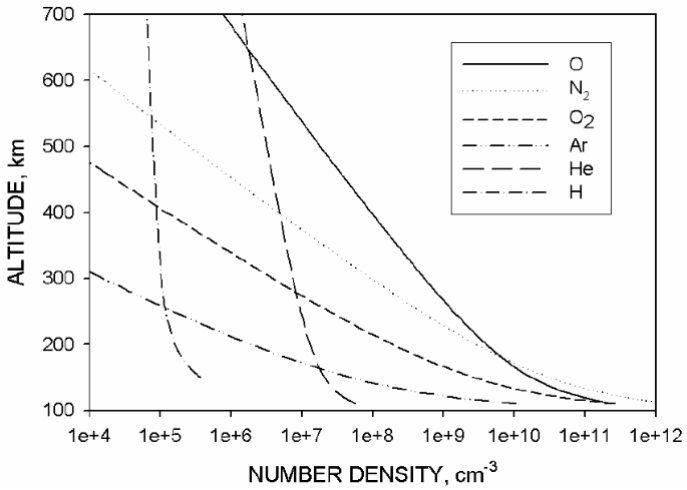

Figure 2.24: Variation of atmospheric element density with altitude. Adapted from [47].

Micro Meteorites and Orbital Debris

Lastly there are the Micro Meteorites and Orbital Debris (MMOD). These are high velocity particles of various sizes. Micro Meteorites are natural occurring particles in orbit around the sun and Orbital Debris are man-made objects in orbit around earth. MMOD can be dangerous due to their high velocities even though they can have low mass. Since the energy of particles scales squared for velocity and to the third power for mass, even small particles can thus have massive impact [44]. There are three ways to protect against MMOD. First, one can add a thick layer that absorbs the energy of the MMOD, but this results in lots of added mass. The second option is to add a more lightweight solution consisting of multiple layers, called a whipple shield [44]. However, this also adds a lot of mass compared to a low mass RA. The third solution is selecting an altitude at which the amount of MMOD is low, which reduces the chances of impact. The spatial density plotted against altitude can for MMOD can be observed in Figure 2.25. This plot indicates that the highest amount of MMOD is between an altitude of $700\,\mathrm{km}$ and $1000\,\mathrm{km}$.

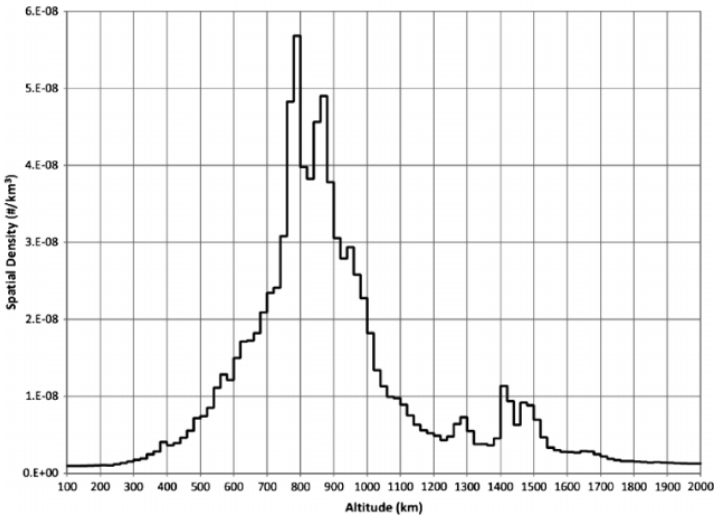

Figure 2.25: Variation of spatial density with altitude. Adapted from [48].

2.7 Requirements on the System

From TNO requirements have been given on which the deployable RA has to satisfy. These range from orbital requirements to material restrictions. In Table 2.2 the most important requirements are mentioned where each requirement has its own identifier and a short rational.

Table 2.2: Design requirements for the deployable reflectarray antenna.

ID	Requirement	Rational
Sys-001	The system shall have a peak gain of $36\,\mathrm{dB}$.	A certain signal amplification is required to get good performance.
Sys-002	The focal length over the diameter of the reflectarray ratio for the system shall be 0.85.	In order for the signal to transition from the near to the far field a certain distance is required. This is mostly done by a f_d/D_a ratio. Here f is the focal length and D is the diameter of the array.
Sys-003	The altitude of the satellite on which the system is connected shall be between 550 and $500\,\mathrm{km}$.	The satellite will operate in LEO to get good coverage of earth while having a short distance from earth and quick revisit times.
Sys-004	The system shall follow a sun-synchronous orbit.	A sun-synchronous orbit will ensure a very stable orbit over the course of the lifetime of the satellite. Besides this the satellite will be at the same ground track position at the same local mean time every day.
Sys-005	The system shall consist of one reflectarray surface and one illuminating feed source.	In order to simplify the antenna design only one reflectarray surface and one feed source will be considered.
Sys-006	The system shall have a expected lifetime of at least 5 years.	To ensure return on investment and mission viability a certain lifetime is required. This has been set to a minimum of 5 years.
Sys-007	The pointing of the beam shall be at $-30\,°$ relative from the middle of the reflectarray along the width of the array.	An advantage of a reflectarray is that it can point the main lobe in different directions. To get no interference this angle is set to $-30\,°$.
Sys-008	The feed shall be located $15\,°$ relative from the middle of the reflectarray along the width of the array.	To make use of the advantage of the no interference of the beam pointing the feed has been moved in the opposite direction.
Sys-009	The angle of incidence of the beam impacting the earth surface shall be between 20 and $40\,°$.	This is a requirement given to ensure good antenna performance for the scanning of the earth.
Ar-001	The reflectarray RF surface shall consist of two membranes with no electrical conductive connection between them.	In order for the reflectarray to not short circuit two membranes are required where there is no electrical conductive connection between the two.
Ar-002	The top layers shall be made from copper for each of the two membranes.	Copper has been chosen since it is a good electrical conductive material and the working basis of the reflectarray.
Ar-003	The copper layers in the membrane shall be $17\,\mu\mathrm{m}$ thick.	This is currently the thickness used in the prototype and not to be changed.
Ar-004	The reflectarray RF surface shall have a surface accuracy of $0.5\,\mathrm{mm}$.	This surface accuracy was measured on the prototype and it still gave good performance.
Ar-005	The tolerance between the two membranes of the reflectarray RF surfaces shall be 1/200 of the free space wavelength.	This tolerance was obtained by TNO with the use of modeling software on the prototype.
Ar-006	The deformation in the fully deployed state of the RA shall be a maximum of 1/16 of the free space wavelength in out of plane direction.	This requirement was presented by TNO to ensure a good enough far field radiation pattern.
Ar-007	The stresses in the reflectarray surface shall remain below the yield stress at all times.	Due to the stresses not reaching yield stress no plastic deformation occurs, ensuring that the intended shape remains.

2.8 Conclusions from Literature Study

Concluding from the recent missions using a RA, the concept of a deployable RA is being used more and more in all kind of forms. However it is still not conventional to use RA as antennas as only a few missions have used one. This suggests work still needs to be done in order to make it easier to use it

on space missions.

There are two main kinds of RAs but they work the same. On one hand there are membrane RA antennas which consist of thin layers that need some kind of tensioning system to keep the required shape. On the other hand there are solid panel RAs which have support structure between the patches and the ground plane. There are also lots of different deployment options, which can be grouped roughly in the following categories:

- Solid panel conventional folding (e.g. ISARA)
- Solid panel origami inspired folding (e.g. Miura-ori and solid flashers)
- Membrane tensioning systems (e.g. Inflatable torus)
- Deployable membrane flashers (e.g. LADeR)

Chapter 3

Concept generation

In order to make a well-considered choice between the concepts, a wide range of possible options is evaluated. First, various positional configurations are presented in Section 3.1. These configurations are then compared in a trade-off analysis in Section 3.2. The three most promising concepts are subsequently combined with deployment options, as described in Section 3.3, and finally evaluated in Section 3.4 to select a single concept to use in the remainder of the thesis.

3.1 Position configurations

Requirement Sys-002 states that the focal distance between the reflective surface and the feed shall be 0.85 times the aperture size of the array. With a diameter of 2.5m this would result in a focal distance of 2.125 m. Together with requirement Sys-008 that states that the feed should be located at 15 degrees from the midpoint along the width of the array, a fixed point has been obtained for the feed position relative to the array. Besides the location of the feed also the reflection angle is known from requirement Sys-007. This requirements states that the pointing shall be at -30 degrees relative to the width of the array. An visual overview of the previously described situation can be observed in Figure 3.1a.

From this starting position numerous options are possible for configurations with the location and orientation of the satellite. In order to maintain performance of the antenna and avoid shadowing, it is desired to place the satellite outside of the illuminating rays of the feed and desired direction of the reflection of the array. This eliminates the red shaded area in Figure 3.1b for placement of the satellite, since this will drastically lower performance of the antenna due to the satellite interfering with the EM waves.

When the satellite is in front of the array, but outside the red shaded area it reflects the EM waves from the RA back onto the RA. This basically means that there is a second feed illuminating the array, even if it is with very low strength. This will reduce performance of the signal, so these are also undesired position. It will however be possible to chose different kinds of coatings or materials to limit the reflection as much as possible, meaning this area is still a valid option to place the satellite. This area is shaded with the color orange in Figure 3.1b. The best possible position is when it is positioned behind the RA. This is shaded with the color green in Figure 3.1b, and here the satellite will not interfere with the EM waves.

Considering potential satellite placements in the green and orange areas, the satellite can be regarded as an anchor point to which both the RA surface and the feed must be connected. To avoid impacting the performance of the RA, support structures should ideally not be placed in the red and orange shaded areas, as their impact on performance is currently unknown.

However, it is considered acceptable to place structural elements in these regions, given that their reflective surface area is likely minimal. Based on these considerations, several positional concepts have been developed. Each concept will be briefly introduced, along with its respective advantages

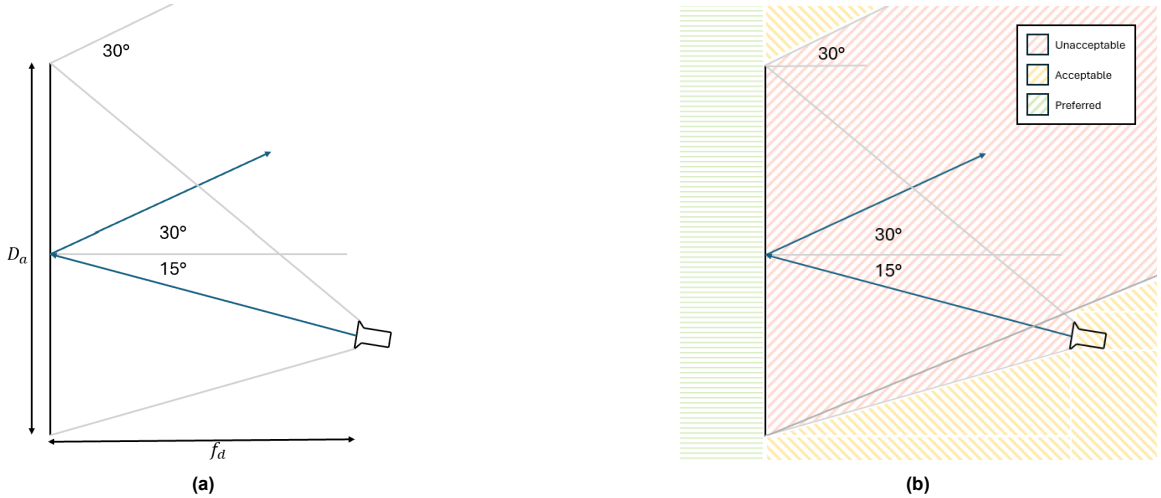

Figure 3.1: (a) Placement of the feed relative to the reflectarray, determined by design requirements. (b) Evaluation of satellite positioning options based on criteria such as signal quality and occurring reflections

and disadvantages. It should be noted that only the RA and the satellite are considered and the constraints introduced earlier. Any other satellite systems and its accompanying constraints, for example placement of solar panels or clear view for a camera, are left out of the concept generation process.

Positional concept #1

The first concept has the satellite positioned in the orange area. Both the feed as the RA surface have support structure to connect it to the satellite. The satellite is placed in a position that both the support structures extrude orthogonal from the satellite. The support structure connecting, the satellite with the RA surface is at the bottom and not the center of the RA to limit the interference. In the center the EM are going to be the strongest. Placing support structure here would create maximum interference. There might be additional support structure required behind the RA surface which is indicted by the dashed line. The concept can be observed in Figure 3.2a.

Advantages;

+ No extremely long distances required for both support structures.
+ Material is placed far away from red shaded area. Reducing the impact on performance as much as possible.
+ Straight support and orthogonal connections to the satellite, reducing complexity of the satellite connection.

Disadvantages;

- Two connections and support structures needed for both the RA surface and the RA feed.
- Storage and deployment of RA surface could be complex and heavy due to distance from the satellite.
- Two sources of instability of the system due to two support structures.
- Satellite present in the orange shaded region.

Positional concept #2

The easiest way to negate one of disadvantages of concept #1 is to relocate the satellite as close as possible to the feed. This results in only one sources of instability, but results also in a longer connection between the RA surface and the satellite. This means that the deployment of the feed in this configuration is the least complex possibility. If however, the RA surface needs to be connected at the center of the surface a very sharp angle is needed to make the support structure go behind the

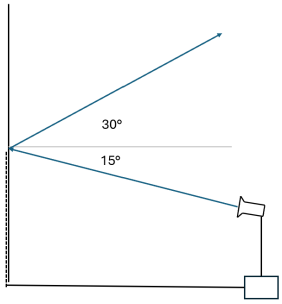

(a) Concept 1: Satellite with orthogonal support structures minimizing interference, additional supports indicated by dashed lines.

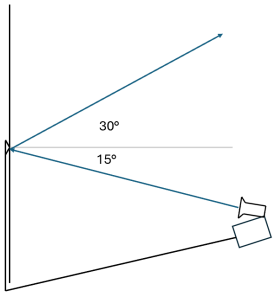

(b) Concept 2: Satellite close to feed removing one support, but still minimizing interference.

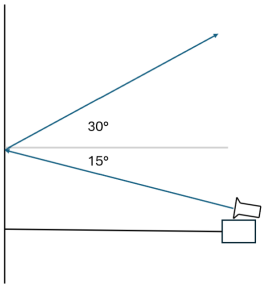

(c) Concept 3: Satellite close to feed removing one support, without minimizing interference.

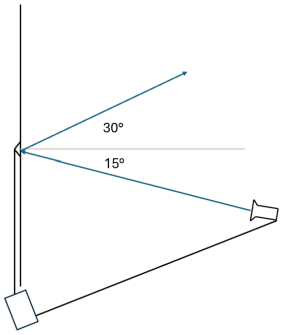

(d) Concept 4: Satellite beneath RA, orthogonal connection to feed support.

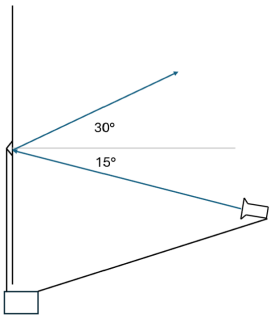

(e) Concept 5: Satellite beneath RA, orthogonal connection to RA support.

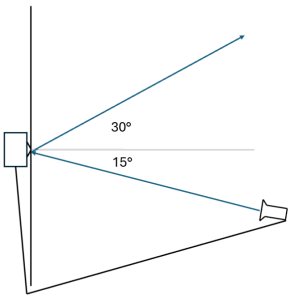

(f) Concept 6: Satellite close to RA, removing one support, minimizing interference.

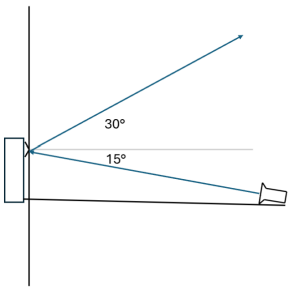

(g) Concept 7: Satellite close to RA, removing one support, without minimizing interference.

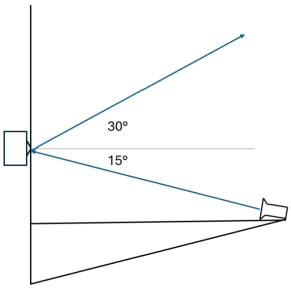

(h) Concept 8: Satellite close to RA, eliminating one support, feed support connected to RA.

Figure 3.2: Overview of all considered positional configurations, each accompanied by a brief description.

array. This is needed to not let the support structure interfere with the performance of the antenna and increase the stability of the RA surface. This concept can be observed in Figure 3.2b.

Advantages;

+ No support structure required for the feed connection, removing one source of instability in the system.
+ No support structure in the red shaded area.
+ Only support straight and orthogonal connected to the satellite, reducing complexity of the connection with the satellite.

Disadvantages;

- Storage and deployment of RA surface even more complex and heavy due to distance compared to concept 1.
- A sharp corner is present in the support of the RA decreasing stability of the system and adding deployment complexity.

Positional concept #3

To remove the sharp corner from concept #2 the RA could be attached on the front side to the support structure. This should make deployment and storage less complex. However, the support structure is now in the direct beam of the feed, reducing performance. The connection point of the support structure to the RA surface can be alongside all of the front side of the array, but this is going to be a complex connection. Besides complexity also the performance will be reduced since patches need to be removed to accommodate the connection. The concept can be observed in Figure 3.2c.

Advantages;

+ No support structure required for the feed connection, removing one source of instability in the system.
+ Straight support and orthogonal connections to the satellite, reducing complexity of the connection with the satellite.
+ Support structure of the RA surface is shorter than #2 and without a sharp corner

Disadvantages;

- Storage and deployment of RA surface is still complex and heavy due to distance from satellite.
- Support structure reduces performance of antenna due to shadowing
- The connection of the RA surface results in removing patches.

Positional concept #4

Instead of placing the satellite closer to the feed, also the option of moving it closer to the RA should be considered. Now the satellite is partly behind the RA with a shorter length of support structure for the RA. Also no kinks are present in the support structures of both the RA and the feed resulting in less complex deployment. The support structure exits the satellite orthogonal for the feed support and at a different angle for the RA surface. The concept can be observed in Figure 3.2d.

Advantages;

+ Reduced weight of the deployment system of the RA surface since it is closer to the satellite compared to the previous concepts.
+ No support structure in the red shaded area.
+ Straight support and orthogonal connections to the satellite of the RA feed support structure.
+ Satellite has little interference with performance of RA antenna due to it being underneath the RA.

Disadvantages;

- Stability is decreased due to multiple support structures, this also makes deployment and stowage more complex.
- RA surface support connection to the satellite is not orthogonal.

Positional concept #5

This concept is similar to concept #4, but the satellite is rotated such that the connection of the RA support structure is now orthogonal. This should reduce complexity since the heavy RA surface has now a orthogonal connection. As a result now the feed connection is not longer orthogonal. The concept can be observed in Figure 3.2e.

Advantages;

+ Lower amount of support structure needed for the RA surface compared to previous concepts since the heavy RA surface is closer to the satellite reducing weight of the deployment system
+ No support structure in the red shaded area.
+ Straight support and orthogonal connections to the satellite of the RA surface support structure.
+ Satellite has little interference with performance of RA antenna due to it being underneath the RA.

Disadvantages;

- Stability is decreased due to multiple support structures, this also makes deployment and stowage more complex.
- RA feed support connection to the satellite is not orthogonal.

Positional concept #6

In order to ease deployment and reduce structural mass of the RA surface the satellite could be placed behind the center of RA. This means that there is no influence of the satellite on the performance of the antenna. There is still however a need to connect the feed to the satellite. Opting for a configuration where the support structure stays out of the red shaded area the current concept was created. This means a structure to support the feed is required that is deployable but also has a deployed state which goes around the RA. The concept can be observed in Figure 3.2f.

Advantages;

+ Deployment of RA surface is less complex also reducing mass due to it being close the satellite.
+ No support structure in the red shaded area.
+ No reduction on performance of the satellite.

Disadvantages;

- Stability of long structure might be outside tolerances of the feed.
- due to long distance of feed support mass is increased.
- Sharp corner present in support structure of the feed.

Positional concept #7

To negate the long support structure of concept #6 one can opt for the support structure of the feed to go through the RA surface. This results in easier deployment of the feed due to the sharp corner not being present. This however obviously means a hole is required to move the feed through in the RA surface which is undesirable since there will be less RA area. This will reduce performance of the antenna. Besides this also the support structure itself will interfere with the performance, but to what extent still needs to be determined. The concept can be observed in Figure 3.2g.

Advantages;

+ Even shorter support structure for the feed
+ Deployment of RA surface is less complex since satellite is close

+ Straight support and orthogonal connections to the satellite of the RA surface support structure.
+ Satellite has no interference with performance of RA antenna due to it being underneath the RA.

Disadvantages;

- A hole will be present in the RA reducing performance of the antenna.
- Support structure will be in the red shaded area.

Positional concept #8

It might be possible to connect the feed to the RA and the RA to the satellite. Reducing the distance of deployment of the feed. This would make deployment more complex, but could reduce the total amount of mass. The concept can be observed in Figure 3.2h.

Advantages;

+ Reduces amount of structural material as much as possible.
+ No support structure in the red shaded area.
+ Deployment of RA surface is less complex since satellite is close.
+ Satellite has no interference with performance of RA antenna due to it being underneath the RA.

Disadvantages;

- Deployment becomes complex, since everything is connected to each other.
- Stability of the system is reduced due to the sequential connections.

3.2 Positional configuration trade-off

In order to chose the best options for the positional concepts, a trade-off has been performed. Each of the concepts is graded on a scale of 1 to 5 with steps of 0.5 on four parameters. The higher the grade the better the concept scores on that respective parameter. The parameters used in this trade-off are: Complexity, Mass, Stability and Antenna performance interference/reduction. Complexity has been chosen since this includes for example complexity of deployment and connection points. Since deployment complexity drives a lot of the design, complexity was deemed as the most important trade-off parameter with a weight of 30%. Mass and stability were both deemed important parameters as well. Since it is a big structure mass can quickly add up. This should be low to reduce launching cost. Stability is important to have a properly working RA. If stability it not good enough it can result in a low performing RA, which is undesired. Both mass and stability were assigned a weight of 25% in the trade-off. Lastly antenna performance interference/reduction is deemed important. One of the reasons to use a off fed feed is to utilize the option of reducing blockage due to support structure. This will improve the performance of the antenna. To get as much use out of the deployed area any performance reductions should be tried to limited as much as possible. Because of these reasons a weight of 20% was assigned to this parameter. The trade-off table for the positional concepts can be observed in Table 3.1. In the most right column the final weighted scores for each concept is calculated.

Based on the scores for each concept a few of the best scoring concepts are selected to continue the work on, in this case the best four are selected. The best four scoring concepts are concepts # 5, 8, 7 and 4, in order of best scoring to worst. Since however, concept 4 and 5 are very similar and 5 scores better, concept 4 is disregarded as a winning concept. The winning concepts are thus concepts 5, 8, and 7, or from now on called concept A, B and C. The best positional concepts can again be observed in Figure 3.3.

Table 3.1: Trade-off weights for eight positional concepts. The rightmost column shows the weighted average, representing the trade-off outcome.

Concept #	**Complexity**	**Mass**	**Stability**	**Antenna Performance Interference/Reduction**	**Final Score**
Weight	30%	25%	25%	20%	
1	3	2.5	2.5	3	2.75
2	1	1	2	3	1.65
3	2	2.5	2	1	1.93
4	2.5	3.5	3	3	2.98
5	3	4	3	3	3.25
6	1	3	2	5	2.55
7	2	5	4	1	3.05
8	2	3	3	5	3.1
	1 = high complexity	1 = high mass	1 = low stability	1 = lots of interference	
	5 = low complexity	5 = low mass	5 = high stability	5 = no interference	

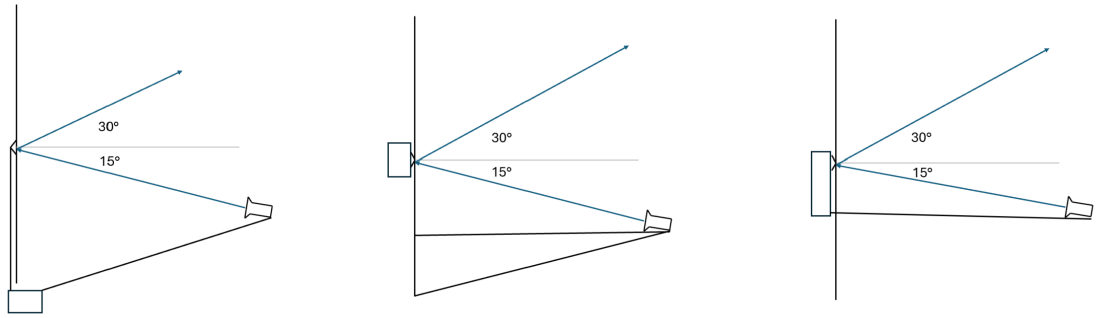

(a) **(b)** **(c)** Concept 7/Concept C

Figure 3.3: Top three positional concepts selected based on trade-off analysis results: (a) Concept 5/Concept A, (b) Concept 8/Concept B, and (c) Concept 7/Concept C.

3.3 Deployment combined with position concepts

Now the positional concepts have been determined different deployment options will be considered as well. From the literature study six deployments have been identified that are relevant. These are (grouped in solids and membrane deployments):

- Solids
  - Origami inspired flashers
  - Regular panels in orthogonal folding
  - Origami inspired Miura-ori
- Membranes
  - Inflatable
  - LaDeR inspired
  - Tensegrity/pulley inspired.

With solid deployable RA, a RA is meant where it consists of multiple smaller segments, where each of these segments are not supposed to be foldable or flexible. Membrane RAs consist of one piece of membrane where the deployment consist mostly of the support structure around the membrane to deploy. Once deployed, the support structure puts tension on the RA to keep it flat and have ideally no wrinkles occur. Simultaneously with the deployment of the support structure of the membrane is the

unfolding of the membrane itself. This has to happen in such a way that no entanglement occurs and the membrane deploys fully.

All of the above mentioned deployment options are considered for Concept A and C. For Concept B only an inflatable is considered since the other deployment options make it too difficult to combine the deployment of the RA surface and the feed. To chose what deployment is best, again a trade-off will be performed, but with more parameters than the first trade-off. All trade-off parameters can be grouped in the following four main parameters:

- Product feasibility
- Satellite constraints
- Complexity (deployment reliability)
- Antenna performance

Table 3.2: Trade-off parameters and their assigned weights.

Product feasibility	Weight	Satellite constraints	Weight	Complexity (deployment reliability)	Weight	antenna performance	Weight
Manufacturing	10.71%	Packing efficiency	17.86%	Modularity	10.71%	Expected thermal stability	17.86%
Flight heritage	3.57%	Expected mass	10.71%	Inter connectivity	3.57%	Patch grid intactness	10.71%
				Integration effort	7.14%	Feed influence	7.14%
Total	14.29%	Total	28.57%	Total	21.43%	Total	35.71%

Each of the main parameters has multiple sub-parameters. All of the sub-parameters with their respective weights are presented in Table 3.2. The weights have been determined through active discussions with TNO. ”Antenna performance” was deemed most important, since making the RA deployable still should result in a good performing antenna. Second is ”Satellite constraints”, this is important since a good packing efficiency is desired, while keeping an eye at the total mass. And lastly there is ”Complexity” and ”Product feasibility”. Of these ”Complexity” was deemed more important since a high deployment reliability is desired. This is hard to determine at the moment, so it is addressed indirectly through the other sub-parameters.

The weights used in the trade-off range from ”1” to ”5” with a step sizes of ”0.5”. Here ”1” will result in the worst score while ”5” being the best. For the parameter ”Satellite constraints” a comparative study has been performed on data available in the literature. For the other parameters comparative scores have been determined based on reasoning and logic.

3.4 Deployment combined with position concepts trade-off

With the trade-off parameters, their weights and the concepts to consider known, the trade-off can be filled in and analysed. The final scores of each concept is presented in Table 3.3, together with the scores it got for each of the four main parameters. Table 3.3 is a summary on the complete trade-off, this complete trade-off can be found in Appendix A. In Table 3.3, a column is present called ”Kind of deployment actuation”. The deployment actuation’s relevant for each deployment have been extracted from the framework developed by Sauder et al. [49]. Based on each deployment type different actuation’s have been identified as a good starting point for designing and these have been considered in this trade-off. Please note that the percentage weights used in the trade-off analysis differ slightly from those mentioned earlier. This is because the weights have been rounded to improve readability and presentation, but the final scores are still for the original non-rounded values.

Based on the performed trade-off a few conclusions can be drawn.

- Positional concept B performs poorly across all parameters except antenna performance. This is primarily because the feed support structure is connected to the RA, which increases complexity

and complicates manufacturing. Additionally, the requirement for a gas canister limits the potential benefits of its high deployment efficiency.

- In general, solid configurations offer higher product feasibility. This is primarily due to the manageable sizes of the required components, producing multiple medium-sized pieces is easier than manufacturing a single large sheet on size-limited machines. As a result, solids perform better in this aspect.
- Configuration A generally performs better than Configuration C, primarily because it lacks the hole which is present in Configuration C. This absence contributes to improved stability and greater reliability.
- Configuration A with panels achieved the highest overall score, primarily due to strong performance in product feasibility, complexity, and antenna performance. However, if satellite constraints had been weighted more heavily in the evaluation, its ranking would have been lower. This is because the panel thickness of $3.71\,\mathrm{mm}$ leads to inefficient use of storage volume, negatively impacting its score in that category.
- Conversely, while the panel-based configuration scores lower on satellite constraints, the LADeR concept performs best in this category. It achieves the highest score due to its very high volume efficiency and lightweight design. However, LADeR scores only average or slightly below average on the other parameters. Additionally, the design requires the removal of several patches, which reduces antenna performance compared to other concepts—preventing it from being the top-scoring design overall.
- The four top-performing designs in the trade-off analysis are quite similar. The highest-scoring design is Configuration A with panels, followed by the LADeR design using Configuration A, Configuration C with panels and a hole, and finally the LADeR design using Configuration C with a hole. This indicates that, regardless of the configuration type, both panel-based and LADeR concepts perform well in this trade-off.

The best scoring concept from the trade-off, Configuration A with panels, will be used to continue the thesis work. It is believed that lessons learned from studying this concept will be applicable to most of the other concepts in the trade-off as well. An artist impression of the fully deployed RA can be observed in Figure 3.4, visualizing the best scoring concept from the trade-off. Here the RA consists of 11x11 panels where each panel would then have 5x5 patches on it. Any patch regardless of the size is assumed to need a space of 45 mm to work properly, hence a panel of 5x5 patches has a size of 225 mm. This results in a value very close to 2.5 x $2.5\,\mathrm{m}^2$ by TNO. The CubeSat is assumed to have a size of 6U to give it a sense of scale to the size of the RA, but this is not the definitive size of the CubeSat.

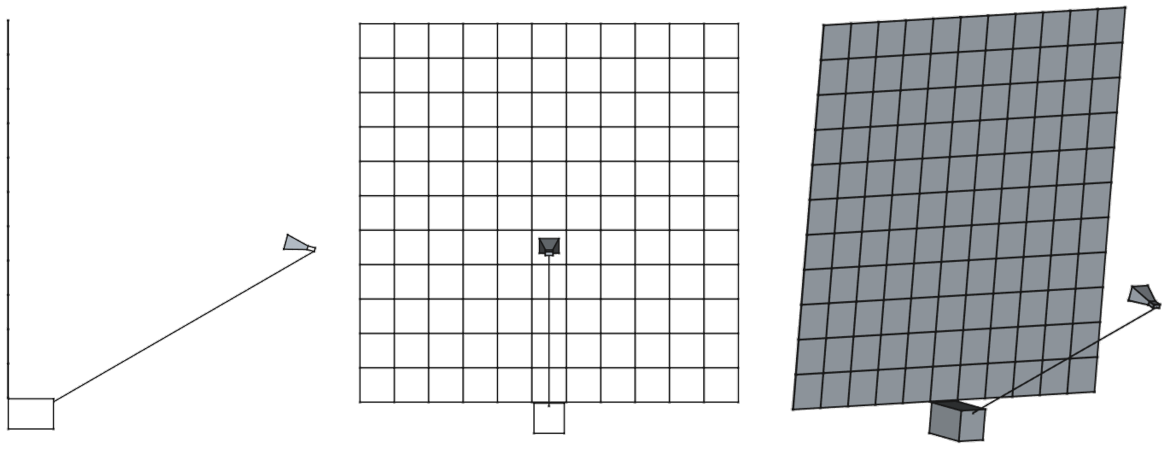

Figure 3.4: Side, front, and isometric views of Configuration A, featuring an 11×11 panel array including 5×5 patches per panel. A 6U CubeSat is shown for scale reference. Made with FreeCAD [50].

In order to make the membranes into a panel, a frame is added along the edges of the membranes. In order to chose a good material for the frame it is important to remember the environment the panel will be in, space. As was mentioned in the literature study there are two main things to take into

consideration to choose a material: AO and space radiation. With AO it is vital to look at the erosion yield of the material. It can be found that the erosion yield of aluminum is near zero [44]. Besides this it is also a very lightweight material with a lot of flight heritage. Making a good choice to be the frame material. It can also observed that the membranes seem to be quite resistant as well against the AO. With copper having a erosion yield of $0.0064 \cdot 10^{-24}$ and polyimide (or kapton H) an erosion yield of $3 \cdot 10^{-24}$. This means that the polyimide layer will degrade earlier than the copper, which is the second best scenario. The best scenario would be no degradation at all. Also space radiation need to be looked into. According to [44], metals are unaffected by UV radiation. Making aluminum a good choice as a frame. This also means the copper will be unaffected. Polymers like polyimide are however susceptible to UV radiation. Cross-linking or chain scission might occur, as well as surface erosion and reflectivity changes. Lastly it should be noted that due to the size it is impossible to shield everything of the RA against MMOD. Also, adjustments need to be made for attitude control due to the large size of the RA and it accompanying drag in orbit and moment of inertia.

Table 3.3: Top configuration concepts from the configuration trade-off, including deployment types. Color coding indicates relative scores per column, with green representing the highest and red the lowest.

Deployment type	RA type	Kind of deployment actuation	Final score	Product feasibility	Satellite constraints	Complexity (deployment reliability)	Antenna performance
				15.00%	30.00%	20.00%	35.00%
Configuration A							
Flasher	Solid	Rotation	2.55	0.43	0.80	0.39	0.93
Panels	Solid	Springs	3.52	0.71	0.38	1.00	1.43
Miura-ori	Solid	Strain energy/motors	3.13	0.54	0.86	0.61	1.13
Inflatable	Membrane	Gas pump	2.63	0.32	0.45	0.50	1.36
Pully/tensegrity	Membrane	Motor	2.52	0.39	0.52	0.61	1.00
LADeR	Membrane	Motor/BI-STEM	3.39	0.32	1.32	0.68	1.07
Configuration B							
Inflatable	Membrane	Gas pump	2.27	0.27	0.45	0.36	1.20
Configuration C							
Flasher	Solid	Rotation	2.52	0.39	0.86	0.39	0.88
Panels	Solid	Springs	3.32	0.63	0.38	0.95	1.38
Miura-ori	Solid	Strain energy/Motor	2.93	0.45	0.86	0.55	1.07
Inflatable	Membrane	Gas pump	2.55	0.29	0.45	0.61	1.21
Pully/tensegrity	Membrane	Motor	2.23	0.36	0.52	0.63	0.73
LADeR	Membrane	Motor	3.21	0.29	1.43	0.57	0.93

Chapter 4

Methodology

This chapter outlines the methodology used to evaluate both the thermal and mechanical behavior of the system. The analysis is divided into two main categories: thermal behavior studies and mechanical aspect studies.

The thermal analysis begins with a reference case in Section 4.1, where the panel is assessed without any design optimizations. In Section 4.2, variations in key parameters, such as radiative and conductive links, panel orientation, size, and quantity, are introduced.

The mechanical analysis focuses on two phenomena. First, thermo-elastic deformations, which describe the elastic response of materials to temperature changes, are examined in Section 4.3. Second, the mechanical effects of deployment activation are introduced in Section 4.4

4.1 Orbital Thermal Loads

Since the RA will orbit earth in a Sun-Synchronous Orbit (SSO), thermal cycling will be present. It is unclear what the exact orbit is going to be for the RA. However, the influence of changing thermal parameters will be the same regardless of the type of orbit chosen. The main influences on the behavior are the radiative link parameters and the conductive link parameters. Recalling the equation for thermal stability:

$$Q_{in} = Q_{out} \tag{4.1}$$

In space the heat sources going into the system are: direct sunlight, albedo (reflected sunlight from earth) and infrared (IR) radiation from earth, while the heat is ejected through radiation to deep space. In equation form this can be written as:

$$Q_{in} = Q_{sun} + Q_{albedo} + Q_{IR} \tag{4.2}$$

$$Q_{out} = Q_{DS} \tag{4.3}$$

To gain a deeper understanding of thermal behavior in space, it is essential to first grasp the fundamental concepts of general heat transfer principles. Heat transfer can occur in three ways, through radiation, convection and conduction [51]. In space there is the near vacuum, which means that convection is not an applicable heat transfer mechanism. This leaves only radiation and conduction as heat transfer mechanisms in space. Recalling the equation for conductive heat transfer in a solid for a 1D case [51]:

$$Q_{conductive} = \frac{k_{12}A}{L_{12}}(T_2 - T_1) \tag{4.4}$$

Here k_{12} is the material thermal conductivity from place 1 to 2, A is the area of the solid, L_{12} the length of the solid between place 1 and 2 and T_2 and T_1 the temperatures at position 1 and 2. In order to get better conductivity either the material can be changed to have a higher thermal conductivity, the area can be increased, the length made shorter or the temperature difference bigger.

Radiative heat transfer occurs across different wavelengths depending on the temperature of the radiating body. The total radiated power follows a fourth-order power law known as the Stefan–Boltzmann Law, which assumes a black body. A black body is a perfect emitter and absorber of radiation. The law is expressed as [51]:

$$Q = A\sigma T^4 \tag{4.5}$$

Here, A is the surface area of the body, σ is the Stefan–Boltzmann constant ($5.67 \cdot 10^{-8}\ \mathrm{W/m^2K^4}$), and T is the absolute temperature of the body in Kelvin. In real-world scenarios, most objects are not perfect black bodies. To account for this, the law is modified to include the emissivity ϵ, which ranges from 0 to 1. An emissivity of 1 corresponds to a perfect black body. Similarly, the absorptivity α describes how much incident radiation a surface absorbs. For a given wavelength, Kirchhoff's law of thermal radiation states that absorptivity and emissivity are equal:

$$\alpha(\lambda) = \epsilon(\lambda) \tag{4.6}$$

However, since the wavelength of emitted radiation depends on the temperature of the radiating body, the relevant values of α and ϵ vary across spectral bands. In this context, absorptivity α refers to the solar spectrum (shortwave radiation), while emissivity ϵ refers to the thermal infrared or ambient spectrum (longwave radiation).

The equation describing the heat transfer between two radiating bodies is as follows:

$$Q_{radiative} = \epsilon_{effective}\sigma F_{12} A_1 (T_1^4 - T_2^4) \tag{4.7}$$

Here $\epsilon_{effective}$ is described by the following equation:

$$\epsilon_{effective} = \frac{1}{\frac{1}{\epsilon_1} + \frac{1}{\epsilon_2} - 1} \tag{4.8}$$

F_{12} is the view factor between body 1 and body 2. The view factor is the fraction of radiation reaching body 2 as emitted from body 1.

Now going back to the different types of heat inputs in the system and radiated heat output the following equations can be set up for each of the terms.

$$Q_{sun} = \alpha \cdot SC \cdot F_{sun\_spacecraft} \cdot A_{sun} \tag{4.9}$$

Here α is the absorptivity of the area the solar radiation hits, SC is the solar constant, F the view factor from the sun to the spacecraft and A the area the solar radiation hits.

$$Q_{albedo} = \alpha \cdot a \cdot SC \cdot F_{earth\_spacecraft} \cdot A_{albedo} \cdot cos(\phi) \tag{4.10}$$

Here α is the absorptivity of the area the albedo radiation hits, a is the albedo reflection coefficient of earth, SC is the solar constant, F the view factor from the earth to the spacecraft and A the area the solar radiation hits and ϕ is the solar zenith angle.

$$Q_{IR} = \epsilon \cdot \sigma \cdot F_{earth\_spacecraft} \cdot A_{IR} \cdot (T_{earth}^4 - T_{spacecraft}^4) \tag{4.11}$$

Here ϵ is the emissivity of the area the infrared radiation hits, σ is the Stephen-Boltzmann constant, F is the view factor from earth to the spacecraft, A the area the infrared radiation hits and T is the temperature of the objects.

$$Q_{DS} = \epsilon \cdot \sigma \cdot SC \cdot F_{spacecraft\_DS} \cdot A_{DS} \cdot (T^4_{spacecraft} - T^4_{DS}) \tag{4.12}$$

Here ϵ is the emissivity of the area the radiation is emitted from the body, σ is the Stephen-Boltzmann constant, F is the view factor from the spacecraft to deep space, A the area emitted radiation hits and T is the temperature of the spacecraft and deep space.

In order to determine the orbit to analyse the system a few orbital parameters need to be known. With one of the most important ones the inclination. This can be extracted from requirements Sys-003 and Sys-004, indicating that the orbit followed by the system is a SSO at a starting altitude of $550\,\mathrm{km}$ with orbital decay going down to an altitude of $500\,\mathrm{km}$. It is assumed that the orbit is circular, to make interpretations of the results more straightforward. In order to have a SSO, the orbit has to rotate 360 degrees per year relative to the sun. This can obtained by the J2 effect of earth, also referred to as the flattening of the earth. Earth's gravitational field is not perfectly uniform due to the this flattening. By using this imperfection an orbit can be turned into a SSO by carefully selecting the altitude and inclination. In equation form the angular precession rate is written as [52]:

$$\dot{\Omega} = \frac{2\pi}{T_{ES}} \tag{4.13}$$

Here $\dot{\Omega}$ is the angular precession rate and T_{ES} is the orbital period of earth around the sun. Given that $\dot{\Omega}$ is described by the following equation:

$$\dot{\Omega} = -3\pi J_2 (\frac{R_e}{p})^2 cos(i) \frac{1}{T_o} \tag{4.14}$$

and that T_o is equal to:

$$T_o = 2\pi \sqrt{\frac{a^3}{\mu}} \tag{4.15}$$

One can solve the equation for inclination i knowing the time it takes for earth to complete one rotation around the sun:

$$cos(i) = -\frac{2\dot{\Omega}}{3J_2 R_e^2 \sqrt{\mu}} a^{\frac{7}{2}} \tag{4.16}$$

here J_2 is the coefficient for the second zonal term related to the oblateness of the Earth, R_e the radius of earth, μ the standard gravitational parameter of the planet (398600.440 km3/s2 for Earth) and a the semi major axis of the orbit. From this equation one can see that the inclination of a SSO depends solely on the altitude of the orbit. Given an altitude of 500 km this results in an inclination of $97.403°$.

It is important to note that maintaining a Sun-synchronous orbit (SSO) throughout the spacecraft's lifetime is highly unlikely. The orbit begins at an altitude of 550 km but gradually decays to around 500 km due to atmospheric drag. This decay affects the orbital inclination required for an SSO, which must remain precise to ensure the orbit precesses at the correct rate relative to the Sun.

While correction burns could theoretically maintain the necessary inclination, this is impractical for a CubeSat due to its limited size and mass, which restrict propulsion capabilities.

As a result, the longitude of the ascending node (Ω) was set to zero at the start of the mission. This value is expected to drift over time due to the lack of active orbit maintenance. Nevertheless, the

insights gained from this mission remain applicable to other values of Ω, and can inform future designs or missions with similar constraints.

The sun season was chosen to be summer solstice and the albedo constant a to be 0.3 everywhere on earth. Lastly the orientation of the spacecraft is as follows: the patches will always point towards earth (nadir) and the x-axis will always point in the flight direction.

A summary of all the orbital parameters as used in the simulation are presented in Table 4.1.

Table 4.1: Orbital parameters for the spacecraft used in the simulations.

Orbital parameter	Value
i [°]	97.403
e [-]	0
a [km]	R_e + 500
Ω [rad]	0
ω_o [rad]	0
υ_0 [rad]	0

In order to simulate the thermal behavior a model has been set up with the use of COMSOL Multiphysics [53]. It was decided to perform a simulation instead of a analytical analysis since the problem was deemed to complex. This is mainly due to the patches and the radiative links in the system. To reduce the model size and run time, only one panel of 5x5 patches is simulated in the above mentioned orbit. The frame mentioned before has a thickness at the edges of $0.1\,\mathrm{mm}$ and a height of $3.71\,\mathrm{mm}$ as is the distance between the layers in the prototype. The patches are all assumed to be square with a side length of $35\,\mathrm{mm}$ and the square hole inside being always 30% of the outer length, in this case thus being $10.5\,\mathrm{mm}$, and the spacing between the patches is $45\,\mathrm{mm}$. This is done for simplicity of the model, since not the exact dimensions of each patch is known at the moment. The thickness of the membranes is also the same as in the prototype: $50\,\mu\mathrm{m}$ thick for the polyimide layer and $17\,\mu\mathrm{m}$ thick for the copper layer. In Figure 4.1a the base geometry can be observed with the 5x5 patches. The membranes are modeled as 2D shell elements and the frame as a 3D solid element. The mesh of the geometry can be observed in Figure 4.1b. The sequence to obtain this mesh is as follows: Extra Fine Free Quad mesh on the holes inside the patches. Extra Fine Free Quad mesh on the patches. Courser mesh size on entire geometry, with Free Tetrahedral on the frame and Free Quad on the remaining.

Initial temperatures used in the panel are the following. The patches and top sheet all have an initial temperature of $-40\,^{\circ}\mathrm{C}$. While the frame and bottom membrane have initial temperatures of $-120\,^{\circ}\mathrm{C}$. The study used to simulate the temperatures during orbit is the ”Orbital Thermal Loads” module with a total of 100 time steps for 2 orbits.

Lastly, the different values of absorptivity and emissivity need to be specified. It is assumed that no coatings are applied to the panel on the inside and outside. A summary of the used absorptivity and emissivity for the each surface can be found in Table 4.2. The exact type of copper used on the RA is unknown, hence the values in the table are used.

Table 4.2: Absorptivity and emissivity values for all surfaces in the reference model.

Surface	Absorptivity (α)	Emissivity (ϵ)
Patches out	0.25	0.5
Patches in	0.1	0.57
Top sheet out	0.1	0.57
Top sheet in	0.1	0.57
Frame in and out	0.1	0.065
Ground plane in	0.25	0.5
Ground plane out	0.1	0.57

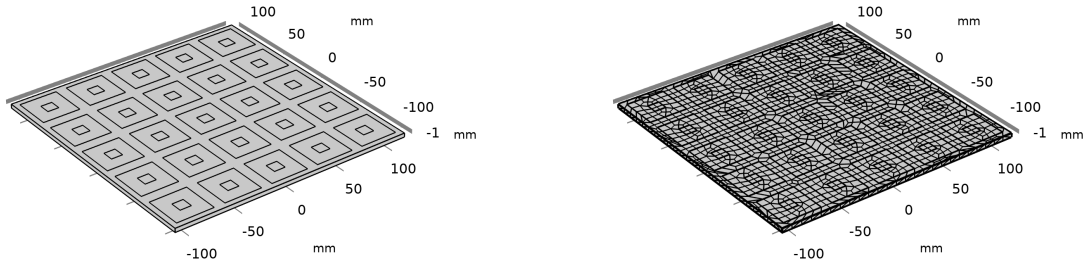

(a) (b)

Figure 4.1: (a) 3D representation of the panel geometry comprising 5×5 patches. (b) Meshed model of the same panel configuration. Both subfigures were generated using COMSOL Multiphysics.

The relevant material properties for all of the materials used in the panel are summarized in Table 4.3. The type of aluminum used for the frame is Aluminum 6063-T83. For the layers in the membranes the base material copper and polyimide were used which are already implemented within COMSOL. If applicable the Margin of Safety (MoS) can be calculated with the following formula:

$$MoS = \frac{Failure\ stress}{Applied\ stress} - 1 \tag{4.17}$$

Table 4.3: Important material constants used in the simulations, including copper (Cu), aluminum (Al), and polyimide (PI).

Material parameter	CU	AL	PI
E [GPa]	110	69	3.1
ν [-]	0.35	0.33	0.345
k [W/(m K)]	400	201	0.15
α [1/K]	1.70E-05	2.34E-05	4.50E-05
ρ [kg/m^3]	8960	2700	1300
σ_y [MPa]	68 [54]	241 [55]	103 [56]

4.2 Orbital Parametric Thermal Loads

In order to understand the influence of certain parameters the decision was made to perform parametric studies. Here only one value at a time is changed and the results are compared against each other. The following parameters will be changed and their influence studied:

- Absorptivity
- Emissivity
- Material change
- Thickness
- Panel orientation
- Array of panels
- Size of panels

Absorptivity

The temperature behavior of the spacecraft can be influenced in two primary ways: by modifying the radiative links or the conductive links between components. Absorptivity accounts for a part of the radia-

tive links. By having a higher absorptivity more heat is going into the system, heating up the spacecraft. In order to get a good understanding of how much this is, a parametric study will be performed. For α a range of 0.1, 0.25, 0.5, 0.95 was deemed reasonable, since this includes the already used values in the reference case and covers the entire possible range of potential values. A change in absorptivity can be obtained by applying different coatings layers with different values for the radiative links. However this increases the weight and might create an additional electrically conductive link.

Emissivity

Besides absorptivity also emissivity is an important factor in the radiative links. Having a high emissivity generally means more heat is ejected form the system, but also less earth IR is being absorbed. For ϵ a range of 0.065, 0.25, 0.55, 0.95 was deemed reasonable, since this includes the already used values in the reference case and covers the entire possible range of potential values. A change in emissivity can also be obtained by applying different coating layers. Unfortunately both the emissivity as the absorptivity are changed by changing the coating and cannot be independently tuned.

Material Change and Thickness

With the radiative links covered by the absorptivity and emissivity now the conductive links still have to be changed. This can be done by chancing the material conductivity or the geometric properties (i.e. the thickness). From the requirement Ar-002 the copper is not allowed to be a different material, but the other materials do not have this requirement. In order to get a good range of different conductivity the following 5 materials have been selected: Polyimide (0.15 W/(m K)), Glass fiber (1.3 W/(m K)), Titanium (21 W/(m K)), Aluminum (201 W/(m K)) and Copper (400 W/(m K)). These materials are only used for their theoretical influence of changing the conductivity.

Besides the material conductivity also the geometry can be changed. In this case the thickness of the entirety of the frame and the thickness of the polyimide layers. The frame thickness ranges from $0.1\,\mathrm{mm}$, $0.5\,\mathrm{mm}$ and $1\,\mathrm{mm}$. The polyimide layers vary between $50\,\mu\mathrm{m}$, $75\,\mu\mathrm{m}$ and $100\,\mu\mathrm{m}$.

Array Orbit Orientation

From requirement Sys-009 a range of allowable angles is given for the main beam hitting earths surface, this corresponds to γ in Figure 4.2a. This means that the RA can be under an allowable ranges of angles β in space as well, which means that it is not parallel to earths surface. To calculate the allowable range of β, the impact angle and altitude need to be known. In order to solve for the angle β a triangle can be set up as shown in Figure 4.2b. Using the sin rule to determine the angle γ gives the following equation:

$$\gamma = sin^{-1}\left(\frac{R_e + altitude}{R_e} sin(30 + \beta)\right) \tag{4.18}$$

Then varying the angle β and knowing the allowable range that is acceptable for γ $(20 - 40°)$ it can be found that β is allowed to range from $-11.5°$ to $6.2°$ at an altitude of 550 km. To limit the amount of simulations only four values from this range have been chosen to perform parametric simulations on. With steps of $5.9°$ this results in $-11.5°$, $-5.6°$, $0.3°$ and $6.2°$.

Array of panels and Panel size

As stated before only one panel is simulated every single simulation with 5x5 patches on each panel. In reality, more than one pane will be present in the final RA. To capture the thermal behavior for multiple connected panels a simulation was done. Initially, a simulation was performed using a configuration of 3×3 patches on each of 3×3 panels. Based on the results from this setup, an estimation was made for a larger configuration consisting of 5×5 patches per panel within the same 3×3 panel array. A thermal connection between panels is obtained by adding conductive connections with the use of cylinders with a radius of $1\,\mathrm{mm}$ and a length of $2.8\,\mathrm{mm}$ made of the same type of aluminum as the frame. This has been added to try and capture the flow of heat through any hinges connecting the panels to each other.

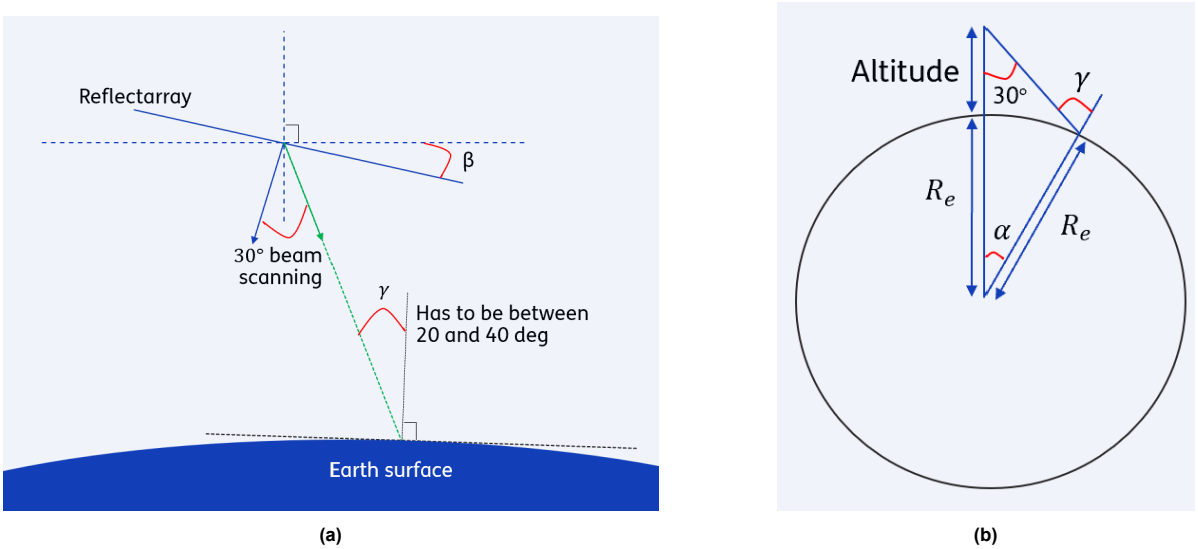

(a) (b)

Figure 4.2: (a) Reflectarray orientation in orbit, with beam illumination angle γ ranging from 20° to 40°. (b) Spatial relationship between the reflectarray and Earth, highlighting the geometric triangle employed to compute angle β.

The sizes have been determined based on torsional springs, with the smallest main loop diameter. This will be further explained later in this chapter.

Lastly the impact on the temperatures could also change due to different panel sizes. This is relevant to the deployment design since it might be preferable to have a different amount of patches per panel. Based on this analysis some thermal induced conclusion can be made on the size of a panel.

4.3 Thermo-elastics

Observed temperature changes in orbit demand an analysis of thermally induced panel deformations. These deformation have to be compared with the allowed deformations from the given requirements. First the model is explained in more detail and afterwards a more detailed explanation on how the deformation is checked with the given requirements is presented.

Since it is unknown what the limiting temperatures are going to be during the orbit, a global temperature increase for all parts on the panel have been selected. It was experienced that with COMSOL it is hard to obtain a converged solution for significant temperature increases. Hence only an increase of $5\,^{\circ}\mathrm{C}$ was chosen, since COMSOL could obtain a converged solution for this value. At higher temperatures the solution was seen diverging, not giving a solution. There is no clear explanation for this, but it is suspected to be caused by the very thin membranes and perhaps the element type. Ideally the element type ”membrane” would be used, since the actual membranes are so thin it is expected to not carry any bending stresses and thus also compressive stresses. In order to perform the temperature deformation analysis in COMSOL it was however required to have the elements carry compressive stresses. For this reason shell elements have been selected as elements for the membranes.

It is expected that due to the temperature increase and the use of two different materials in the membranes, out of plane deformation will occur. To get a better understanding of the results it is vital to know the equation describing linear thermal expansion and contraction. It is given to be [57]:

$$\Delta L = \alpha L_0 \Delta T \tag{4.19}$$

Here α is the coefficient of thermal expansion, L_0 the original length and ΔT the change in temperature. Hence with an increase of the temperature, an increase in length is present and due to this a larger out of plane deformation is expected for the membranes. Once the deformation and stresses are known

for the membranes, some positional based antenna requirements have to be checked, specifically: AR-004, AR-005, AR-006 and AR-007.

- **Ar-004** This requirement states that the surface accuracy has to be between $\pm 0.5\,\mathrm{mm}$. In order to find the surface accuracy a reference line has to be determined. Based on the distance between the reference line and the actual deformation the surface accuracy can be calculated. To do this, the surface is cut through the middle along the y-axis to find the deformed membrane geometry. The reference is then determined by computing a second degree polynomial trend line. Lastly, the difference is computed between the reference line and the actual deformation.
- **Ar-005** This requirement states that the tolerance between of the distance two membranes have to be within 1/200 of the free space wavelength of each other. With the known frequency this translates to a allowable tolerance of $0.36\,\mathrm{mm}$. Calculating the tolerance difference is straight forward with the given cut through the middle as used in Ar-004.
- **Ar-006** This requirement states that the maximal out of plane displacement of the panel cannot be more than 1/16 of the free space wavelength. Converting this to the simulation where a panel has the size of $225\,\mathrm{mm}$, one has to perform the following conversion. Starting with Figure 4.3, one can set up the following sequence of equations to determine the allowable deformation for one panel, in the figure corresponding to h_1.

$$\begin{aligned} h_1 &= l\sin(\alpha_1) \\ h_2 &= l\sin(\alpha_2) = \sin(2\alpha_1) \\ h_{tot} &= h_1 + h_2 + h_3 + ... = \frac{\lambda}{16} \\ l\left(\sin(\alpha_1) + \sin(2\alpha_1) + \sin(3\alpha_1)\right) &= \frac{\lambda}{16} \\ l\sum_{n=1}^{N}\sin(n\alpha_1) &= \frac{\lambda}{16} \end{aligned} \tag{4.20}$$

  Numerically solving the last equation for α_1 with N equal to 5 and l equal to $225\,\mathrm{mm}$ gives a maximum allowable deformation of one panel out of plane to be $0.35\,\mathrm{mm}$

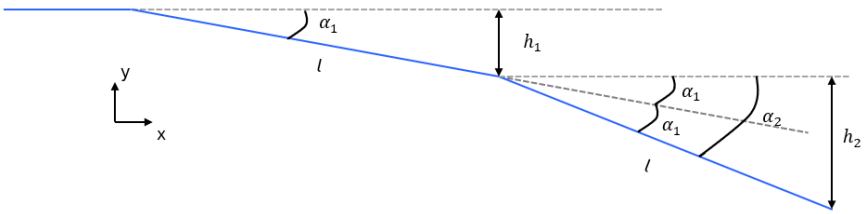

Figure 4.3: Visualization of the analysis used to determine the maximum allowable displacement of panels.

- **Ar-007** Lastly, the stress must be evaluated to ensure that no plastic deformation occurs in the panel. This can be easily assessed by visually inspecting the von Mises stress results provided by COMSOL at the end of the simulation.

In order to get to the deformed shape two studies in COMSOL have to be done. First a buckling analysis has to be performed to get the first buckling shape. Once this is found, the first five buckling mode shape can be used as input for an initial out of plane displacement. After this the temperature is incrementally increased to the final desired temperature of $5\,^{\circ}\mathrm{C}$. For this, a step size has been used of $0.1\,^{\circ}\mathrm{C}$ till the first $1\,^{\circ}\mathrm{C}$ increase and for the remaining steps a step size of $0.5\,^{\circ}\mathrm{C}$ has been used. The reference temperature is was set to $20\,^{\circ}\mathrm{C}$ as this is a very likely temperature in which the RA will be manufactured.

The model is the same as used in the orbital analysis for an array of panels. Only one panel is used with the same size cylinders. The edges of the cylinders are clamped as boundary conditions with this simulation. A other change is the increase of the frame thickness to $1\,\mathrm{mm}$. The meshing sequence was set to the default in build meshing sequence in COMSOL with ”fine” as size.

4.4 Deployment

To perform an analysis of the deployment, first the deployment has to be defined in more detail. Sauder et al. [49] suggested to use springs as activation mechanism for the panels. This would mean that the panels need to be kept in place and, once they are in orbit, need to move into their respective place with the use of springs. In this case it would be beneficial to use torsional springs. Torsional springs are mechanical devices that store and release energy by twisting. It consists of a helical coil of material that applies a torque in the opposite direction of the force it is applied to. However, no selection has been made on the deployment sequence yet. This directly impacts the amount of connections between the panels and the deployment reliability.

In order to get a higher deployment reliability the entire array is proposed to be deployed sequentially. In this way, if a spring fails, only a part of the panels is not deployed instead of the entire array. This would be the case if an Miura-ori kind of system is used. This is a one degree of freedom system, meaning the entire system can be deployed by only controlling one parameter. With a sequential type of deployment, if a hinge fails, only a part of the RA will not be deployed. The RA can then be designed such that amount of active patches is high enough to get a good far field radiation pattern. In order to make the deployment sequential, a proposal is made for the deployment, as can be seen in Figure 4.4, which shows an example of a deployment of 5x5 panels. To reduce inter-connectivity and the amount of hinges, the RA panels are split into two main sections. The center panels are called the spine and the side panels are called the strips or ribs. The strips are connected to the spine and the spine connects the strips to the satellite. Each strip will deploy sequentially in order to not interfere with other strips of RA panels and to have more control of the deployment. Hence the amount of steps to deploy this type of RA is equal to N+1 steps NxN panels.

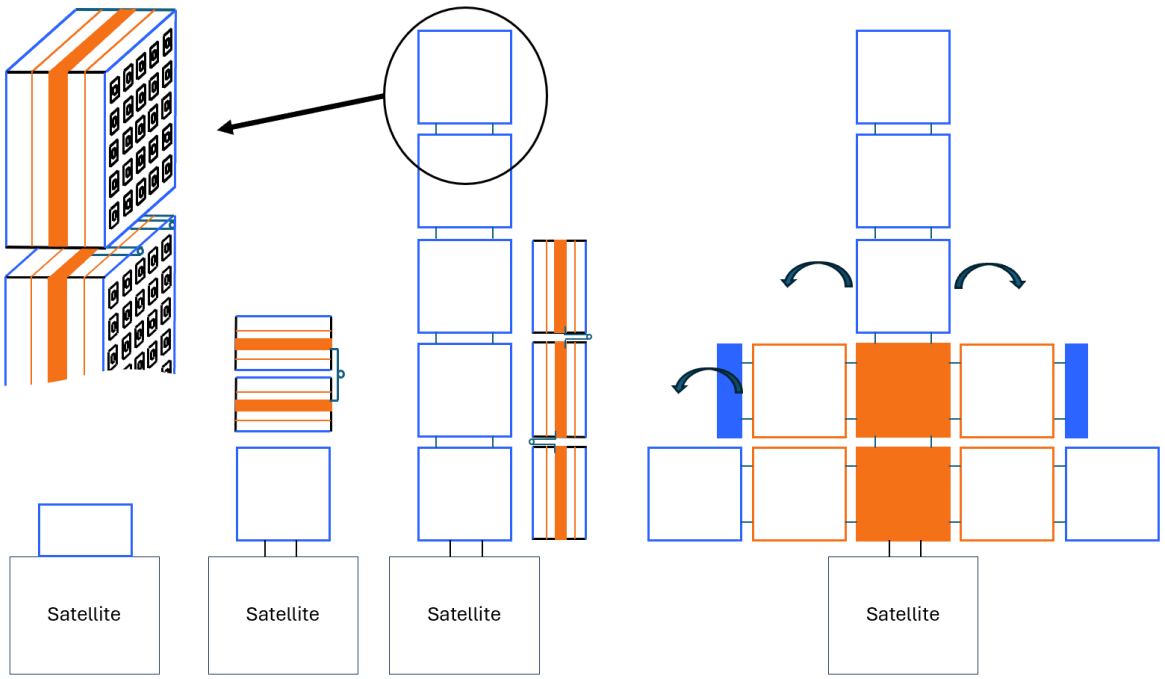

Figure 4.4: Step-by-step visualization of the deployment sequence for a 5×5 reflectarray, with each panel comprising 5×5 patches.

To make deployment more structured all panels for a strip will be deployed from a panel box. Each panel box is connected to another box or the satellite. To make the spine deployable, and without interfering with the deployment of the strips, a special connection is needed between the boxes. Instead of having a connection at the edges of the box a connection is needed at the middle panel for each panel box with the use of a hinge. The length of the hinge varies with the size of each box and thus with the total amount of panels in the array. Meaning this part cannot be universal for each choice of amount of panels. The connections between the panels in a strip are, however, universal and can be the same everywhere

in the RA. This makes it important to get a good understanding of the deployment dynamics for the panels in the strip. To ensure effective deployment of the panels, it is crucial to understand the role of torsional springs in the system and their working. By analyzing the characteristics and the physics of torsional springs, a better understanding can be acquired on the deployment of the panels.

The torque of a torsional spring can be described with the following equation:

$$T_q = \theta k \tag{4.21}$$

Here θ is the angle over which the spring is rotated and k is the spring constant of the torsional spring. The spring constant k is a function of the geometric properties of the spring but also of the material used:

$$k = \frac{d^4 E}{64 D_m N_a} \tag{4.22}$$

Here d is the wire diameter, E the longitudinal elastic modulus of the spring material, D_m the main loop diameter and N_a the amount of loops. One can change these parameters to get a weaker or stronger spring, but within limitations of course.

The deployment of a panel consist of roughly three steps or phases: (1) The start or activation of the torsional spring, (2) the movement of the panel from start to end position, and (3) the response of the panel as it arrives at the end position. It was decided to only analyse the start and end response, since these were deemed the most critical steps during deployment. At the start position the torque applied by the torsional spring on the panel is highest and at the end response the most amount of energy is in the system. In order to analyse the end response it is important to know the expected angular impact velocity. This can be estimated by setting the angular kinetic energy equal to the energy stored in the torsional spring.

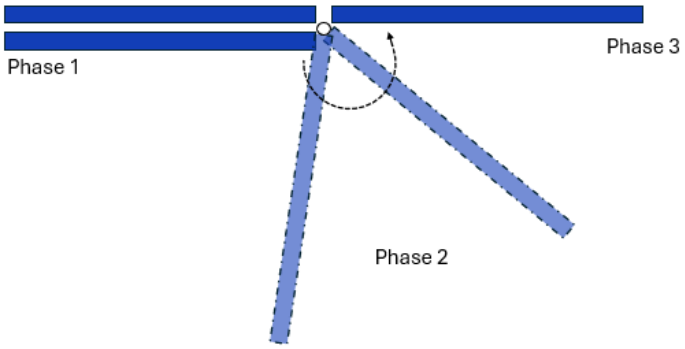

Figure 4.5: Sequential phases of panel rotation leading to its final deployed position.

Stating the angular kinetic energy equation [58]:

$$E_{rot} = \frac{1}{2} I \omega^2 \tag{4.23}$$

Finding the energy stored in a torsional spring:

$$U = \int_{\theta_0}^{\theta_1} T(\theta) d\theta \tag{4.24}$$

by substituting Equation 4.21 for $T(\theta)$ one can obtain:

$$U = \int_{\theta_0}^{\theta_1} k\theta d\theta \tag{4.25}$$

solving this integral gives:

$$U = \frac{1}{2}k(\theta_1^2 - \theta_0^2) \tag{4.26}$$

And assuming all the stored energy in the spring is converted to angular kinetic energy without losses gives:

$$\frac{1}{2}k(\theta_1^2 - \theta_0^2) = \frac{1}{2}I\omega^2 \tag{4.27}$$

Solving for ω gives the equation for impact velocity after a rotation from θ_0 to θ_1:

$$\omega = \sqrt{\frac{k(\theta_1^2 - \theta_0^2)}{I}} \tag{4.28}$$

It is desirable to have a low impact velocity to reduce the deformations and stresses in the panel and prevent failure. According to the derived equation, there are three ways to lower the impact velocity: lower the angle of rotation, lower the spring constant of the torsional spring or increase the moment of inertia. However, lowering the angle of rotation is not possible due to the fixed angle that the panels have to rotate. This leaves lowering of the spring constant or increasing the moment of inertia as potential options. Lowering k can be done in multiple ways: lowering the wire diameter, using a material with lower longitudinal elastic modulus, increasing the main loop diameter or increasing the amount of loops. Increasing the moment of inertia can be done in two ways, by deploying more panels with one spring, or by increasing the amount of material in a single panel, by making the frame thicker for example.

Using a build-in feature of COMSOL one can determine the moment of inertia of the model. This leaves only the spring constant k to be determined. To get a reasonable value of k, the spring constant is calculated for a spring of the shelf, from Lee Springs [59]. Picking the smallest spring, i.e. with the smallest main loop diameter, gives k equal to $9.56480 \cdot 10^{-4}$ with spring name: LTR012A 03 S and has the following parameters presented in Table 4.4.

Table 4.4: Parameters of the LTR012A 03 S torsional spring from Lee Springs [59]

Parameter	Value
Wire diameter	$0.3\,\mathrm{mm}$
Main loop diameter	$2.63\,\mathrm{mm}$
Loop amount	9.75
Material	Stainless Steel 302/304
E	$193\,\mathrm{GPa}$
k	$9.56480 \cdot 10^{-4}$

Initial results indicated a too large deformation of the membrane of the panel, hence changes to the design were made. First, the moment of inertia was increased by making the frame thicker from $0.1\,\mathrm{mm}$, as was used during the orbital studies, to $2\,\mathrm{mm}$ thickness. However, still the impact speed was to high, hence a spring alteration was considered. With the thinnest spring wire used from Lee Springs, the only other options are chancing the material, increase loop diameter or amount of loops. However these all are bad options. Since a drastic lowering of impact speed is needed a much weaker material would be needed. Increasing the amount of loops would increase the size of the spring significantly. Leaving the option for a bigger loop diameter. This has however two disadvantages. Looking at the placement of the spring compared to the panels reveals why, see Figure 4.6.

In the standard configuration, a gap is present between the panels both in the stowed and deployed states. This gap is equal to the diameter of the spring's main spool. By moving the spring around and not placing the spring inside a panel one can eliminate only one of the two occurring gaps. Always a gap remains between the storage part or the deployed part. By increasing the main loop diameter this gap becomes larger which is undesirable. By having the gap during storage means an almost double amount of storage volume is required. Hence a gap between the panels after deployment would be better from a satellite volume point of view. It is however unknown what the effect of this would be on

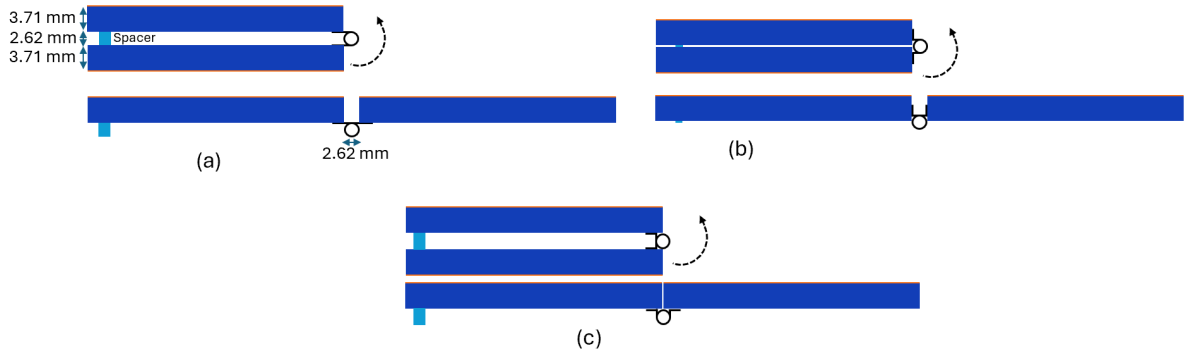

Figure 4.6: Comparison of spring placement configurations: (a) standard placement, (b) configuration optimized for minimal storage volume, and (c) configuration optimized to reduce inter-panel gap spacing.

the antenna performance. It would perhaps be possible to put the spring main loops inside the panels, but this would not be straight forward. This means that the there is no need anymore to minimize the main loop diameter. There is now however a maximum allowable loop diameter, driven by the panel thickness. Since the spring can be stored between two panels, the maximal spring diameter would be twice the panel thickness, resulting in $7.42\,\mathrm{mm}$. However, this still gives an angular impact velocity that is too high as the moment of inertia is still as low as $2.23 \cdot 10^{-4}\ \mathrm{kg\,m^{-2}}$.

Concluding, it is not possible to drastically lower membrane deformation by increasing the moment of inertia or increasing the spring constant. Hence some kind of additional support is needed to prevent the membrane from displacing to much. This has two advantages, first the mass increases meaning a higher moment of inertia is obtained and thus a lower impact speed, but also less displacement will be observed since the membrane will be prevented from displacing at some points. There are infinite ways to apply additional support to the system, but only one option was explored. The additional support is placed in a plus (+) shape with similar thickness as the outer frame. This analysis is purely done for structural purposes, since the effect of placing additional support directly underneath the patch on the antenna performance is unknown.

Two structures will be simulated in COMSOL: one panel without additional support, featuring a frame thickness of $2\,\mathrm{mm}$, and another panel with a plus-shaped internal support, resulting in a local thickness of $4\,\mathrm{mm}$ while maintaining the same edge frame thickness. The additional support is also made of AL as is the rest of the frame. The membranes are exactly the same as TE study, with again shell elements used.

Both structures will be used for two simulations. First to simulate phase 1 of deployment (the activation of the spring) and secondly to simulate phase 3 (the dynamic response at the end of deployment). To simulate phase 1 a surface load is applied with a total force equal to $0.285\,99\,\mathrm{N}$. This force has been calculated with the following equation:

$$F_{applied} = \frac{k \cdot \theta}{R_{spring}} \tag{4.29}$$

Here k is the spring constant, θ the angle the spring has been twisted and R_{spring} is the length on which the spring force is acting. In this case k is equal to $3.37 \cdot 10^{-4}\ \mathrm{N\,m\,rad^{-1}}$, θ equal to $180°$ and R_{spring} equal to $3.71\,\mathrm{mm}$. A figure of the position of the applied force can be seen in Figure 4.7.

Both structures will be subjected to an angular impact velocity of $-50\,°/\mathrm{sec}$, chosen as an initial test value to facilitate interpretation of the results. Once the final impact velocity is determined, these simulations should be revisited and refined accordingly. It is expected that simulating at this angular velocity will still allow for meaningful conclusions applicable to a range of impact velocities. Additionally, the results may help identify a desirable target impact velocity for future testing.

The displacement of the top and bottom membrane in the middle of each part is extracted from the simulation. The mid point has been selected since this will experience the most displacement. For the

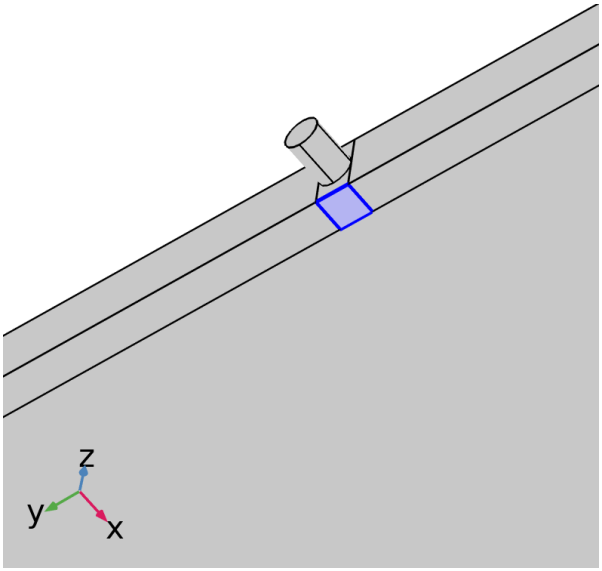

Figure 4.7: Position of applied load for phase 1 of deployment

additional support four parts are present, but due to symmetry only two parts are plotted. Besides the displacement of the membrane also the observed stresses are important. Hence the maximal observed Von Mises stress has been extracted and plotted for each time step, for different parts of the panel. This includes the frame and additional support, the bottom membrane for both layers and the top membrane for both layers.

In order to simulate the damping of the present material in space, artificial reighley damping is introduced. Since the deployment happens in space, with the only way of dissipating energy is by having it absorbed by the material, a damping factor of 0.3% was deemed substantially low. The corresponding α_r and β_r used by COMSOL can be calculated with the following two equations [60]:

$$\begin{aligned} \alpha_r &= \zeta \frac{2\omega_1\omega_2}{\omega_1 + \omega_2} \\ \beta_r &= \frac{2\zeta}{\omega_1 + \omega_2} \end{aligned} \tag{4.30}$$

Here ζ is the damping factor, ω_1 is the first frequency and ω_2 is the second frequency. The first frequency was chosen to be the first natural frequency of the system and the second frequency was chosen to be five times as high as the first natural frequency. This means that the dynamic analysis consists of two COMSOL studies: first an Eigenfrequency study was done to find the first natural frequency, and then the Time Depended study can be performed. The duration of the time depended study is set to $1\,\mathrm{sec}$ with a total amount of time steps of 200 steps.

The meshing sequence is the same used in the thermal aspects study. The changes to the geometry include the following: two small cylinders have been added to try and capture the behavior of the spring and hinges. These cylinders are made from the same material as the frame and have a radius of $1\,\mathrm{mm}$ and a length of $2.8\,\mathrm{mm}$. The length corresponds to the main spool diameter of one of the small springs of Lee springs [59]. They are positioned such that the distance between the edge and the cylinder is one fourth of the panel width. The free edges of the cylinders are clamped as the applied boundary condition during all simulations. An example of the additional support geometry, unmeshed and meshed can be observed in Figure 4.8.

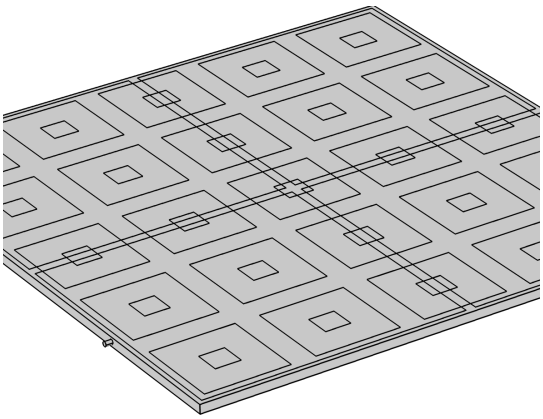

(a) 3D model of the geometry of the panel consisting of 5x5 patches, made in COMSOL.

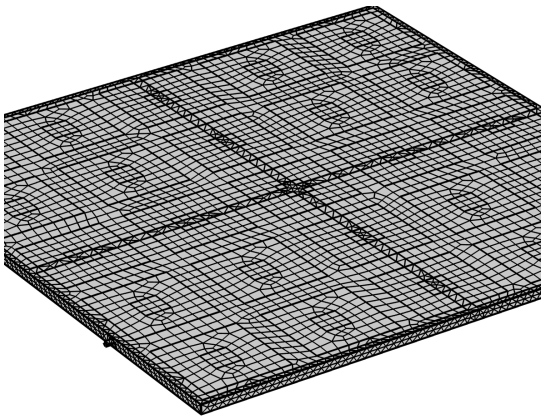

(b) 3D model of the meshed panel consisting of 5x5 patches.

Figure 4.8: (a) 3D model of the panel with additional support geometry, consisting of 5×5 patches, generated using COMSOL Multiphysics. (b) Meshed version of the same panel configuration, including the added support structure.

Chapter 5

Results

This chapter presents the results obtained from the simulations described in the methodology. In Section 5.1, the outcomes of the reference case are presented and discussed. Section 5.2 follows with the results of the parameter studies, including a discussion and summary. The mechanical analysis results are divided into two parts. Thermo-elastic deformation results are discussed in Section 5.3. Finally, Section 5.4 presents and discusses the results of the deployment study.

5.1 Orbital Thermal Loads

Before the results on the parametric studies can be analysed first, the reference case must be understood. After running the simulation the average temperature over time for the two orbits is calculated for the four main components in the structure: the frame, the patches, the remaining top membrane and the ground plane or bottom membrane. The results can be observed in Figure 5.1.

The temperature behavior of all components follows a consistent trend: when the bottom side heats up, the top side also experiences an increase in temperature, and vice versa. This is primarily due to the conductive link created by the frame, as well as the radiative interaction between the two membranes.

Additionally, the top part of the panel, including the patches and the rest of the top membrane, consistently have higher temperatures than the bottom side, which includes the frame and bottom membrane. The patches are warmer than the top sheet throughout the orbit, although their temperature remains below $0\,^{\circ}\mathrm{C}$ at all times.

Another thing to notice is that two orbits can be observed, the first orbit starting at 0 seconds and the second orbit at around 5700 seconds. Within one orbit two peaks are present. The first one indicates a higher temperature spike on the top side of the panel and the second peak a temperature spike on the bottom side of the panel. This pattern can be explained by the panel's illumination by the sun, as illustrated in Figure 5.2.

The sun rotates relative to the panel, as can be seen in the figures. First, the sun illuminates only the side of the frame and then moving such that it illuminates the top part of the panel. This explains the first and third peak. After the top the sun rotates to illuminate the bottom part of the array. This corresponds to the second and fourth peak.

Since the sun illuminates the bottom part of the panel this side of the panel heats up significantly by almost $30\,^{\circ}\mathrm{C}$ as can be seen in the second peak in the bottom part of the panel. Due to the thermal coupling between the top and bottom part of the panel not being perfect, the top part of the panel does not increase the same amount in temperature. This explains why the second peak on the bottom part of the panel is higher then the first peak. And vice versa on the top part of the panel with a higher first peak hen the second peak.

During the second peak the top part of the array is increasing even more in temperature due to albedo. Albedo can only happen when there is sunlight illuminating earth. During the first peak the spacecraft

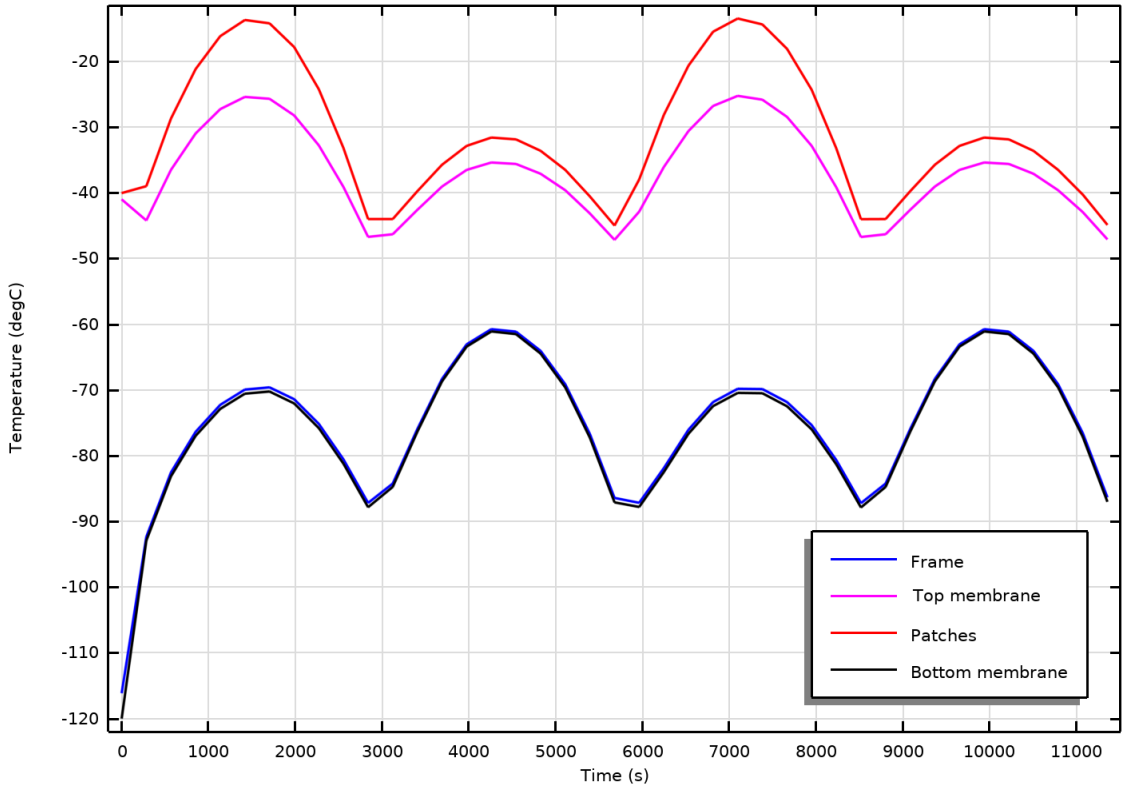

Figure 5.1: Simulated temperature profiles over time for the reference panel configuration, including the frame, patch array, top membrane (excluding patches), and bottom membrane.

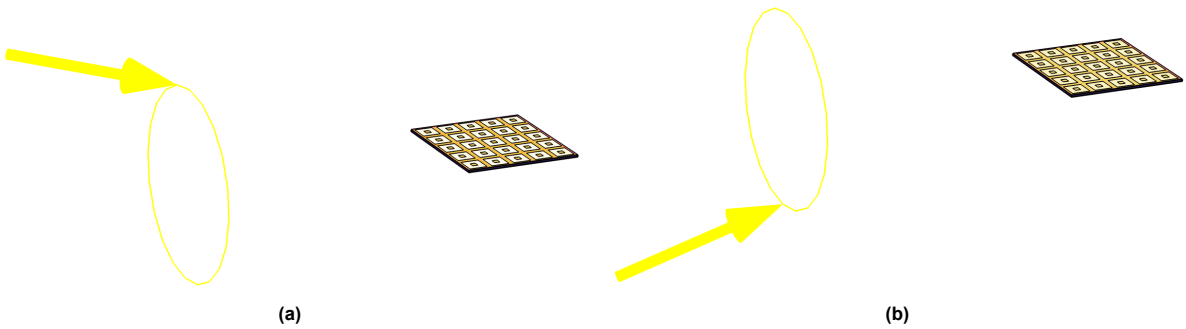

Figure 5.2: Suns position relative to the panel for two examples. (a) Top illumination. (b) Bottom illumination.

is traveling over a part of earth where no sunlight illuminates the earth, but not far enough to create an eclipse. This results in no albedo being present during the first half of the orbit. However, during the second half the spacecraft enters the sunlit part of earth, meaning that now albedo is present. This phenomena explains the temperature difference between the patches and the top sheet. The patches have a higher absorptivity compared to the top sheet, meaning that more heat is going into the patches than into the top sheet when the sun illuminates this part. Regardless of the part of the orbit considered the patches always have a higher temperature than the rest of the top membrane. This results in the patches having a higher temperature than the top sheet at all times.

When taking a closer look at each of the four main components a more detailed temperature distribution can be seen. First, the frame is considered, for which the results are shown in figure Figure 5.3a. The temperature distribution in the frame is almost constant. The corners are a little warmer than the middle parts, but this range is within $0.5\,^{\circ}\mathrm{C}$, because of the radiative link of the frame upon itself.

Considering the patches next, a slightly larger temperature range can be observed of near $1\,^{\circ}\mathrm{C}$, see Figure 5.3b. Here the middle patches are warmer than the outer ring of patches. This indicates using an average temperature instead of the temperature distribution is a good approximation.

When looking at the top sheet the temperature fluctuations can be explained of the patches. The top sheet has a uniform temperature of around $-20\,^{\circ}\mathrm{C}$, except at the edges connecting it to the frame, see Figure 5.3c. The top sheet works as a thermal conductive connection between the hot patches and the colder frame and bottom sheet. Since PI is not very conductive the heat does not transfer well between these parts. This results in a large gradient in the PI sheet itself. With this information known, inspecting the location of the patches explains the observed behavior. The patches at the edges have only one edge close to the cold boundary while the patches in the corners have two edges close to the cold boundary. This results in the corner patches being colder than the edge patches.

Lastly the temperature distribution of the bottom membrane is important to observe, see Figure 5.3d. Here the temperature distribution at the connection from the membrane to the frame follows the observed distribution of temperature of the frame. The corners are warmer than the edges. However the middle part of the sheet is colder than the edges. There is no heat input coming expect from the frame so the sheet tries to distribute it but radiates the heat out. This gives the observed temperature range in the bottom membrane as well as the observed distribution.

Plotting the temperature at one time step through the top membrane and patches visualizes the temperature distributions in the top membrane more clearly. This can be observed in Figure 5.4, where both the location relative to the panel, as the resulting temperature through the top membrane are plotted. The patches are indicated by the green line while the PI sheet is visualized in blue. First thing to notice is that the PI sheet has the same temperature as the CU patches, but in between the patches the temperature drops. The temperature drop inside a patch is smaller than the drop between patches, due to distance being shorter in between the warmer patches, compared to the distance between seperate patches. The last thing to notice is the temperature change at the beginning and end of the graph. This is the same spike observed in the visual representation of the top sheet. Within a very short length the temperature changes by almost $60\,^{\circ}\mathrm{C}$. This can be explained by the non thermal conductive properties of PI.

Multiple conclusions can be drawn from the performed orbital studies. First of all, it has been observed that the top membrane with the patches always has a higher temperature than the bottom membrane and the frame. Each orbit consist of three parts. First the sun illuminates the top side, then illuminates the side of the panel, and lastly illuminates the bottom side. Low temperature variations of around $2\,^{\circ}\mathrm{C}$ have been observed in each part of the structure. Except for the top membrane near the edges connecting it to the frame, here high temperature variations have been observed of more than $50\,^{\circ}\mathrm{C}$. It was also observed that at any point during the orbit, the panel was below $0\,^{\circ}\mathrm{C}$.

5.2 Orbital Parametric Thermal Loads

Now that the reference case is fully understood, it is possible to interpret the results of the parametric studies. First absorptivity is presented, then emissivity and the other relevant parameters.

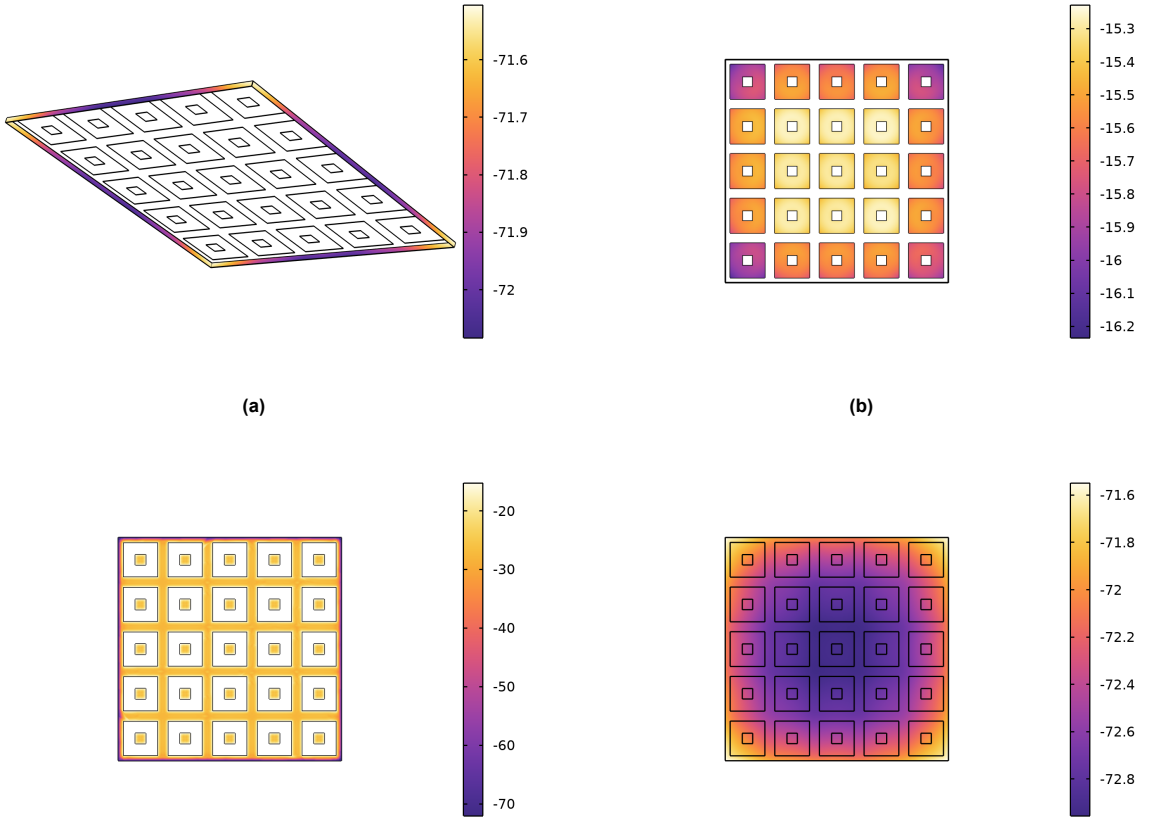

Figure 5.3: Temperature distributions of the four main panel components at 6812.4 seconds, with values expressed in $^{\circ}\mathrm{C}$: (a) frame, (b) patches, (c) top membrane, and (d) bottom membrane.

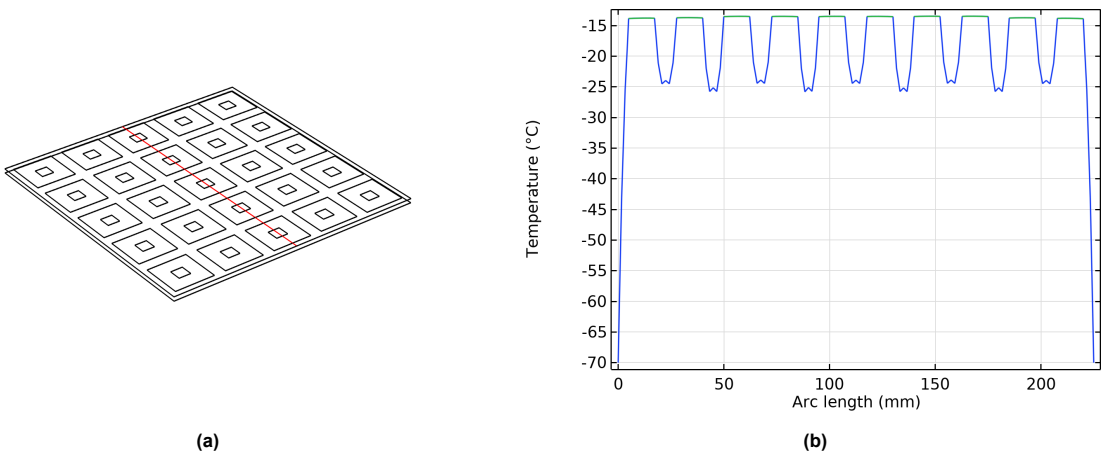

Figure 5.4: Temperature distribution through the top membrane at the final simulation time step. (a) Indication of the selected cross section on the panel. (b) Temperature profile along the arc length of the selected cross section, showing thermal behavior of the copper patches (green) and the polyimide layer (blue).

Absorptivity

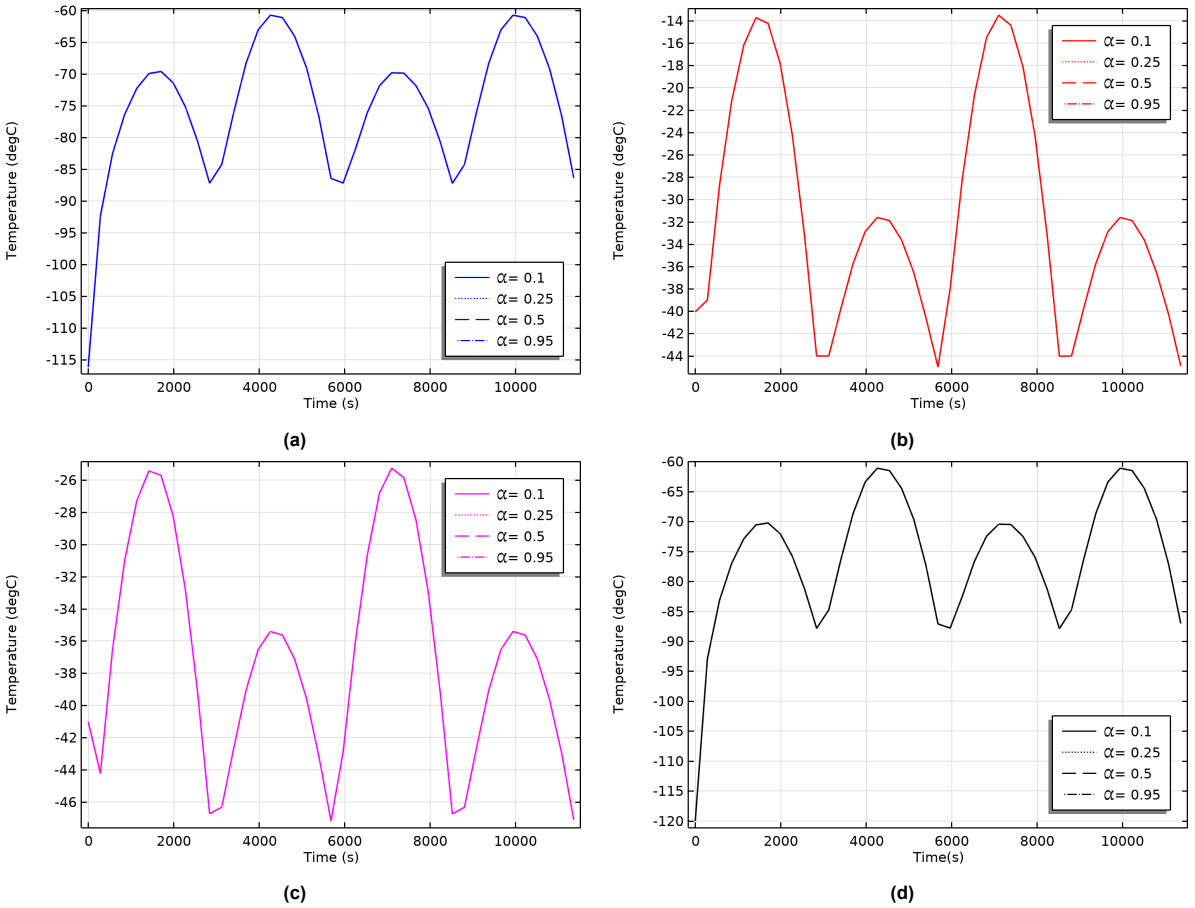

Figure 5.5: Simulated impact of altered frame absorptivity on average temperature distribution across panel components: (a) frame, (b) patches, (c) top membrane, and (d) bottom membrane.

First the frame is simulated for the different absorptivity values and the results are visualized in Figure 5.5. It can be quickly seen that there is no change in temperature for different values of α for any of the four main components. A possible explanation for this could be an error in the model, but after a closer inspection a deviation in the temperatures can be seen. Compared to the area of the membranes that the sun illuminates the frame contributes very little to the heat input for the system due to its relatively lower area. Hence changing the absorptivity of the frame has no influence on the behavior of the system on thermal aspects.

Changing the absorptivity of the patches gives the results as shown in Figure 5.6. Focusing first on the patches only, a temperature increase can be observed in the first and third peak. This is where the sun shines on the top side of the panel. However, during the lower peaks the temperature also increases, this is due to the previously explained albedo. However, the intensity of this reflected sunlight is lower than direct sun light, which explains why the temperature is lower in the second peak compared to the first peak. Due to the temperature increase in the patches also the other parts heat up across the panel. This is due to the thermal links between the patches all the way to the bottom membrane, through both conductive as radiative links. However, the temperature in the bottom part of the panel does not increase as much as the top part, due to the bottom membrane radiating heat into deep space.

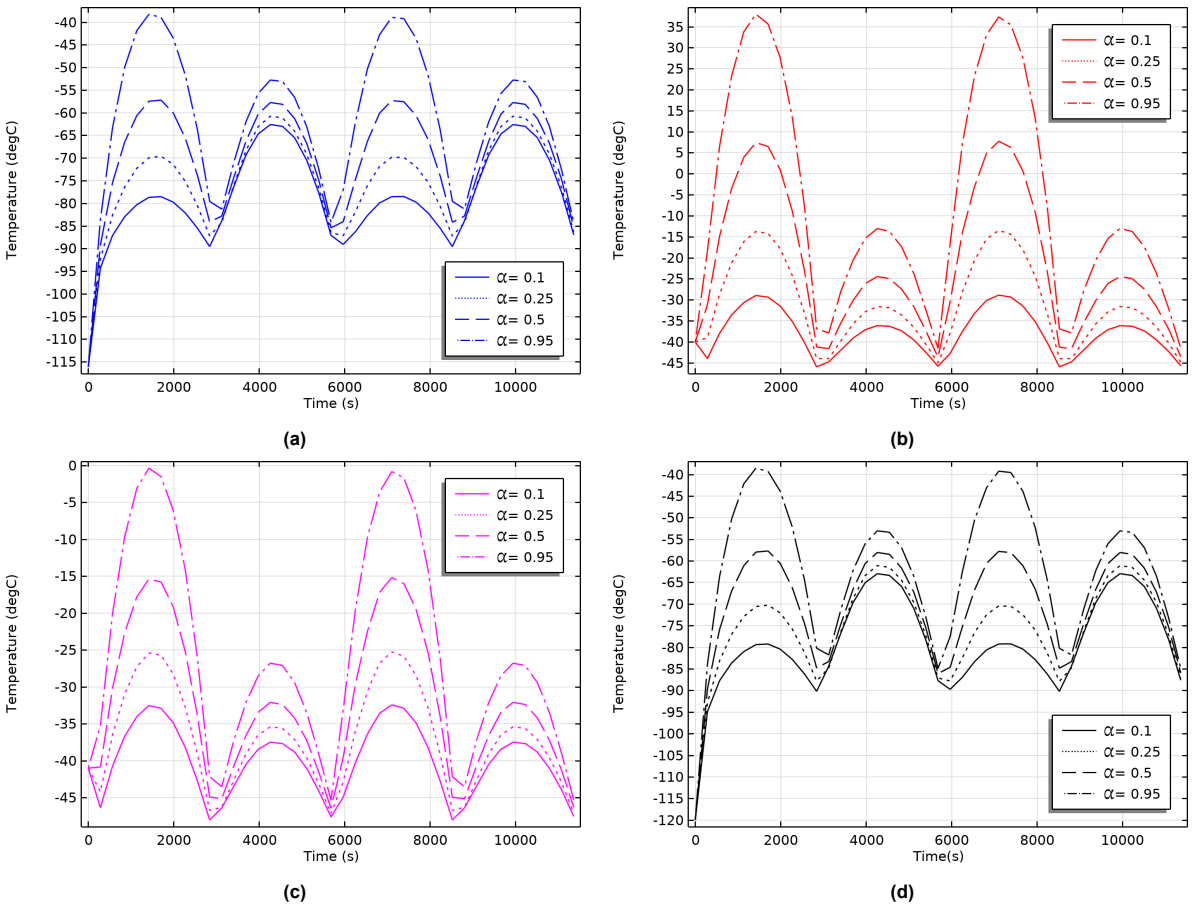

Figure 5.6: Simulated impact of altered patch absorptivity on average temperature distribution across panel components: (a) frame, (b) patches, (c) top membrane, and (d) bottom membrane.

Changing the absorptivity of the bottom membrane gives different results than the absorptivity change of the patches, as can be seen in Figure 5.7. In this case only the second and fourth peak show an increase in temperature, while there is no change in the other parts of the orbit. This is an expected result. Since the bottom side is only exposed to sunlight in the second part of the orbit only then a change in temperature should be present. The change in temperature is quite significant, with the largest increase in temperature of more than $100\,^{\circ}\mathrm{C}$ in the bottom membrane. Also in the top part of the panel a temperature increase is present of around $40\,^{\circ}\mathrm{C}$. It should be noted that only a part of the full orbit is influenced by this change of absorptivity, and the other part remains the same.

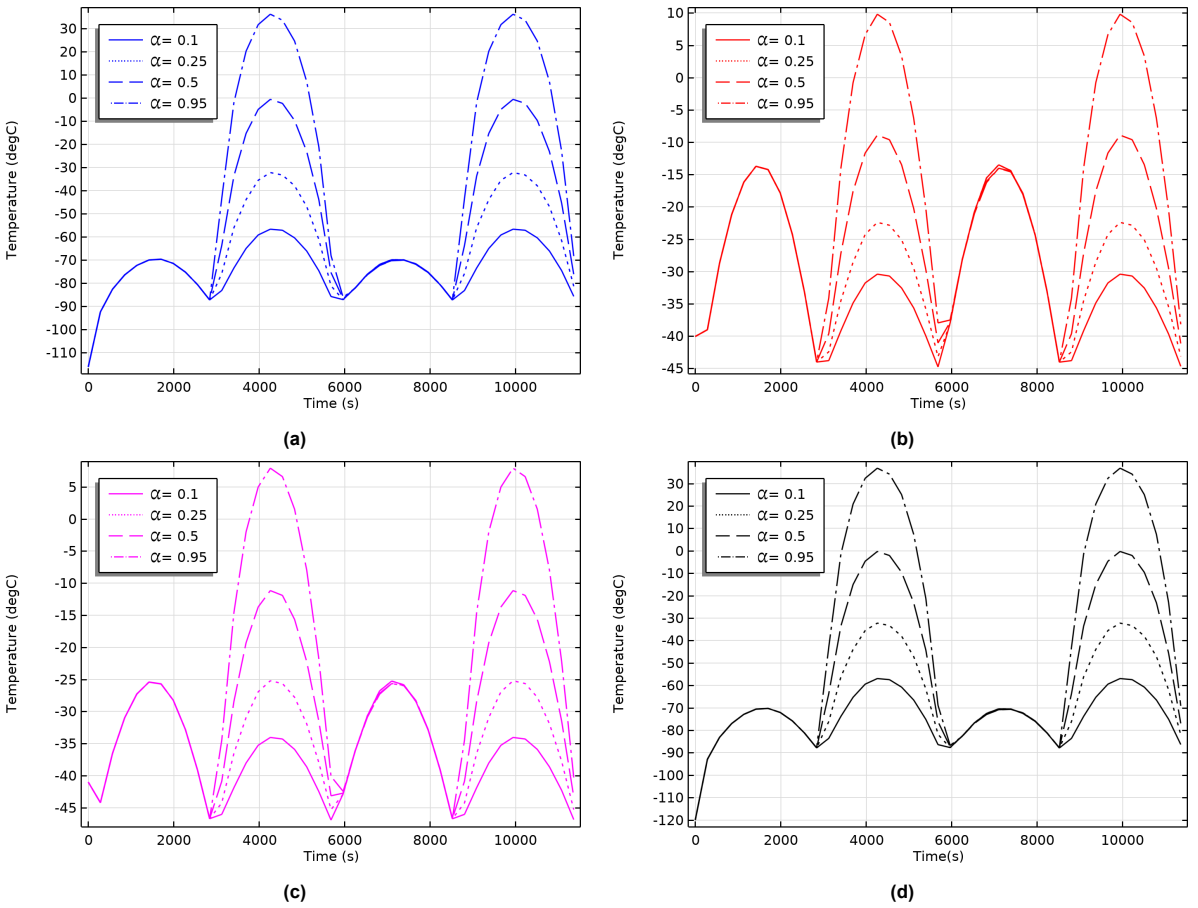

Figure 5.7: Simulated impact of altered bottom membrane absorptivity on average temperature distribution across panel components: (a) frame, (b) patches, (c) top membrane, and (d) bottom membrane.

Lastly changing the absorptivity of the top membrane, excluding the patches, gives the results observed in Figure 5.8. A similar graph can be observed for the change of absorptivity of the patches. However, now the temperature of the top membrane is higher than the patches. Due to the higher absorptivity more heat is going into this section of the panel. Due to the low thermal conductivity of the PI, this heat is not distributed equally over the top membrane and the patches, which results in the observed temperature difference. Due to the sun illuminating at some times only mainly the side of the panel and since this has little influence on the temperatures, as concluded from Figure 5.5, changing the absorptivity of the membranes does not change the temperatures during the entire orbit. It can be observed that the minimum temperatures do not change drastically.

A summary of the results of the parametric study on the absorptivity can be seen in Table 5.1. For the three different parts of the orbit (top, side and bottom illumination) the temperature change for each of the relevant parts of the panel is graded for all of the parameters. The impact label for each part of the orbit is determined based on the absolute temperature change ΔT in degrees Celsius:

$$\text{Impact Label} = \begin{cases} \text{No} & \text{if } \Delta T < 5 \\ \text{Low} & \text{if } 5 \leq \Delta T < 20 \\ \text{Medium} & \text{if } 20 \leq \Delta T < 50 \\ \text{High} & \text{if } \Delta T \geq 50 \end{cases} \tag{5.1}$$

With this table it would become clear that changing the absorptivity results in medium to high temperature changes, but in only one part of the orbit.

Increasing absorptivity on the top membrane increased the temperatures throughout the panel drastically, but only mainly in one first half of the orbit. Similar behavior has been seen with increasing the

absorptivity on the bottom membrane, but with the other half of the orbit increasing in temperature. It was also noted that no temperature variation was observed by chancing the absorptivity on the side of the panels.

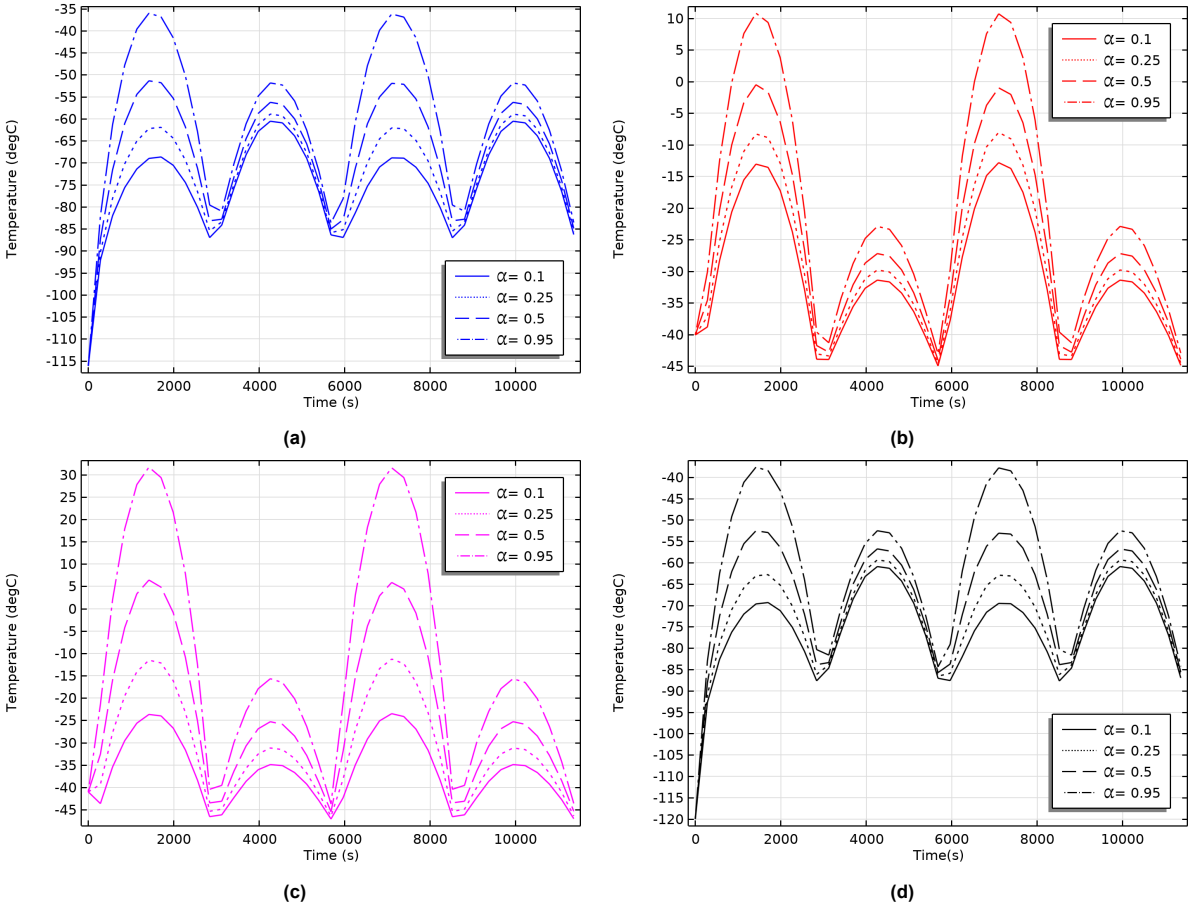

Figure 5.8: Simulated impact of altered top membrane absorptivity on average temperature distribution across panel components: (a) frame, (b) patches, (c) top membrane, and (d) bottom membrane.

Table 5.1: Temperature impact across three orbital phases based on surface absorptivity.

	Illumination on	Top	Side	Bottom
Patch out	Frame	Medium	Low	Low
	Patch	High	Low	Medium
	Top	Medium	Low	Low
	Bottom	Medium	Low	Low
Top out	Frame	Medium	Low	Low
	Patch	Medium	Low	Low
	Top	High	Low	Medium
	Bottom	Medium	Low	Low
Frame	Frame	No	No	No
	Patch	No	No	No
	Top	No	No	No
	Bottom	No	No	No
Bottom out	Frame	No	No	High
	Patch	No	No	Medium
	Top	No	No	Medium
	Bottom	No	No	High

Emissivity

One way to influence the minimum temperature is not to increase the amount of heat going into the system, but reducing the heat going out of the system, i.e. the emissivity. In the next part, the influence of changing the emissivity of all the surfaces will be analysed. In this case not only the outward facing side of a surface is of importance but also the inner facing surfaces. This is due to the heat exchange in the ambient band, and this happens inside the spacecraft as well.

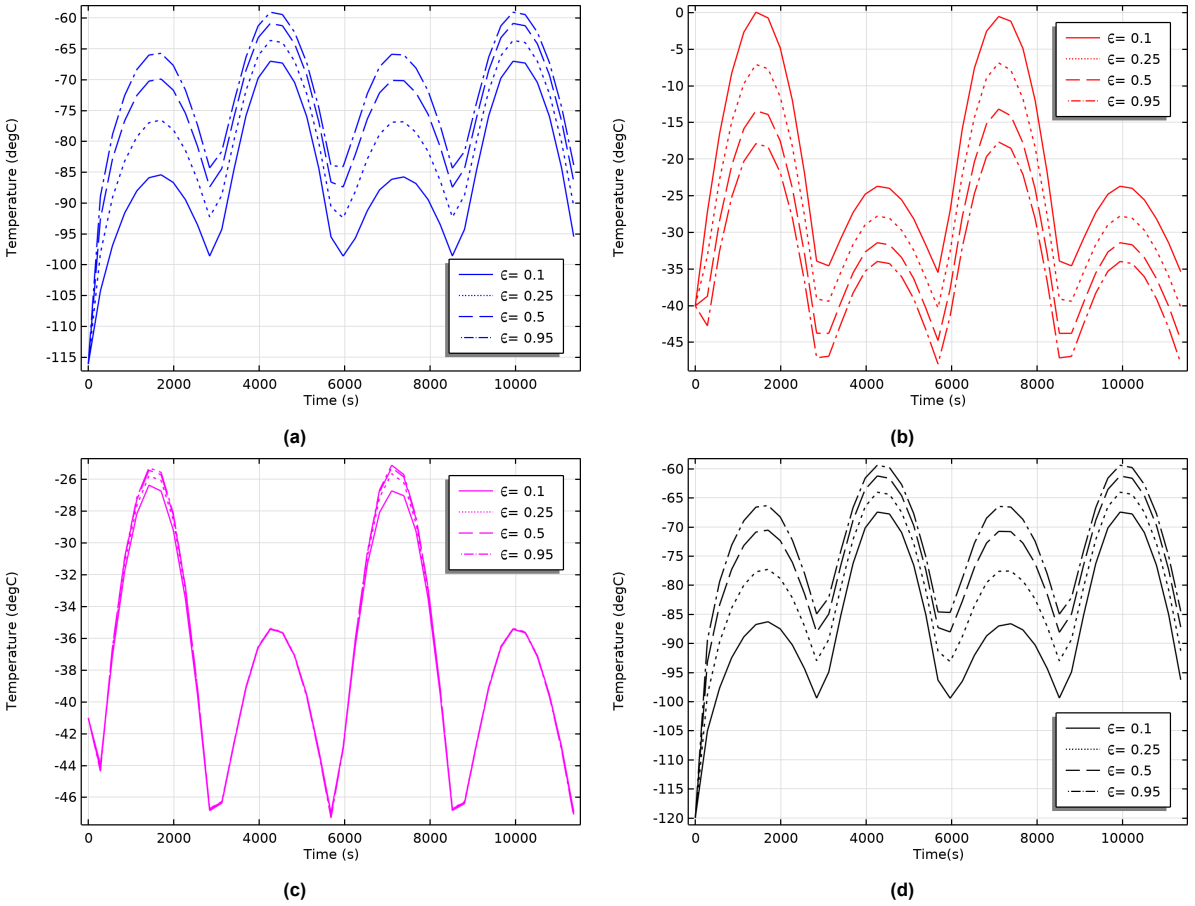

Figure 5.9: Simulated impact of altered emissivity on the inside of the patches on average temperature distribution across panel components: (a) frame, (b) patches, (c) top membrane, and (d) bottom membrane.

Varying the emissivity on the inside of the patches gives the results shown in Figure 5.9. It can be seen that only the patches, frame and bottom membrane are influenced on temperature. Due to the higher emissivity of the inside of the patches, a stronger radiative link is present between the patches and the bottom membrane. This results in an increase of temperature in the bottom membrane. As a direct response the frame increases in temperature as well, since they are thermally connected. Since the patches only have a varying emissivity the rest of the top membrane remains the same temperature due to the low thermal conductivity of the PI. A similar kind conclusion can be drawn when the emissivity is varied for the inside of the top membrane without the patches, see Appendix B.

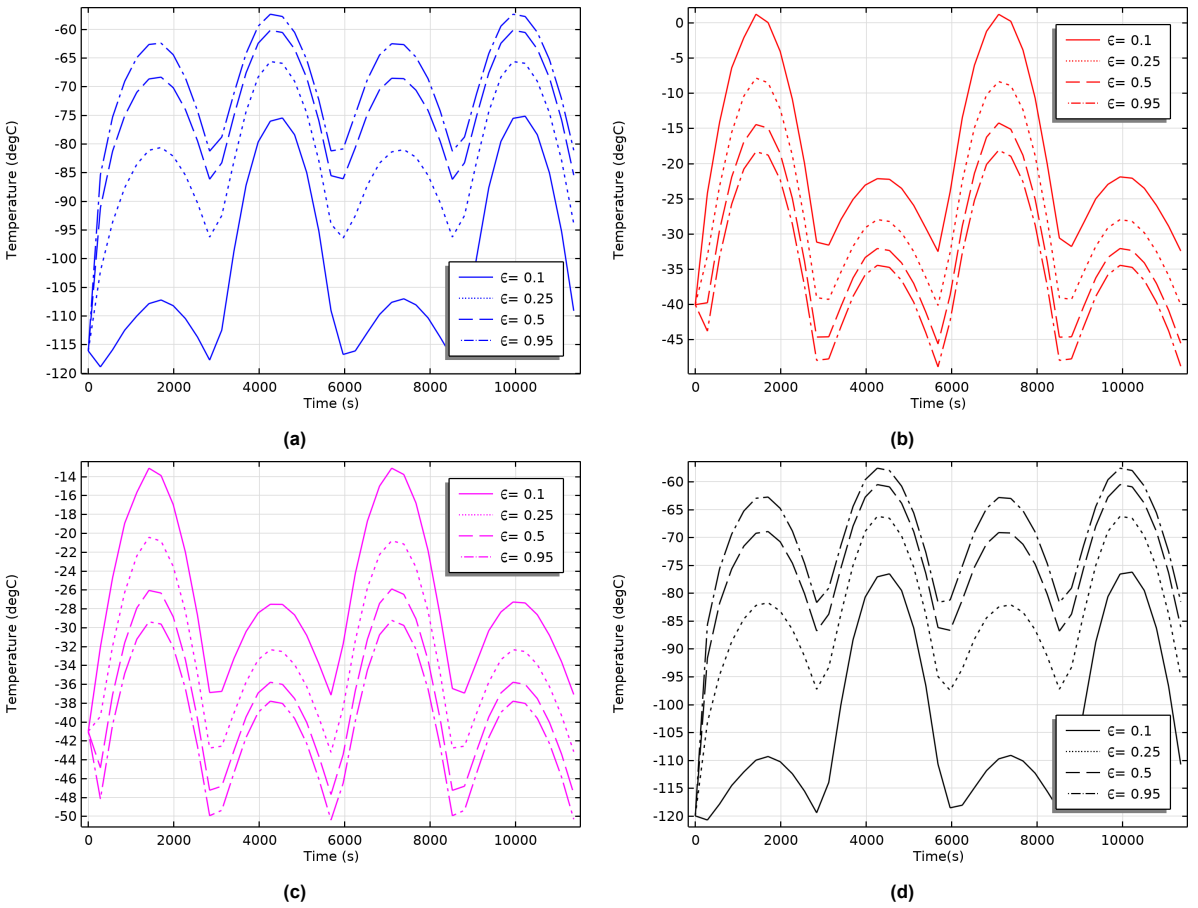

Figure 5.10: Simulated impact of altered emissivity on the inside of the bottom membrane on average temperature distribution across panel components: (a) frame, (b) patches, (c) top membrane, and (d) bottom membrane.

Similar to the emissivity change on the inside of the top membrane and the patches also a change in temperature is observed when the emissivity is varied on the inside of the bottom membrane, see Figure 5.10. With a higher emissivity a stronger radiative link is present between the two membranes. This results in a more equal temperature distribution within the panel. Resulting in a lower temperature for the top part and a higher temperature for the bottom part of the panel. with a stronger thermal link between the top and bottom membrane a more uniform temperature distribution is obtainable. One can thus conclude that if a more uniform temperature distribution is needed, all the inside surfaces need to have a high emissivity.

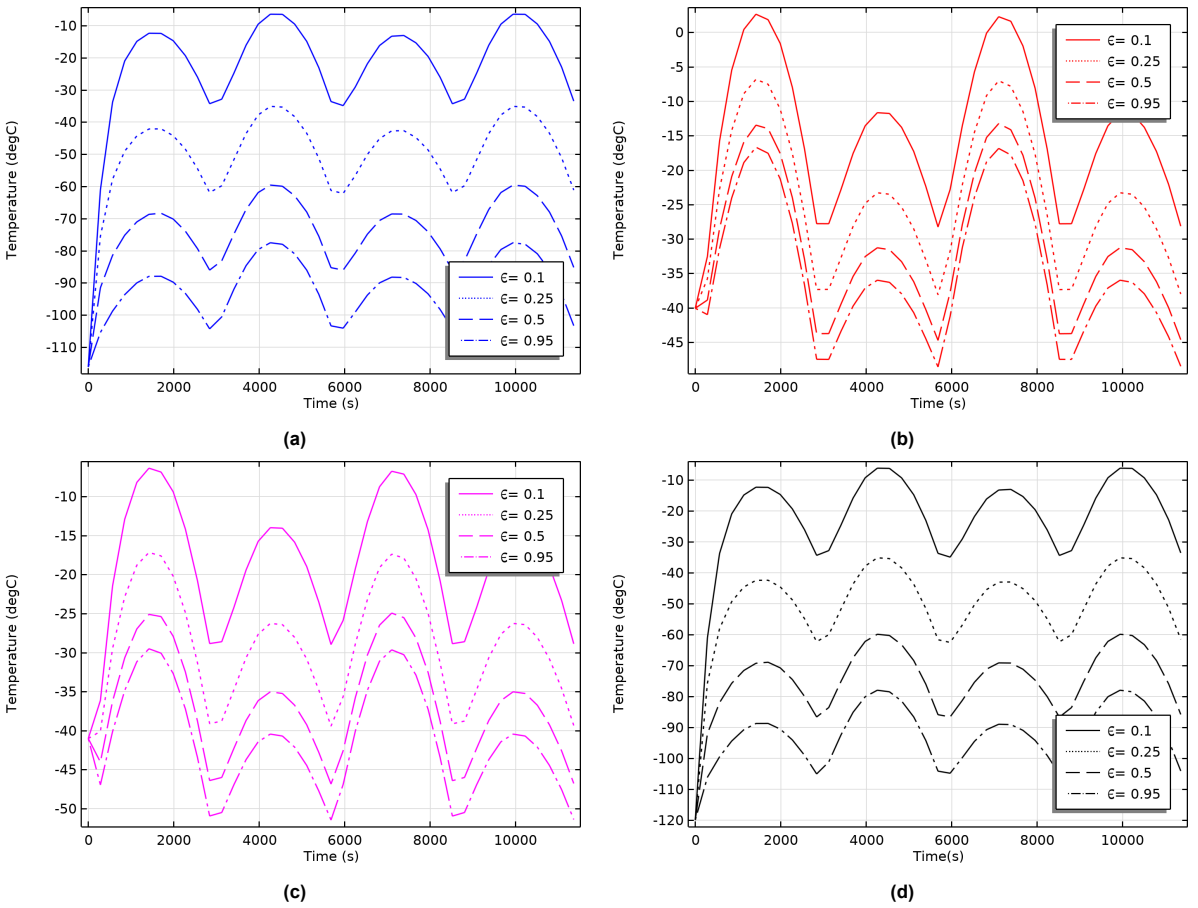

Figure 5.11: Simulated impact of altered emissivity on the outside of the bottom membrane on average temperature distribution across panel components: (a) frame, (b) patches, (c) top membrane, and (d) bottom membrane.

Figure 5.11 presents the results of the emissivity change of the outside of the bottom membrane. A temperature change of around $80\,^{\circ}\mathrm{C}$ can be observed for the bottom membrane with a change of emissivity. Due to this temperature increase also the other parts of the panel increase drastically in temperature. When lowering the emissivity of the outside of the bottom membrane, less heat is being ejected in the system compared to when the emissivity is high. Basically a thermal isolation is applied trapping the heat to stay in the system. In this case, this is preferable due to the low temperatures observed, increasing the temperature throughout the entire orbit everywhere on the panel.

A summary of the other results can be observed in Table 5.2. It can be seen that the surfaces with the highest impact are the bottom membrane facing both outwards as inwards and the top membrane facing inwards. No change is observed for the frame as could be expected from the absorptivity results. It should be noted that compared to the absorptivity results, where only part of the orbit is impacted, changing the emissivity impacts the panel on the entire orbit.

Table 5.2: Temperature impact across three orbital phases based on surface emissivity.

	Illumination on	Top	Side	Bottom
Patch out	Frame	Low	Low	Low
	Patch	Low	Medium	Low
	Top	Low	Low	Low
	Bottom	Low	Low	Low
Top out	Frame	Low	Low	Low
	Patch	No	Low	Low
	Top	Low	Medium	Low
	Bottom	No	Low	Low
Frame	Frame	No	No	No
	Patch	No	No	No
	Top	No	No	No
	Bottom	No	No	No
Bottom out	Frame	High	High	High
	Patch	Medium	Medium	Medium
	Top	Medium	Medium	Medium
	Bottom	High	High	High
Patch in	Frame	Medium	Medium	Low
	Patch	Medium	Low	Low
	Top	No	No	No
	Bottom	Medium	Low	Low
Top in	Frame	Low	Low	Low
	Patch	No	No	No
	Top	Low	Low	Low
	Bottom	Low	Low	Low
Bottom in	Frame	Medium	Medium	Medium
	Patch	Medium	Low	Low
	Top	Low	Low	Low
	Bottom	Medium	Medium	Medium

Material change

In Figure 5.12 the results are visualized for a change in thermal conductivity of the top membrane. Similar behavior can be observed in the panel as the parametric studies with a stronger radiative internal link. The top cools down and the bottom heats up. Due to better conductivity of the top sheet, now the heat can be more easily transferred from the top to the bottom. This results in the observed behavior. It should also again be noted that the temperature changes are throughout the entire orbit, as is the case with the variation of the emissivity.

Besides the temperature over time, also the cross section of the top sheet is interesting to analyse, see Figure 5.13. Using a more conductive material instead of PI results in less severe temperature jump in the top sheet. For a conductivity equal or higher then aluminium no significant temperature jumps can be observed in the top membrane as it converges to one average temperature. This can be seen more clearly by looking at the logarithmic scaled plot. Having a more conductive material as the top sheet results in lower temperature gradients in the top sheet itself.

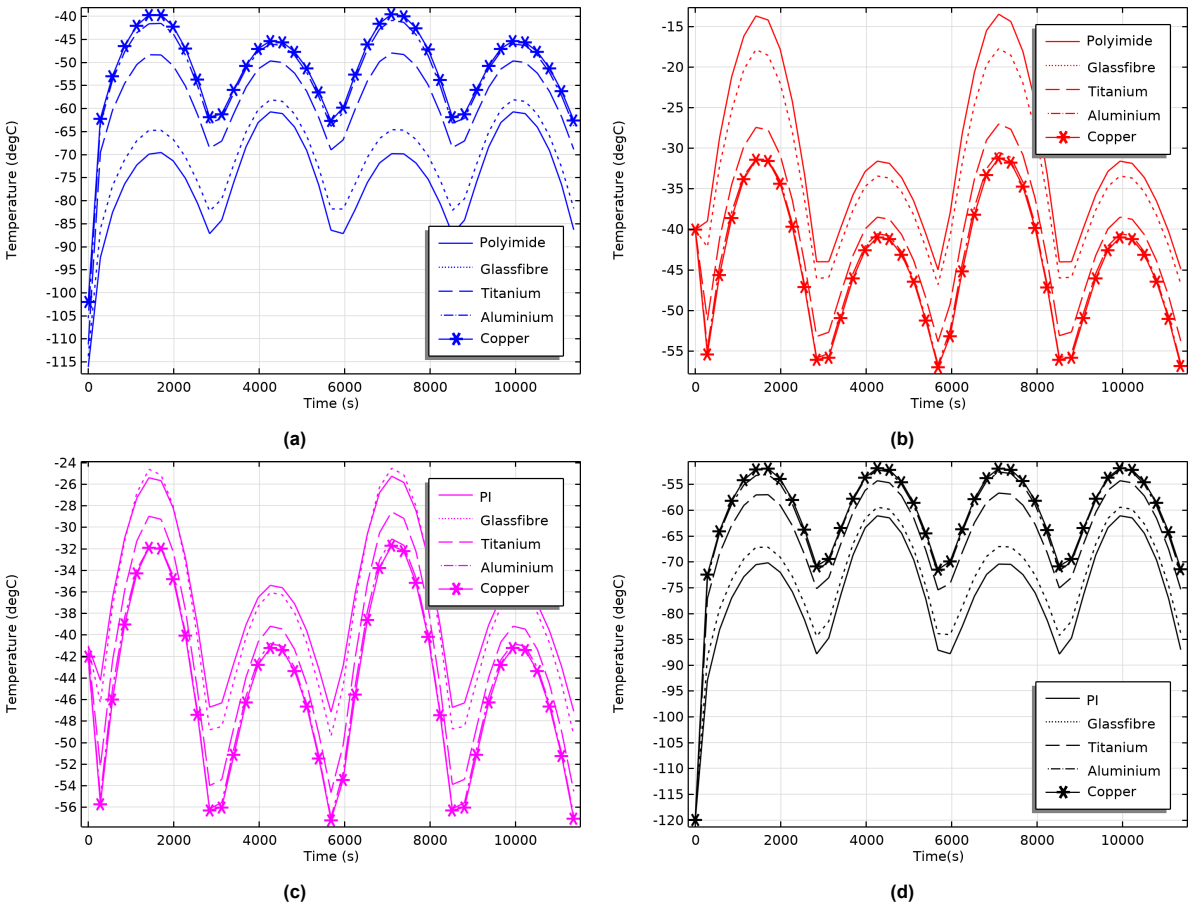

Figure 5.12: Simulated impact of altered material conductivity of the top membrane including the patches on average temperature distribution across panel components: (a) frame, (b) patches, (c) top membrane, and (d) bottom membrane.

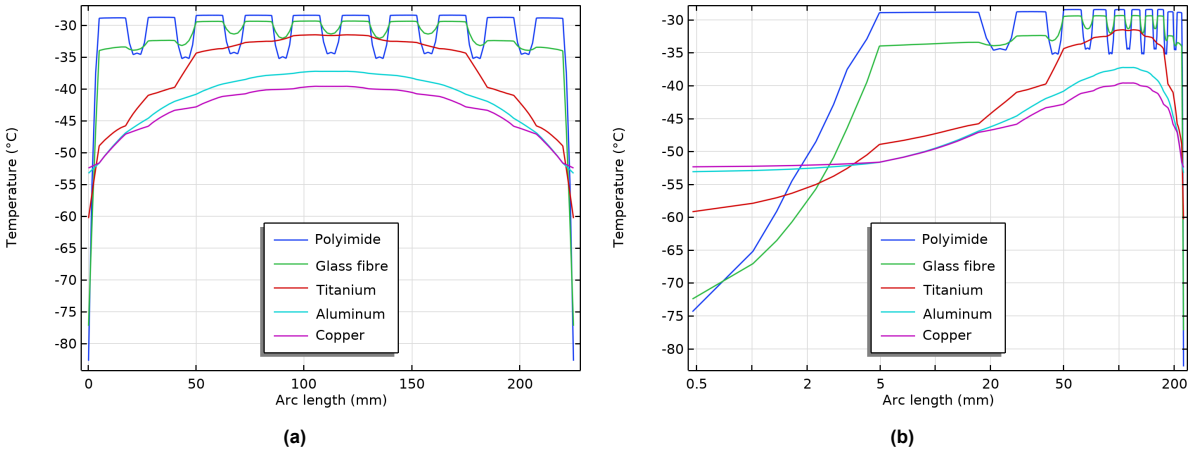

Figure 5.13: Temperature distribution across the top sheet at t=4257.7 seconds for an altered material conductivity of the top membrane. (a) Linear-scale temperature profile along the selected cross section. (b) Corresponding temperature profile plotted on a logarithmic scale to highlight finer variations.

the results for the other material change results are presented in Appendix B. For a change of conductivity of the frame little effect was observed on the temperature variations throughout the panel. A change was however observed for the temperature variation inside the top sheet, see Figure 5.14. With an increase of conductivity in the frame, the temperature variation increases in the top sheet. This can be explained due to the following. With a higher conductivity in the frame, a better thermal link

is present between the top and bottom membrane. With the high emissivity of the bottom membrane facing outwards the more heat can be ejected form the top membrane. This lowers the temperature in the frame and results in the observed behavior.

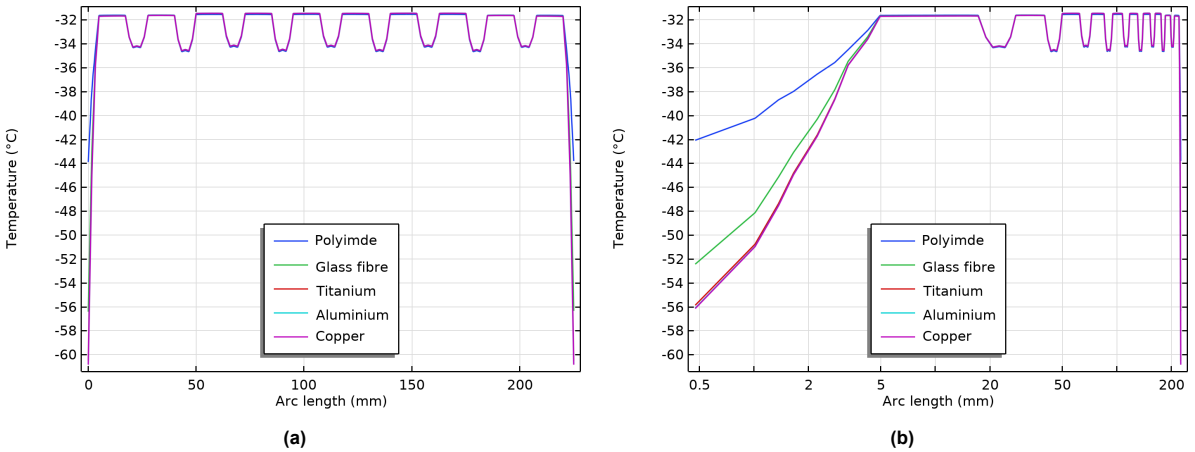

Figure 5.14: Temperature distribution across the top sheet at t=4257.7 seconds for an altered material conductivity of the frame. (a) Linear-scale temperature profile along the selected cross section. (b) Corresponding temperature profile plotted on a logarithmic scale to highlight finer variations.

Orbital Angle Variations

The orbital angle is varied to know the effect on the thermal behavior of the panel, the results are presented in Figure 5.15. It can be observed that only minor temperature variations are present in the bottom part of the panel and the top membrane. A larger effect is observed in the patches, due to the higher absorptivity, this part is more influenced by the incident angle of the solar rays. It should also be noted that besides the temperatures varying also the lines can become shifted over time. This is especially highlighted with the frame and bottom membrane. The observed temperature variations can be classified as low with the maximal observed change lower then $20\,^{\circ}\mathrm{C}$. Hence orientation of the panel is something to keep in mind if very strict temperature requirements are required, but otherwise do not cause a large change in temperatures.

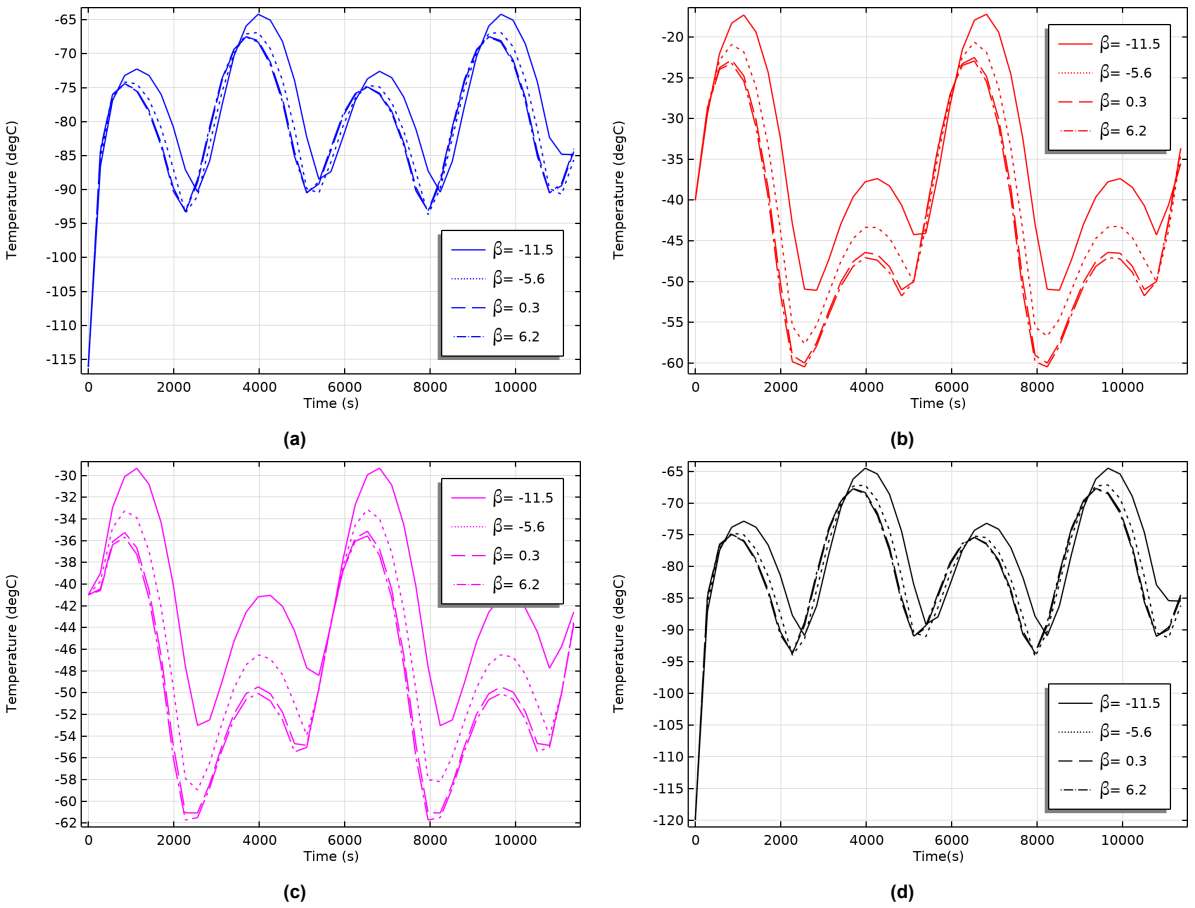

Figure 5.15: Simulated impact of orbital angle variation on average temperature distribution across panel components: (a) frame, (b) patches, (c) top membrane, and (d) bottom membrane.

Array of Panels and Panel Size

Lastly, the size of the panels was studied by varying the amount of patches on the panel and also the influence of an array of panels was studied. First the size of the panels was varied and the results are shown in Figure B.10. It can be seen that the size has little to no influence on the average temperature of the patches, frame and bottom membrane. On the other hand it does have an influence on the average temperature of the top membrane. This is due to the fact that the fraction of the frame in comparison to the total surface area decreases when the size of the panel increases. The frame has a lower temperature than the surface, meaning that increase in size results in a higher average temperature for the top frame.

Besides altering the size of the panel also an array of panels was created to understand this thermal behavior. However no change was observed in any of the different panels regardless of the amount and type of connections. This can be explained by the very thin sides. As seen in the influence of the absorptivity of the frame, there is no noticeable change anywhere on the panel. The amount of heat going into the system from the top and bottom is much larger than from the sides. Shadowing the side of a panel by adding another in front of it by creating an array has thus no effect. The amount of panels and type of connections have thus no influence on the temperature distribution of the array.

All of the remaining results are summarized in the Table 5.3. This table includes the results of material and thickness variation, orbital angle change and panel size variation. No significant temperature change was observed when varying the thickness of certain panel components. This aligns with the conductive link equation, where both material and thickness scale linearly with conductivity. However, materials typically offer much larger conductivity factors than thickness changes. For example, achieving a 1000× increase in conductivity could be done by selecting a material with 1000× higher thermal

conductivity, whereas reaching the same effect through thickness alone would require a 1000× increase in thickness. The graphs for the remainder of the results not shown in this Chapter, can all be found in Appendix B.

Table 5.3: Temperature impact across three orbital phases for each parameter: material, thickness, orbital angle, and panel size.

	Illumination on	Top	Side	Bottom
Material bottom PI	Frame	No	No	No
	Patch	No	No	No
	Top	No	No	No
	Bottom	No	No	No
Material frame	Frame	Low	Low	Low
	Patch	No	No	No
	Top	No	No	No
	Bottom	No	No	No
Material top pi	Frame	Medium	Medium	Low
	Patch	Medium	Medium	Low
	Top	Low	Low	Low
	Bottom	Medium	Low	Low
Thickness bottom PI	Frame	No	No	No
	Patch	No	No	No
	Top	No	No	No
	Bottom	No	No	No
Thickness frame	Frame	No	No	No
	Patch	No	No	No
	Top	No	No	No
	Bottom	No	No	No
Thickness top pi	Frame	No	No	No
	Patch	No	No	No
	Top	No	No	No
	Bottom	No	No	No
Orbital angle	Frame	Low	Low	Low
	Patch	Low	Low	Low
	Top	Low	Low	Low
	Bottom	No	Low	Low
Panel size	Frame	No	No	No
	Patch	No	No	No
	Top	No	No	No
	Bottom	No	No	No

5.3 Thermo-Elastics

In Figure 5.16 the deformation in the z-direction of the top membrane including the patches is visualized for an increase of $5\,^{\circ}\mathrm{C}$. It can be seen that the general trend of the sheet is downward going further in the x-direction. The maximal observed displacement is around $-0.3\,\mathrm{mm}$ but there is also a positive displacement at two patches in the middle closest to the other edge. It can be seen that the deformation is symmetric around the x-axis, this is due to the symmetric imposed boundary conditions and the shape of the structure. Figure 5.17 visualizes the deformation in the z direction for the bottom membrane. It can be seen that the amount of deformation almost doubles for the bottom membrane compared to the top membrane. Since the PI has a higher CTE than CU, it can be explained why the deformed membrane goes downwards with an increase of temperature. This also results in much more deformation than is observed in the top membrane. The PI wants to deform more than the CU, hence it displaces into a position where the PI has a higher radius of curvature and thus more length. It should also be noted that the edge of the bottom membrane has the same amount of displacement as the top membrane. This indicates that the frame should have a similar degree of deformation, as is the case, see Figure 5.18. Here the maximal deformation is again around $-0.3\,\mathrm{mm}$ as can be more clearly be seen in Figure 5.19. There is also a slight bending of the far edge of the frame due to the temperature increase, but this is barely visible in the figure. With the maximal deformation of the frame being $-0.3\,\mathrm{mm}$, requirement Ar-006 is satisfied for a temperature increase of $5\,^{\circ}\mathrm{C}$.

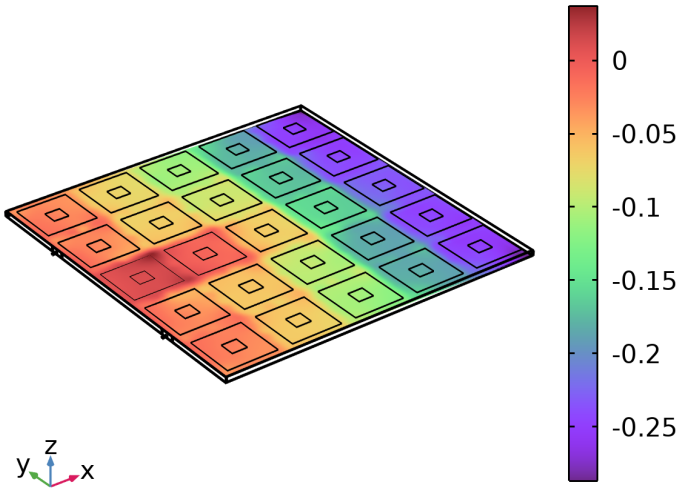

Figure 5.16: Deformation of the top membrane resulting from a temperature increase of $5\,^{\circ}\mathrm{C}$, relative to a reference temperature of $20\,^{\circ}\mathrm{C}$. Deformation is in z-direction and in mm.

Having established the overall deformation characteristics, attention can now be turned to assessing the remaining system requirements. Starting with the yield stress, it can be observed that the highest stress is found in the top layer of the bottom membrane. Indeed, this is in the CU layer. The maximal observed stress is positioned in every corner in the ground plane, with one example shown in Figure 5.20. The maximal stress observed is $20\,\mathrm{MPa}$, still well away from the yield strength of $68\,\mathrm{MPa}$. It can be expected that when the temperature increases however even more, the stress will increase even more as well getting closer to the yield strength of the copper. With the current temperature increase no yielding will occur, satisfying requirement Ar-007.

Next, the two remaining antenna requirements are evaluated, beginning with the surface accuracy of the top membrane. In Figure 5.21 the deformation of both the membranes are plotted, including a second order polynomial fit. In Figure 5.22 the surface accuracy is plotted, also for both membranes. It can be seen that the surface accuracy for both the top and bottom membranes are well within the

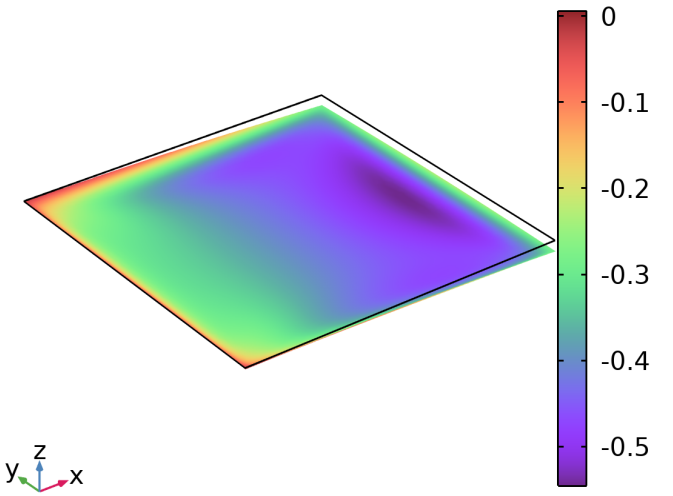

Figure 5.17: Deformation of the bottom membrane resulting from a temperature increase of $5\,^{\circ}\mathrm{C}$, relative to a reference temperature of $20\,^{\circ}\mathrm{C}$. Deformation is in z-direction and in mm.

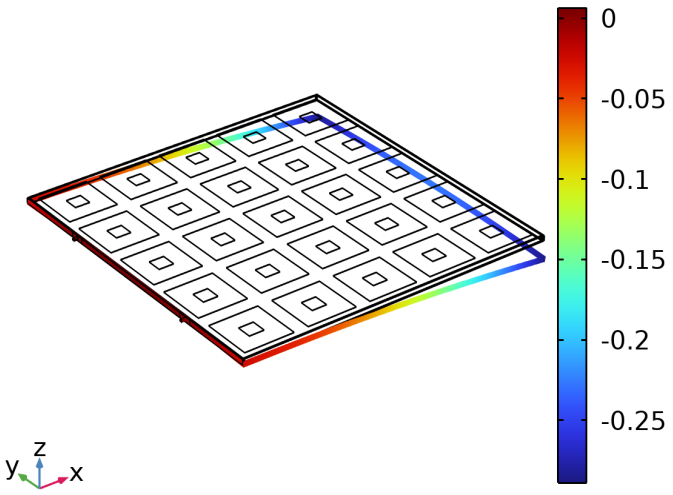

Figure 5.18: Deformation of the frame resulting from a temperature increase of $5\,^{\circ}\mathrm{C}$, relative to a reference temperature of $20\,^{\circ}\mathrm{C}$. Deformation is in z-direction and in mm.

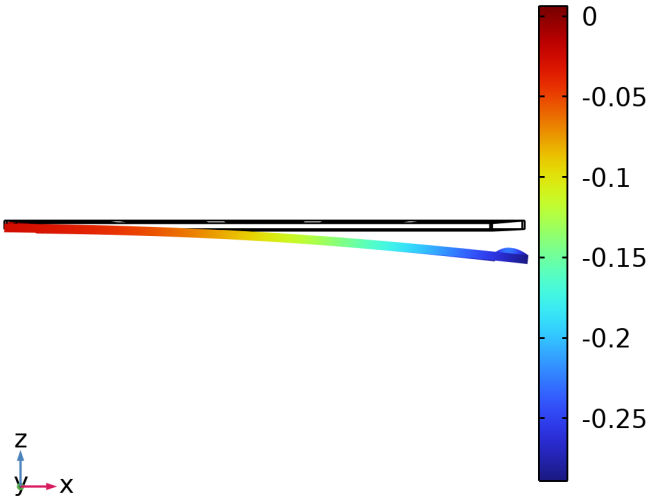

Figure 5.19: Side view of the deformation of the top membrane resulting from a temperature increase of $5\,^{\circ}\mathrm{C}$, relative to a reference temperature of $20\,^{\circ}\mathrm{C}$. Deformation is in z-direction and in mm.

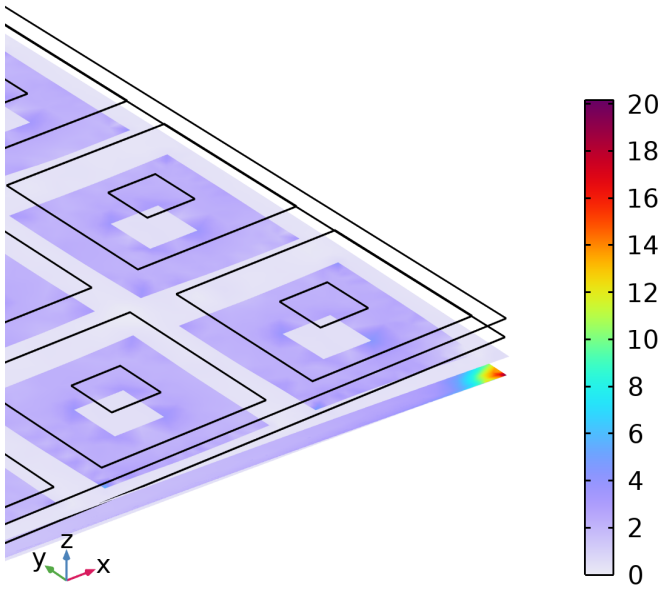

Figure 5.20: Stresses in the membranes resulting from a temperature increase of $5\,^{\circ}\mathrm{C}$, relative to a reference temperature of $20\,^{\circ}\mathrm{C}$.

allowable tolerance limits of $0.5\,\mathrm{mm}$. This means that Ar-005 is satisfied.

Lastly the distance between the two membranes is computed and the difference with the original distance is plotted in Figure 5.23. It can be observed that at two instances the allowed deviation is exceeded and along a large portion the deviation is close to the allowed deviation. This means that requirement Ar-004 is violated at a temperature increase of $5\,^{\circ}\mathrm{C}$.

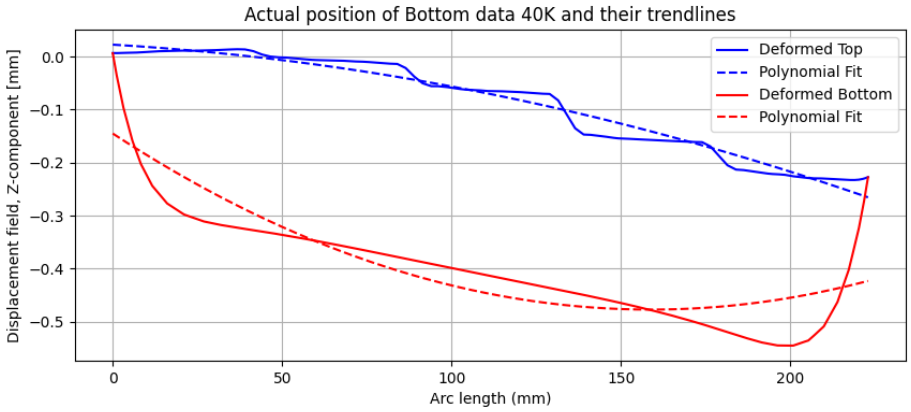

Figure 5.21: Comparison of the deformed top and bottom membranes relative to their original positions in the z-direction, including second-order polynomial trend lines fitted to the displacement data.

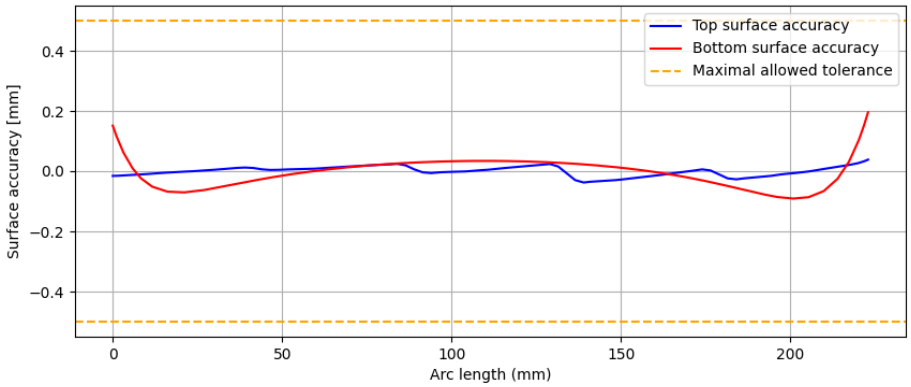

Figure 5.22: Surface accuracy assessment for the top and bottom membranes, based on the deviation between the deformed displacement profiles and their corresponding second-order polynomial trend lines.

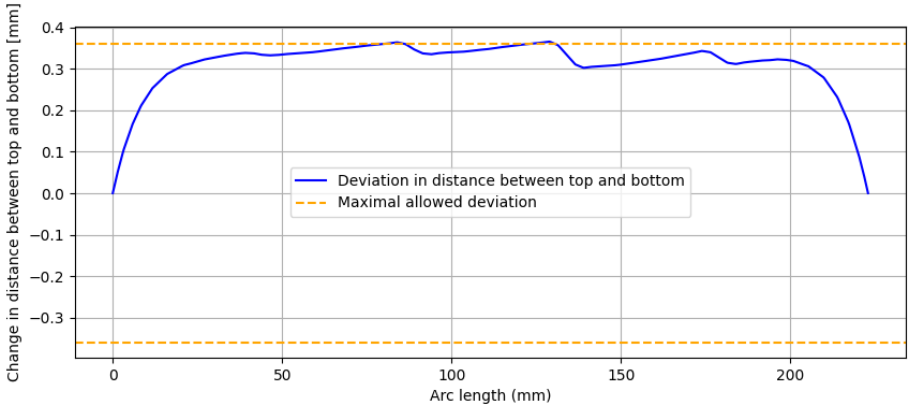

Figure 5.23: Vertical separation between the top and bottom membranes under thermal loading conditions.

5.4 Deployment

This section presents the results for the first and third phase of deployment. Both the normal support and additional supported panels are covered. For the third phase of deployment the deformation of the membranes and the maximal stresses are plotted.

Normal support

During the initial phase of deployment, the spring applies force to the frame, initiating its movement and enabling the deployment process. It is important to see if the acting force does not cause any permanent deformation to the structure. Hence the stress should not be higher than the yield stress. The results indicate that the highest observed stress in the frame is lower than $0.8\,\mathrm{MPa}$ and the stress in the membrane is lower than $0.07\,\mathrm{MPa}$. This means that the stresses are much lower than their respective yield stresses. The figures of the results are presented in Appendix C. The highest stress is mainly observed in the cylinder that approximates the torsional spring and its connection, but not the frame itself.

In Figure 5.24 the z position of the mid point of the membranes is plotted during the third phase of the deployment. It can be seen that the membranes go downward as is the direction of deployment. It can also be seen that the position of the mid points for the top and bottom membranes intersect, which means that they would touch each other. This should be avoided since damage could be done to the membranes, degrading the performance of the RA. Besides hitting each other, the membranes have different amplitudes and frequencies of their dynamic vibrations. It can be seen that the top membrane has more displacement compared to the bottom membrane for example. The bottom membrane has more CU compared to the top membrane, this makes this membrane more stiff since CU has a higher E-modulus than PI. This can be observed in the figure by the lower amplitude of the bottom sheet compared to the higher amplitude of the top sheet, which have the values 8.7 mm and 12 mm respectively. Additionally, it can be seen that the higher frequencies slowly damp out, especially in the bottom sheet where the high frequency responses appear to be mostly gone after 0.6 seconds. However there is also a difference in frequency between the responses of the top and bottom, being around $3\,\mathrm{Hz}$ and $4\,\mathrm{Hz}$ respectively.

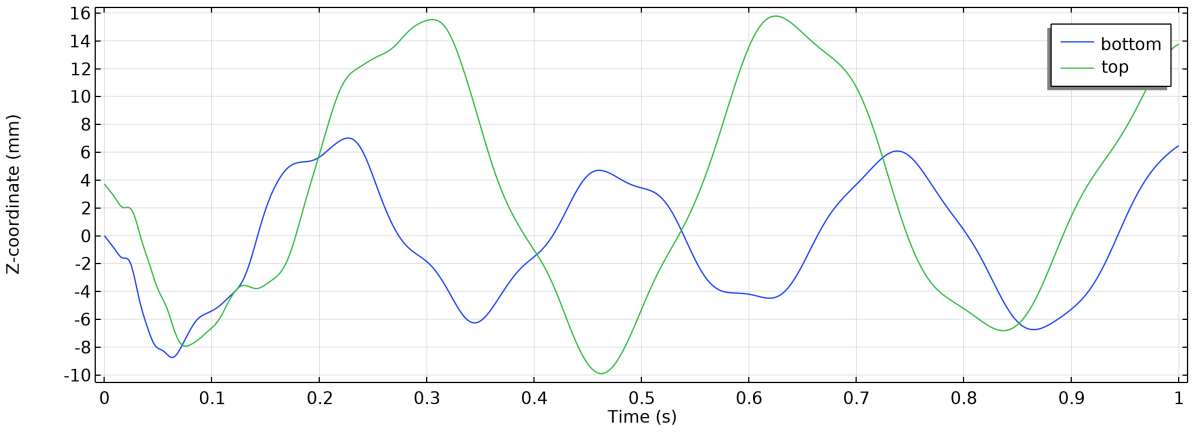

Figure 5.24: Midpoint z displacement over time for both the top and bottom membrane, without any additional support added to the panel.

Besides the deformation it is also important to look at the observed stresses in the structure and see if they are not too high such that plastic deformation takes place. Hence the maximal Von Mises stresses for each material in relevant groups have been plotted. To begin, the stress distribution in the aluminum frame is examined (see Figure 5.25). It can be observed that the maximal stress observed over the plotted data is right at the beginning of the response. A peak stress of around $8.5\,\mathrm{MPa}$ is observed, but this is significantly lower than yield stress of AL. Hence it is not expected that the frame will hence fail with the given impact velocities. The maximum stresses are mainly observed in at the edges close to the corners, see Figure 5.26. This is due to the observed bending of the structure. At the top and bottom

sides the stress is higher in the frame. When the frame moves upwards, the bottom side experience tension and the top side compression. The observed stresses are however always positive. This is due to the way the Von Mises stress is calculated.

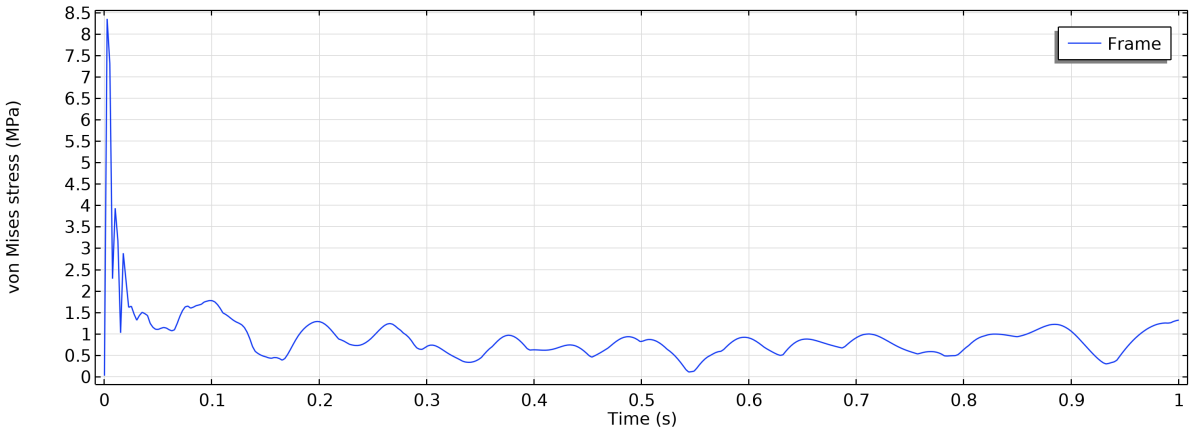

Figure 5.25: Maximum observed frame stresses over time with normal support

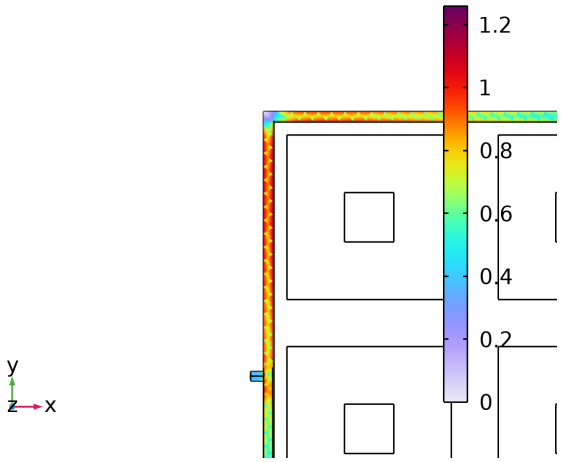

Figure 5.26: Location of maximum stress in the frame at t=0.20301 seconds with normal support

Next to the frame also the stresses in the membranes should not exceed the yield stress. Hence, by splitting up the membrane geometry into five parts this can be analysed. Starting with plotting all the stresses in the PI, see Figure 5.27.

The PI is split into three parts: the PI layer in the ground layer, the PI under the patches, and the rest of the PI in the top membrane. It can be seen that the stress in the top sheet is significantly higher, by more then a factor 2, than the other two observed stresses. However, for all stresses an initial peak stress is observed in the beginning, after which the stress slowly transitions into a smoother periodic response with decreasing amplitude for the patch and ground PI stress. The stress in the top sheet also gets a more periodic response but still quite unpredictable. It can be observed that the response can be related back to the displacement curves of the membranes. However, due to the Von Mises stress the values do not go below $0\,\mathrm{MPa}$ and will remain positive at all times. Hence when the membranes displaces downwards the stress increases again, instead of becoming negative.

The higher stress observed in the top sheet can be explained by examining the specific locations where these stresses occur. As shown in Figure 5.28a, stress concentrations are present at the corners of the patches. When these would be ignored the highest observed stress is a factor 2 lower, as is observed

between the patches. However, the highest observed stress is still a much lower than the yield stress of PI which is $103\,\mathrm{MPa}$. Other examples of the highest observed stress in the relevant parts can be seen in Figure 5.28b for the PI patch layer and in Figure 5.28c for the PI ground layer. In both the observed stress distributions, no stress concentrations can be observed, but a more smooth distribution. Both are highly dependent on the shape the membrane takes. The highest stress in the PI layer of the patches is observed in the corner patches since there the gradient of displacement is highest. The highest stress in the PI ground layer is observed near the edges since here also the gradient of displacement is highest.

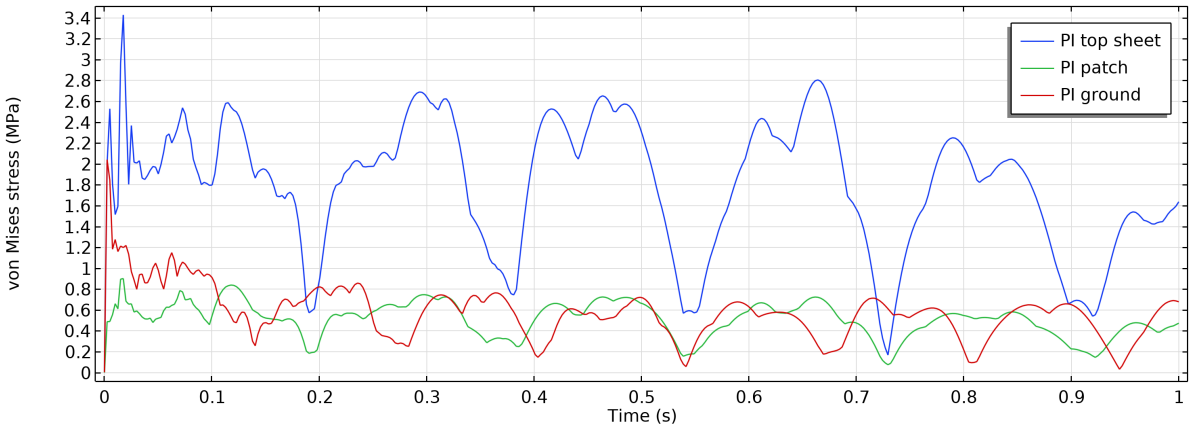

Figure 5.27: Maximum observed PI stresses over time with normal support

Lastly, the stresses in the CU layers can be observed in Figure 5.29. Again, a peak is observed in the beginning of the response for the CU layer of the ground. However, after this initial peak the stress lowers significantly and stabilizes. The stress of the CU layer of the patches follows a very close trend shape as the observed stress in the PI layer in the patches. This can be explained by the fact that they are thin layers and are bonded together and thus have the same displacement. The maximal stress observed is around $18\,\mathrm{MPa}$ and thus well below the yield strength of copper, as it is $68\,\mathrm{MPa}$. The peak stress is observed to be in the ground, specifically in the corners. The high stresses in the patches occur however at multiple occasions and reach almost $15\,\mathrm{MPa}$. The stress distributions for the two CU layers can be seen in Figure 5.30a for the patches and Figure 5.30b for the ground. Similar results can be observed for the stress distributions as for their PI counter parts. The stresses are highest in the corner patches and at the edges of the ground layer.

In Figure 5.31 the amount of energy and the three main components are plotted over time. It can be seen that the amount of energy decreases as time passes. In the beginning is reduces quite quickly but the amount of energy reduces less after $0.1\,\mathrm{sec}$. Then the energy reduces only marginally. The observed reduced energy reduction is due to the applied Rayleigh damping.

The total energy in the system consists of the total kinetic energy in the membrane, the total elastic strain energy in the membranes, and the total energy in the solids. In the plot it can be observed that when the total elastic strain energy decreases, the amount of total kinetic energy increases. This indicates a mutual exchange between kinetic and strain energy. This is logical due to the observed movements. Initially there is only kinetic energy in the system since no stress is present in the system. Once the system starts to displace some of the kinetic energy is absorbed in the system as elastic strain energy. Once the system has reached it furthest point, all of the kinetic energy is transformed into elastic strain energy. After this point, the system moves the other direction, continuing its movement. Then the kinetic energy increases again while the elastic strain energy decreases. In addition to this exchange, some energy is transferred from the membranes into the solid parts of the panel. However, the energy stored in the solids remains significantly lower than that in the membranes. Due to the rapid reduction in total energy, it is unclear whether the applied damping is appropriate. This aspect may need to be revisited in future analyses.

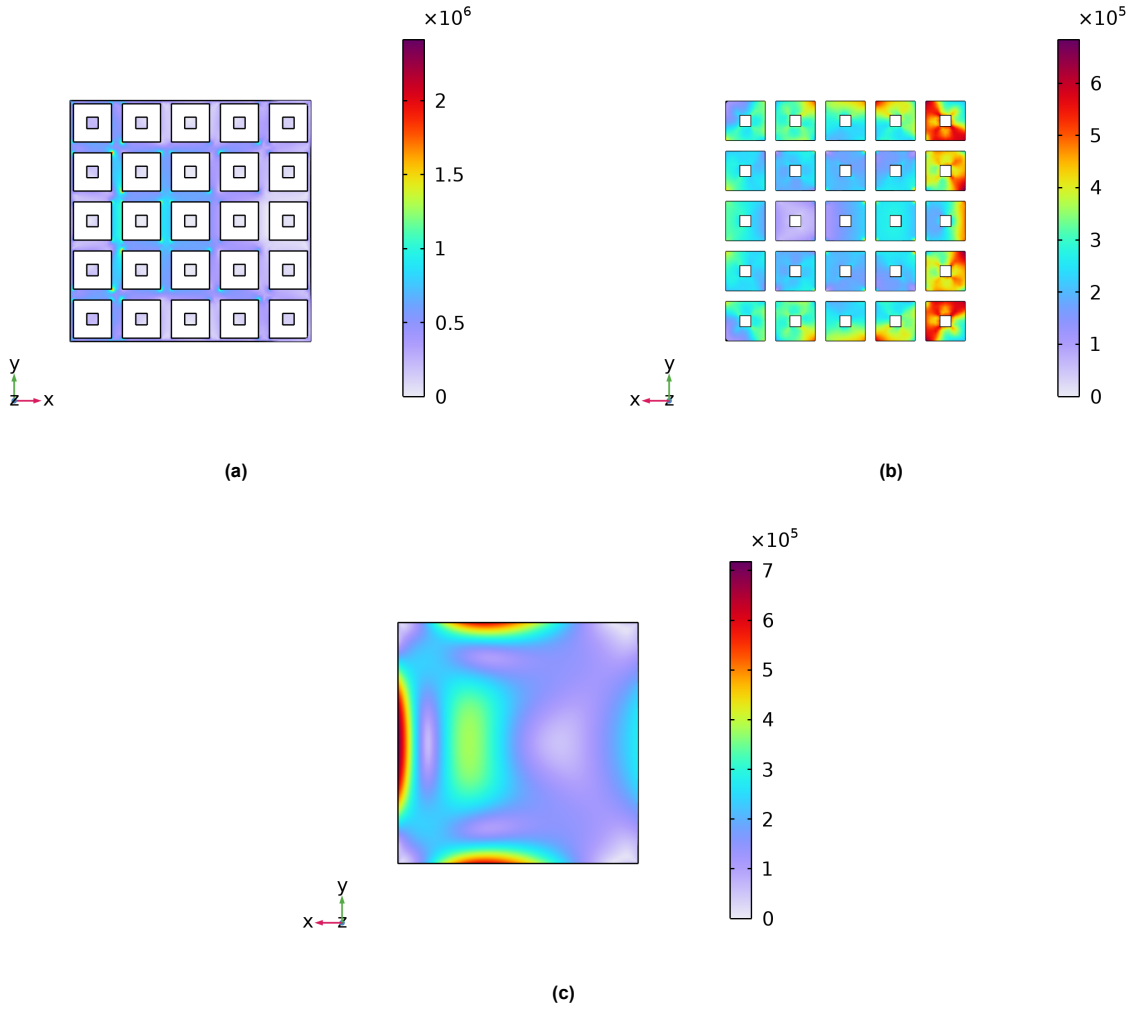

Figure 5.28: Stress distributions in polyimide components at t=0.4962 seconds with normal support: (a) top sheet, (b) patch layer, and (c) ground plane layer.

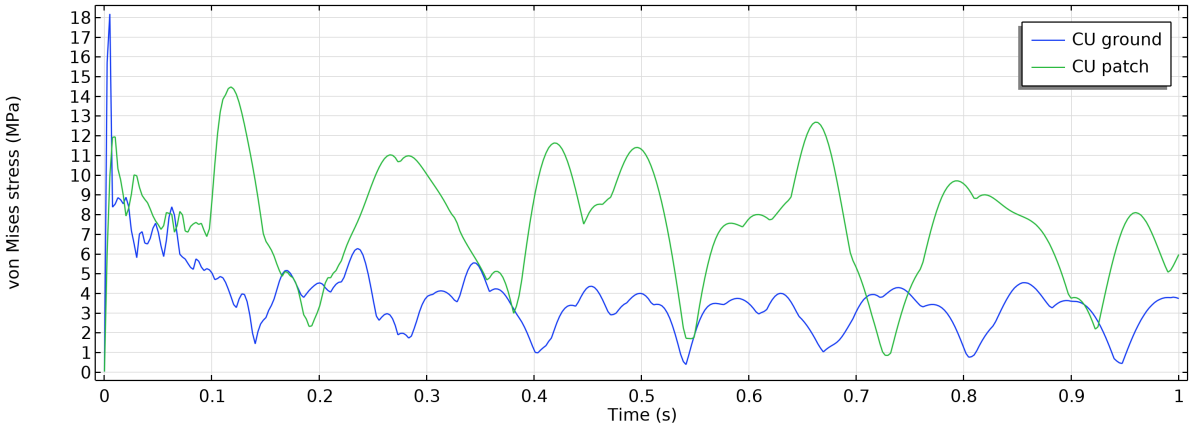

Figure 5.29: Maximal observed CU stresses over time with normal support

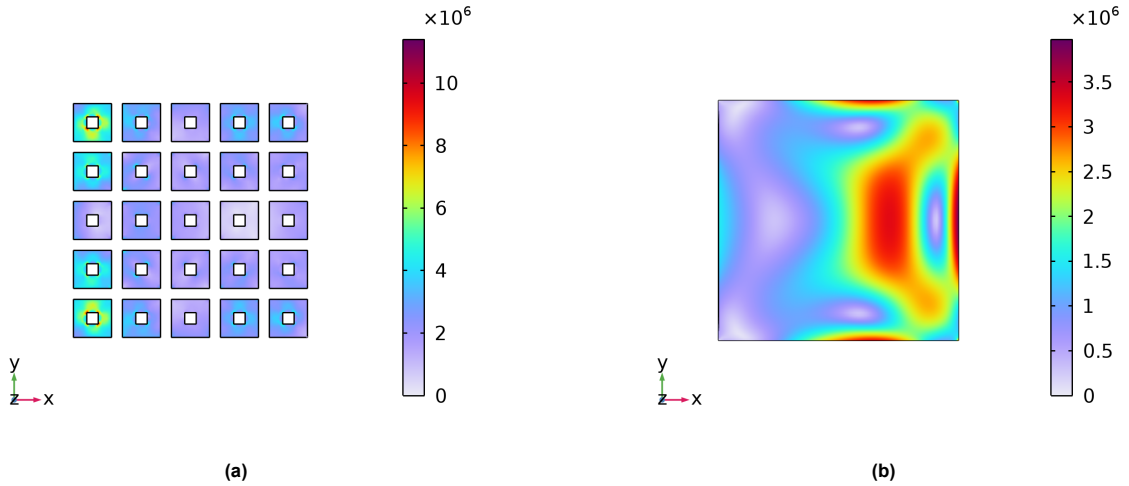

Figure 5.30: Stress distributions in CU components at t=0.4962 seconds: (a) patches, (b) ground plane layer.

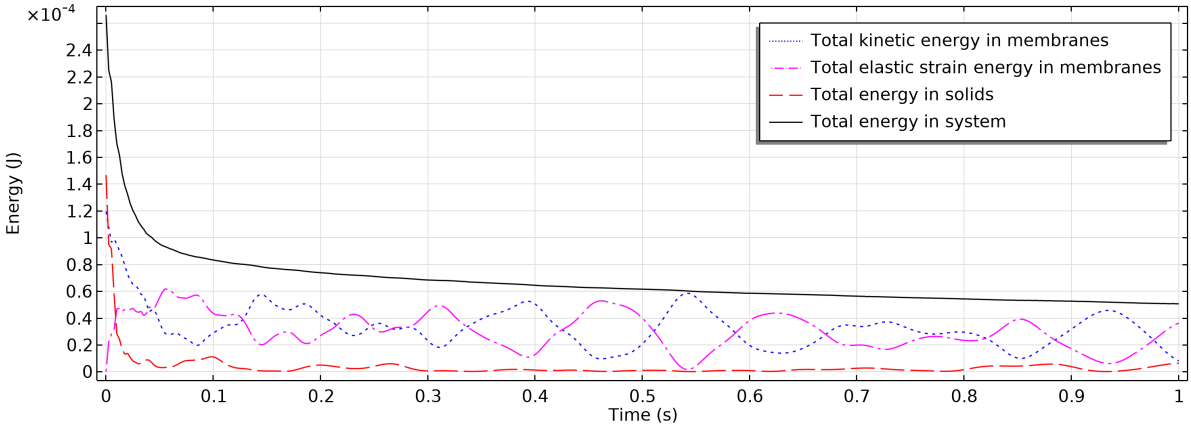

Figure 5.31: Energy in the system over time with normal support

Additional support

Since the membranes impact each other during this phase of deployment it can be concluded that the amount of displacement is too high. To address this issue, additional support was added to the panel. This modification divides the membranes into four sections. However, due to the panel's symmetry, only two sections are relevant for analysis: the one closest to the spring hinge and the one furthest from it.

In the first phase of deployment, the response remains nearly unchanged compared to the configuration with normal support. The results, presented in Appendix C, show similar stress values.

For the third phase of deployment, the displacements at the midpoints of these two sections were plotted again, as shown in Figure 5.32. The figure contains four graphs: each pair with similar amplitude corresponds to the same section of the panel, with one graph showing the displacement of the top membrane and the other showing the bottom membrane.

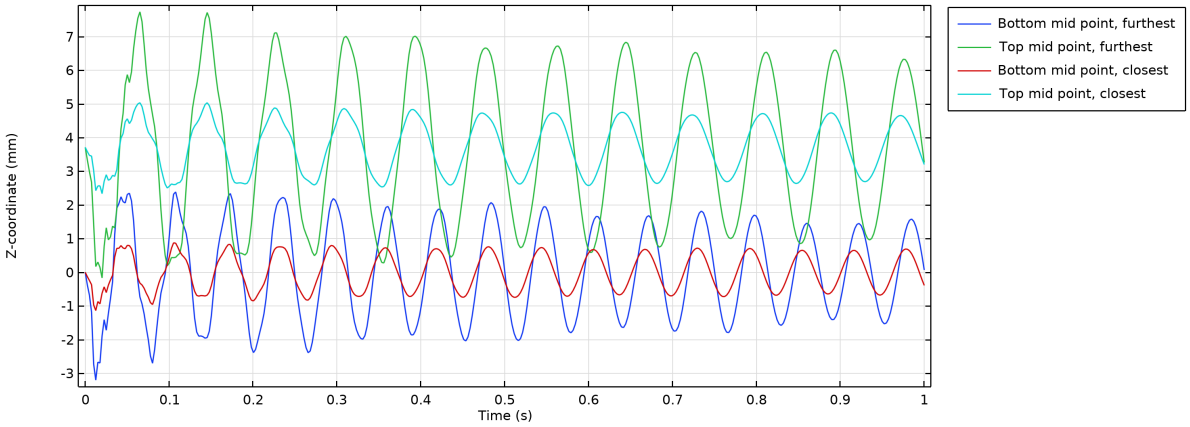

Figure 5.32: Midpoint z displacement over time for both the top and bottom membrane, with additional support added to the panel.

It can immediately be seen that these responses are different from the responses of the normal supported panel. First of all, the amplitude of the deformations in the z-direction for the top and bottom membrane decreased to 4 and 3 mm, respectively. Besides the amplitude reduction also the frequency of the moving membranes increased. Where the frequency before was in the range of 3-$4\,\mathrm{Hz}$ it is now more towards 12-$16\,\mathrm{Hz}$ for the top and bottom membrane respectively. Again, the high frequency response can be seen damping out during the beginning of the response, as it stops at the end of the first vibrational wave. It takes longer till the responses follow a nicely shaped sinusoidal wave, after around $0.4\,\mathrm{sec}$. This is due to the mid point being selected to visualize the deformation. However, in the beginning the response of each part of the membrane is not twice symmetric. Since the impact speed increases with distance, a piece of membrane has a higher impact further from the spring hinge than a piece of membrane closer to the axis of rotation. This insight also applies to the difference in amplitude of the closest and furthest part of the membrane. Since the furthest part is further from the axis of rotation also the impact speed increases, resulting in the observed higher amplitude. Even though the amplitude of the z displacement decreased significantly, still the membranes touch each other. This is undesirable since the membranes could damage each other.

In addition to displacement, stress levels remain a critical factor. Starting with the maximum observed stresses in the frame, Figure 5.33 shows a peak of approximately $7.5\,\mathrm{MPa}$ occurring within the first few steps after deployment. This peak quickly drops to around $1\,\mathrm{MPa}$, accompanied by high-frequency vibrations.

After approximately 0.4 seconds, the system settles into a periodic response characterized by two dominant frequencies: a lower frequency of about $4\,\mathrm{Hz}$ and a higher frequency of approximately $28\,\mathrm{Hz}$, which is roughly seven times greater. The amplitude of this periodic response gradually decreases over time, indicating a damping effect.

The maximum stresses in the frame of the additionally supported panel are located near the added support, specifically in the outer sections. This is illustrated in Figure 5.34.

While this suggests that these regions may benefit from increased thickness to reduce stress concentrations, the observed stress levels remain well below the material's yield strength, indicating that structural integrity is not compromised.

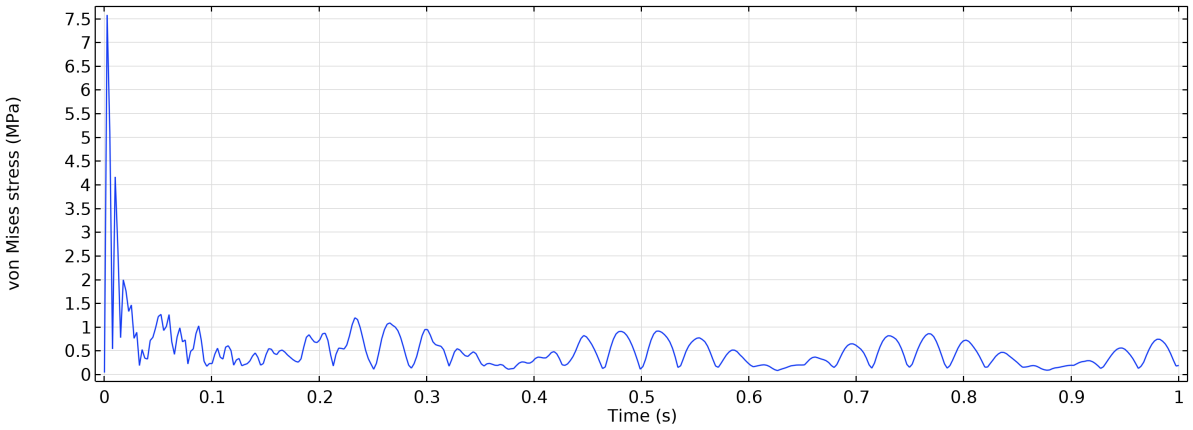

Figure 5.33: Maximum observed frame stresses over time with additional support.

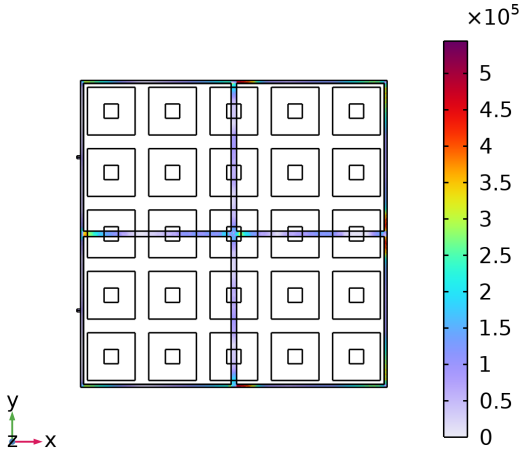

Figure 5.34: Location of maximum stress in the frame at t=0.4962 seconds with additional support. Values indicate the stresses in MPa.

The maximum stresses in the PI layers for the additionally supported panel are shown in Figure 5.35. As before, the highest stresses occur in the PI top layer, exceeding those in the PI patch and ground layers. After an initial peak, the stress response gradually transitions into regular sinusoidal oscillations around 0.5 seconds, as the high-frequency components are damped out.

A periodic response similar to that observed in the frame becomes visible after this point, although it is less pronounced. The maximum stress in the PI top sheet reaches approximately $7\,\mathrm{MPa}$, as indicated in Figure 5.36a. Stress concentrations are again found at the corners of the patches, while the regions between patches experience stresses more than two times lower.

Figure 5.36b shows the stress distribution beneath the patches. The highest stresses are observed in the far-left section of the membrane, particularly at the corners of some patches. These elevated stresses consistently occur near the edges of the additional support, while other areas show stress levels roughly half as high.

Finally, Figure 5.36c presents the stress distribution in the PI ground layer. The highest stresses are located at the edges of the square membrane, with slightly lower values in the center. A circular stress pattern is visible around the center, caused by the up-and-down motion of the square membrane during dynamic response.

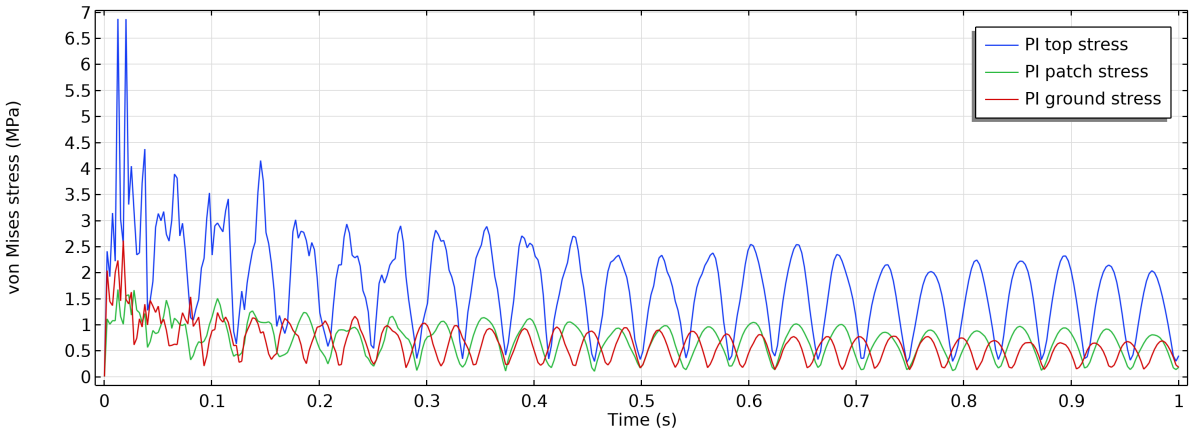

Figure 5.35: Maximum observed PI stresses over time with additional support

Lastly there are the stresses observed in the CU layers, as seen in Figure 5.37. First a peak is observed and then it transitions into a regular sinusoidal wave at around 0.5 seconds. However the stress is higher than for the PI, with the maximal stress observed being $20\,\mathrm{MPa}$, again in the patches. In Figure 5.38a the stress distribution is shown for the CU layer of the patches. As seen before the highest stress is observed at the inner corner of the outer patches. However, similar to the PI layer of the patches, higher stress can be seen at the patches close to the additional support. But this is not as high as the inner corner of the outer patches. Lastly in Figure 5.38b the stress distribution can be seen of the CU layer of the ground plane. A similar stress distribution is observed for both the CU as for the PI layer. However, the stress in the middle is in the same magnitude as the edges. This was not the case for the PI layer.

The energy in the system over time for the additional supported panel can be seen in Figure 5.39. It can be observed that the total amount of energy in the system has increased compared to the normal panel. This can be explained by the increase of amount of solid structure in the pane, while having the same angular impact velocity. The general trend in the system is however the same as with the normal supported panel. A rapid decrease in energy is observed till about $0.1\,\mathrm{sec}$. After this a slower energy decline can be observed for the total amount of energy in the system. Low frequency waves with higher frequency fluctuations are observed for the total kinetic energy and total elastic strain energy in the system. Which is the same as was observed for the maximal stress in the frame previously. Again, it is unsure if the amount of Rayleigh damping applied is realistic for the application, this should be addressed in future iterations.

A comparison of the most important results and observations can be seen in Table 5.4. It can be seen that while adding additional support to the panel the magnitude of the maximal stresses remain roughly the same. Only a doubling is stress is observed in the PI layers, but all observed stresses remain well under the yield stress, as is highlighted by the MoS. The maximal displacements for the top and bottom membranes decreased significantly with the addition of support in the panel, but the frequency of the response increases with the same factor. While the mass almost doubled per panel, the moment of inertia only increased by around 15% when applying additional support. It was found by trail and error that the maximum angular impact velocity needs to be lower or equal to $6\,^\circ/\mathrm{sec}$ in order for the membranes not to impact each other in the case if no support is added to the panel. Based on this the spring constant can be calculated, given any moment of inertia, and the spring can be sized accordingly.

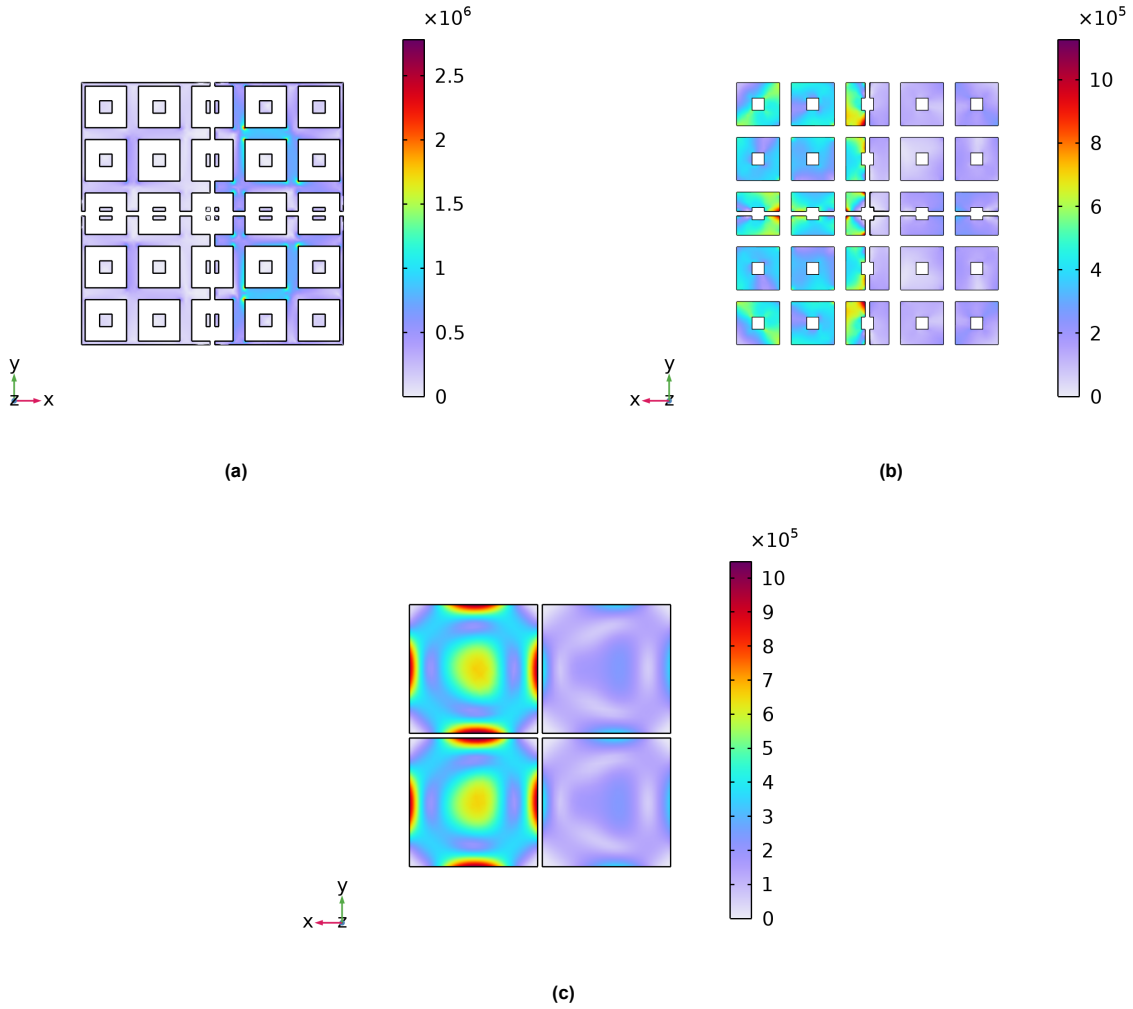

Figure 5.36: Stress distributions in polyimide components at t=0.4962 seconds with additional support: (a) top sheet, (b) patch layer, and (c) ground plane layer.

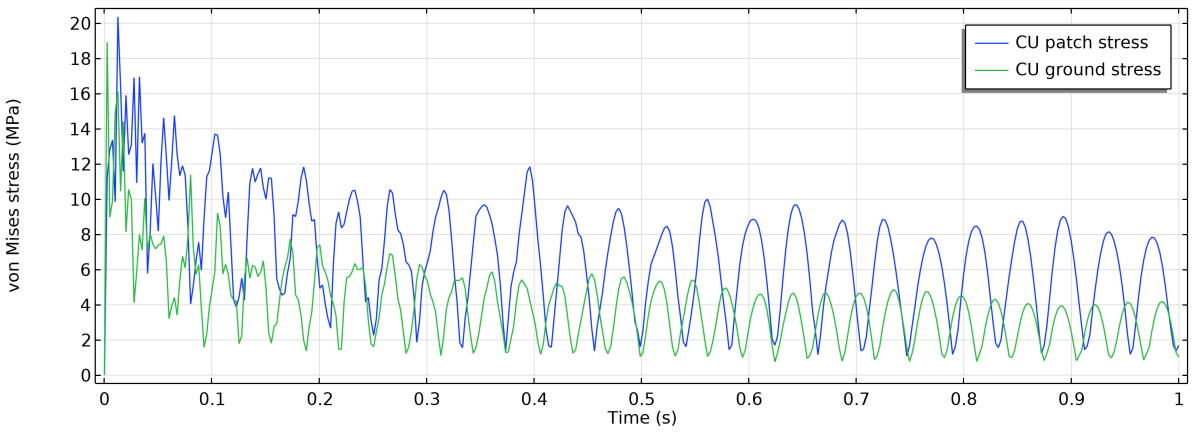

Figure 5.37: Maximum observed CU stresses over time with additional support

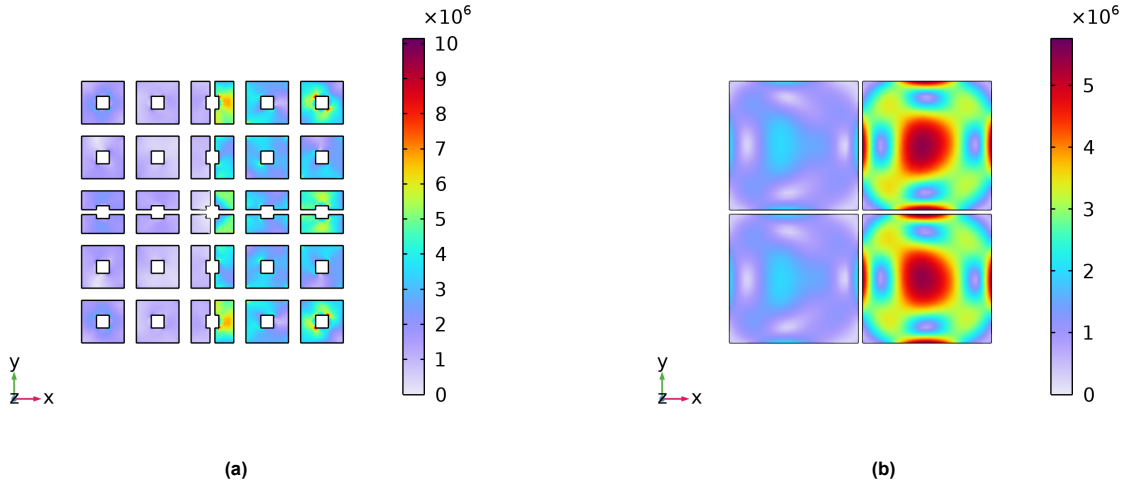

Figure 5.38: Stress distributions in CU components at t=0.4962 seconds with additional support: (a) patches, (b) ground plane layer.

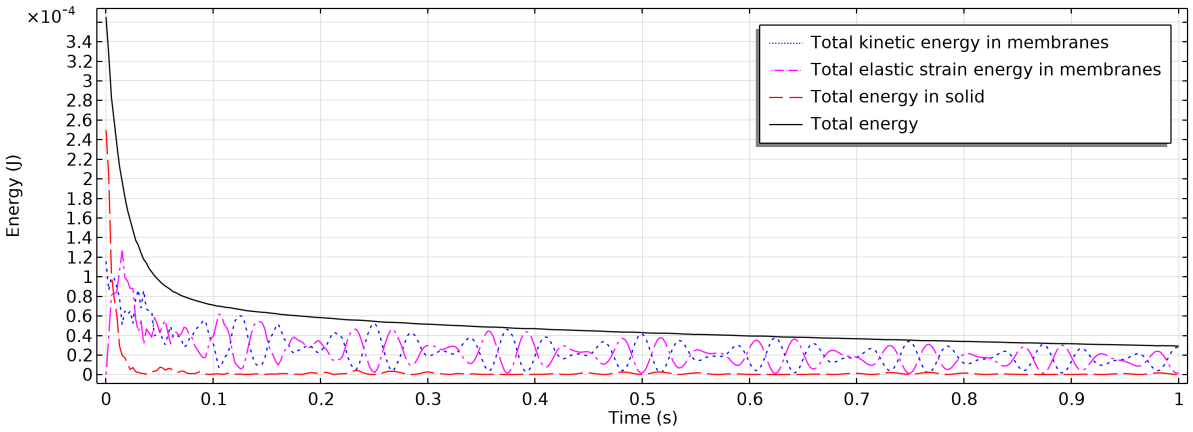

Figure 5.39: Energy in the system over time with additional support

Table 5.4: Summary of deployment results, including key performance metrics and observations.

Parameter	Normal	Additional support	Percentage difference [%]
PI σ_{max} [MPa]	3.4	7	105.0
AL σ_{max} [MPa]	8.5	7.5	-11.8
CU σ_{max} [MPa]	18	20	11.1
PI MoS [-]	30	29.3	-2.3
AL MoS [-]	27.4	31.1	13.5
CU MoS [-]	2.8	2.4	-14.3
Top max displacement [mm]	12	4	-66.7
Bottom max displacement [mm]	8.7	3	-65.5
Top frequency [Hz]	3	12	300.0
Bottom frequency [Hz]	4	16	300.0
I_{YY} [kg m^{-2}]	0.000223	0.000257	15.25
Mass [kg]	0.035952	0.052857	47.11

Chapter 6

Conclusions

This chapter will draw conclusions on the results. In Section 6.1 the conclusions from the concepts and trade-off are presented. Section 6.2 then gives the conclusions for the orbital temperature studies including the reference case as all of the parametric studies. In Section 6.3 the conclusions for the thermo-elastics are presented and in Section 6.4 gives the conclusions drawn from the deployment part of the thesis. Lastly, in Section 6.6 the main research question is answered as a final conclusion of the thesis work.

6.1 Trade-off

From the performed trade-offs, several conclusions can be drawn. First, due to the large size of the reflectarray (RA), a significant large distance is required between the feed and the RA. This necessitates the deployment of either the feed, the RA, or both, away from the satellite. Based on the given requirements, potential satellite placements have been proposed, taking into account the influence of the placing of the satellite and the supports. Eight positional concepts were evaluated with the use of a trade-off, of which only three advanced to the deployment trade-off phase. All three concepts positioned the satellite close to the RA surface, requiring a longer feed deployment. For the deployment trade-off, six deployment options for the RA have been determined from the literature study. These include: A flasher, Panels, Miura-ori, Inflatable, Pully/Tensegrity, and LADeR.

Among all the evaluated parameters (including, Product feasibility, Satellite constraints, Complexity and Antenna performance), Antenna performance was the most heavily weighted category, accounting for approximately 35% of the total. This caused Panels to perform very well on the trade-off. However, if satellite constraints were prioritized more heavily than antenna performance, the LADeR design would have emerged as the top choice. This highlights that the optimal design depends on the specific focus and priorities of the RA. Ultimately, Concept A with Panels scored highest and was used throughout the remainder of the thesis.

6.2 Coatings

Multiple conclusions can be drawn from the performed orbital studies. First of all, it has been observed that the top membrane ,including the patches, always have a higher temperature than the bottom membrane and the frame. The studied orbit consist of three phases. The first phase is where the sun illuminates the top side, the second where it illuminates the side, and lastly it illuminates the bottom side. Throughout the orbit the parts of the panel follow the same trend in temperature. Relevantly low temperature variations of around $2\,^{\circ}\mathrm{C}$ have been observed in each part of the structure except for the top membrane near the edges connecting it to the frame. There, high temperature variations have been observed of more than $50\,^{\circ}\mathrm{C}$. It was also observed that at any point during the orbit, the panel had a temperature below $0\,^{\circ}\mathrm{C}$.

In addition to temperature trends, the effect of relevant parameters for the temperature distribution in orbit were analysed. With varying the absorptivity on the panel for each surface it was found that the side of the panel does not influence the temperature of panel. Increasing absorptivity on other parts of the panel resulted in an increase everywhere on the panel of more then $20\,^{\circ}\mathrm{C}$. However this is only in a specific part of the orbit.

It was found while varying the emissivity of all of the surfaces that some surfaces have a high impact on the temperature of the entire panel and some only a low impact. Specifically the outward facing side of the bottom membrane has a high impact. However, also all inward-facing membrane surfaces had a medium impact on panel temperature. For all of the other faces in the panel low or no impact was observed while varying the emissivity.

Changing the conductivity of the polyimide (PI) layer in the top membrane resulted in a medium impact on the panel temperature. By having a higher conductivity the temperature of the top part decreased and in the bottom increased. This also resulted in a more equal temperature variation in the top membrane. Changing the materials in other parts of the panel resulted in low or no change in the temperature distribution. No temperature change was observed with an increase of thickness of the PI layers in the membrane or the frame. This can be accounted for the low change in thickness variation.

Varying the angle of the panel in orbit between the allowable angles of -11.5 to 6.2° indicated temperature variations compared to the angle of 0° of less than $\pm\ 20\,^{\circ}\mathrm{C}$ for both the top and bottom part of the panel. It can thus be concluded that orientation of the panel has a low impact on the temperature. If high accuracy is required for the allowable temperature in the frame, orbital angle can become an issue, otherwise this should not be expected.

Increasing the size of the panel resulted in a change in temperature less then $5\,^{\circ}\mathrm{C}$. Putting the panels in an array with thermal connection between the panels, simulating hinges, gave no change in the temperatures for the different panels. This is due to the already observed limited influence of changing the emissivity and absorptivity of the sides of the frame.

6.3 Thermo-elastics

For a global temperature increase of $5\,^{\circ}\mathrm{C}$ three out of four requirements are satisfied. These three are Ar-004 (surface accuracy), Ar-006 (maximal displacement of panel) and Ar-007 (yield stress). However, Ar-005 is violated, meaning that the membranes get too close to each other to work properly according to this requirement. This is mainly due to the bottom membrane displacing upwards due to the temperature increase. Since one of the requirements is already violated at an temperature increase of $5\,^{\circ}\mathrm{C}$, this indicates that TE is the most critical aspect of the design, as it can be expected to heat up even more during its lifetime.

6.4 Deployment

In order to increase deployment reliability, a sequential deployment sequence is proposed. This consist of one spine and several ribs. The spine connects the ribs to the satellite and a rib consists of a row of panels with patches on them. Only the deployment of one panel on a rib was analysed since these happen the most often during this kind of deployment. Phase one of deployment (activation of the spring) causes no issues with stresses far from the yield strength of the materials. For phase three (the dynamic response after stopping) several issues were reported. First of all, the membranes are very likely to touch each other in this phase. This might be allowed, but would ideally be avoided to prevent any unforeseen damage to the membranes. This can be partially negated by introducing additional support, but the proposed support is not deemed enough. Applying pre-tension to the membranes could be a potential solution for this problem as well.

During phase three, the first component that is likeliest to fail is the CU patches on the top membrane. This is due to the material's combination of a low yield stress and a high Young's modulus, which makes it more susceptible to failure under stress. If the PI layer fails, it is most likely to occur at the corners of the patches on the top sheet, where stress concentrations are higher. However, the observed stresses

in the PI remain well below its yield stress. The frame is the least likely to fail, as it experiences the lowest stress levels and has the highest yield stress among the components.

6.5 Other Conclusions

The materials used in the current panels consists of: PI and CU for the membranes and aluminum for the frame. All used materials have good resistance against atomic oxygen. The metals have good resistance against UV radiation. The PI does not, but can be protected with a coating. Meaning with one coating the temperature can be better regulated but everything underneath can be better protected as well against the space environment. It is however impossible to protect the reflectarray against MMOD.

6.6 Main Research Question

Returning to the main research question:

Is it possible to design a deployment mechanism for a two membrane reflectarray antenna that still satisfies the mission requirements?

The research conducted in this thesis indicates that such a design is indeed feasible. Reflectarray antennas offer several advantages over traditional parabolic reflectors, including improved volume efficiency and significantly reduced mass. While the flat, deployable configuration allows for better packing within a launch vehicle, the overall volume remains however substantial and must be carefully managed.

Thermal analysis revealed that uncoated panels experience cold temperatures reaching lower than $-100\,^{\circ}\mathrm{C}$. The application of thermal coatings was shown to potentially mitigate this issue effectively. The surfaces with the highest impact have been identified to apply coatings to and quantify the change. Additionally, membrane deformation due to temperature fluctuations poses a challenge. Not primarily in terms of surface accuracy, but in maintaining consistent spacing between the two layers. Another found issue includes the deformation of the membranes during the spring deployed panels. The springs are too strong relative to the mass they deploy, resulting in the membrane impacting each other. Both of these options could be solved by applying structural supports between the membranes of the right materials, or pre-tensioning the membranes.

In conclusion, the findings support the feasibility of a deployable two-membrane reflectarray antenna that meets mission requirements, provided that the identified challenges are addressed through further design iterations.

Chapter 7

Recommendations for future work

This chapter provides recommendations for future work based on the findings and insights gained throughout this thesis. The recommendations are grouped by topic for clarity and relevance. In Section 7.1, suggestions are made for exploring new design concepts. Section 7.2 offers recommendations for further thermal studies. Recommendations based on the thermo-elastic analysis are presented in Section 7.3, while Section 7.4 focuses on deployment-related improvements. Additional recommendations that do not fall under the previous categories are discussed in Section 7.5. Finally, Section 7.6 highlights the recommendations that should be prioritized first in future research.

7.1 Trade-off

Future studies could investigate alternative RA configurations. One such an idea involves splitting the RA into two equal parts, each with its own feed. This may simplify deployment by reducing RA size but introduces additional system complexity due to a second feed and new stability requirements.

Another concept, involves the use of a Cassegrain design configuration, commonly seen in parabolic reflectors. In such configuration, the feed remains fixed to the satellite, minimizing positional disturbances. However, this approach requires precise tuning between the main RA and the sub-reflector also a RA.

7.2 Coatings

This work showed that altering emissivity significantly affects thermal distribution across the membranes. Future work should therefore focus on applying high-emissivity coatings on the inside and low-emissivity coatings on the bottom membrane surfaces to increase temperatures to above $0\,^{\circ}\mathrm{C}$.

Applying coatings has advantages, since the temperature can be altered by increasing or decreasing the emissivity and absorptivity. There are however also some drawbacks, including an increase of weight and having weak electrical conductivity links between the patches for example. Since coatings could potentially be needed on the top membrane it is important to quantify the effect of an electrical conductive link between patches. It is currently unknown what the effect is on the performance of the RA if such a electrical conductive link is present.

Beyond coatings, Multi-Layer Insulation (MLI) should be considered as an alternative thermal control strategy on the bottom membrane. MLI could further reduce emissivity or the reduce the impact of solar illumination, but it is vulnerable to mechanical damage during deployment.

Finally, future thermal models should incorporate non-uniform patch sizes, which would produce more realistic temperature distributions across the panel, since the final RA will also not consist out of the uniformly sized patches.

7.3 Thermo-elastics

Thermo-elastic effects were found to be critical for system performance, and further work should address the observed requirement violation under a relatively small temperature increase. Potential solutions include adding additional support to prevent displacement or applying pre-tension to decrease the magnitude of displacement. Future work should look into other software tools than COMSOL, given the encountered issues of no convergent solutions beyond $5\,^{\circ}\mathrm{C}$ temperature increase. It is recommended to look into more realistic temperature distributions for the panel as it encounters these during its lifetime.

7.4 Deployment

Future studies should extend simulations to include all three phases of deployment into one simulation. This gives better understanding of the entire deployment and eliminates artificial induced stresses as were observed in the beginning of phase 3 simulations. A more detailed investigation of Rayleigh damping factors would also help producing more predictions of dynamic response.

Since torsional springs appear too strong for the extreme lightweight panels, alternative deployment mechanisms such as tape springs should be considered. If however torsional springs remain under consideration, additional support is most likely required to prevent any membrane self induced damage. Furthermore, the dynamics of multiple panels deploying simultaneously within a rib, as well as the behaviour of panel boxes deploying in the spine, should be analysed.

7.5 Other Recommendations for Future Work

Besides the RA in orbit, also the RA stowed during the rocket launch should be investigated in the future, considering the mass and size of the panels. Both the vibrations during launch as well as the launch forces should be addressed in the future. Due to the large size of the reflectarray, it could potentially serve as a drag sail on the satellite. By simply rotating into the right direction the satellite can get more drag and deorbiting can happen much quicker.

The panel itself also needs to be worked out in more detail in the future. How to connect the membranes to the panel should be addressed, as well as a more detailed hinge between the panels and manufacturing.

Lastly mechanical simulations should be combined with RF simulations. This will give more insight into potential problems or give more precise values for the current requirements. It is highly recommended to combine these aspects as this will shape the rest of the design choices on the structural side.

7.6 Priority Recommendations

Based on all the recommendations the following recommendations should be prioritized in the near future.

- Mechanical and RF coupling should be combined to get better understanding of allowable deformations.
- Increase range of temperatures used in thermo-elastics and investigate mitigation strategies for requirement violation.
- Create data base/code to quickly evaluate the sizes of patches based on position taking into account all relevant effects.
- Analyse deployment options other then springs.
- Multiple panel deployment simulations with FEM and panel box deployment analysis.

References

[1] H.-G. Kim, D.-G. Kim, R.-H. Do, K.-R. Koo, and Y.-J. Yu, "Development of deployable reflector antenna for the sar-satellite: Part 1. design and analysis of the main reflector using honeycomb sandwich composite structure," *Applied Sciences*, vol. 14, no. 4, 2024. DOI: 10.3390/app14041590. [Online]. Available: https://www.mdpi.com/2076-3417/14/4/1590.

[2] D. Berry, R. Malech, and W. Kennedy, "The reflectarray antenna," *IEEE Transactions on Antennas and Propagation*, vol. 11, no. 6, pp. 645–651, 1963. DOI: 10.1109/TAP.1963.1138112.

[3] U. of Central Florida. "Deployable reflectarray antennas for space applications." (2017), [Online]. Available: https://www.ece.ucf.edu/deployable-reflectarray-antennas-for-space-applications/. Accessed: 4-Aug-2025.

[4] E. S. Agency. "Smart design of flat reflectarray satellite antennas." (Jul. 2020), [Online]. Available: https://www.esa.int/Enabling_Support/Space_Engineering_Technology/Smart_design_of_flat_reflectarray_satellite_antennas. Accessed: 20-Aug-2024.

[5] NASA. "Integrated solar array and reflectarray antenna (isara)." (Sep. 2023), [Online]. Available: https://www.nasa.gov/smallspacecraft/isara/. Accessed: 26-Aug-2025.

[6] C. Stefopoulos, A. Garufo, R. J. Bolt, C. Trampuz, and S. Monni, *Membrane reflectarray for microsat applications*, ESA Workshop 2024, 2024. [Online]. Available: https://repository.tno.nl/SingleDoc?find=UID%2032a81d24-4751-43e0-854a-ec32aaf6e5ed.

[7] A. Chepala, V. Fusco, U. Naeem, and A. McKernan, "Uniform linear antenna array beamsteering based on phase-locked loops," *Electronics*, vol. 12, no. 4, 2023, ISSN: 2079-9292. DOI: 10.3390/electronics12040780. [Online]. Available: https://www.mdpi.com/2079-9292/12/4/780.

[8] C. Balanis, *Antenna Theory*, 4th. Hoboken, NJ: Wiley, 2016, ISBN: 978-1-118-64206-1.

[9] P. Nayeri, F. Yang, and A. Elsherbeni, *Reflectarray Antennas: Theory, Designs, and Applications*. Hoboken, NJ: John Wiley & Sons, 2018, ISBN: 978-1-118-84676-6.

[10] M. Zawadzki and J. Huang, "Integrated rf antenna and solar array for spacecraft application," in *Proceedings 2000 IEEE International Conference on Phased Array Systems and Technology (Cat. No.00TH8510)*, 2000, pp. 239–242. DOI: 10.1109/PAST.2000.858948.

[11] R. E. Hodges, D. J. Hoppe, M. J. Radway, and N. E. Chahat, "Novel deployable reflectarray antennas for cubesat communications," in *2015 IEEE MTT-S International Microwave Symposium*, 2015, pp. 1–4. DOI: 10.1109/MWSYM.2015.7167153.

[12] R. E. Hodges, N. Chahat, D. J. Hoppe, and J. D. Vacchione, "A deployable high-gain antenna bound for mars: Developing a new folded-panel reflectarray for the first cubesat mission to mars," *IEEE Antennas and Propagation Magazine*, Feb. 2017. DOI: 10.1109/MAP.2017.2655561.

[13] NASA/JPL-Caltech. "Marco being tested in sunlight." (Mar. 2018), [Online]. Available: https://www.jpl.nasa.gov/images/pia22317-marco-being-tested-in-sunlight/. Accessed: 26-Aug-2025.

[14] M.-J. Li, M. Li, Y.-F. Liu, X.-Y. Geng, and Y.-Y. Li, "A review on the development of spaceborne membrane antennas," *Space: Science and Technology*, vol. 2022, Mar. 2022. DOI: 10.34133/2022/9803603.

[15] R. L. USA. "Darpa r3d2 press kit." (Mar. 2019), [Online]. Available: https://rocketlabcorp.com/. Accessed: 26-Aug-2025.

[16] M. Cooley, B. Yon, D. Konapelsky, *et al.*, “Rf design and development of a deployable membrane reflectarray antenna for space,” in *2019 IEEE International Symposium on Phased Array System and Technology (PAST)*, 2019, pp. 1–4. DOI: 10.1109/PAST43306.2019.9020871.

[17] NASA. “Swot: Surface water and ocean topography press kit.” (Nov. 2022), [Online]. Available: https://swot.jpl.nasa.gov/internal_resources/638/swot-press-kit.pdf. Accessed: 26-Aug-2025.

[18] E. Peral, D. Esteban-Fernández, E. Rodríguez, *et al.*, “Karin, the ka-band radar interferometer of the swot mission: Design and in-flight performance,” *IEEE Transactions on Geoscience and Remote Sensing*, vol. 62, pp. 1–27, 2024. DOI: 10.1109/TGRS.2024.3405343.

[19] ESA. “M-argo.” (Nov. 2019), [Online]. Available: https://www.esa.int/ESA_Multimedia/Images/2019/11/M-Argo. Accessed: 26-Aug-2025.

[20] ASI. “M-argo program.” (Jun. 2020), [Online]. Available: https://www.asi.it/en/technologies-and-engineering/micro-and-nanosatellites/esa-gstp-fly-program/m-argo/. Accessed: 26-Aug-2025.

[21] GomSpace. “Esa and gomspace sign contract for continuation of the gomx-5 mission.” (Feb. 2020), [Online]. Available: https://gomspace.com/news/esa-and-gomspace-sign-contract-for-continuati.aspx. Accessed: 26-Aug-2025.

[22] S. Pellegrino and J. F. Vincent, “How to fold a membrane,” in *Deployable Structures*, Cambridge, UK and Reading, UK: Springer, 2002, ch. 4.

[23] S. Magleby, S. Zirbel, R. Lang, *et al.*, “Accommodating thickness in origami-based deployable arrays,” *Journal of Mechanical Design*, vol. 135, Nov. 2013. DOI: 10.1115/1.4025372.

[24] Y. Tsuda, O. Mori, R. Funase, *et al.*, “Flight status of ikaros deep space solar sail demonstrator,” *Acta Astronautica*, vol. 69, no. 9, pp. 833–840, 2011, ISSN: 0094-5765. DOI: https://doi.org/10.1016/j.actaastro.2011.06.005. [Online]. Available: https://www.sciencedirect.com/science/article/pii/S0094576511001822.

[25] S. Georgakopoulos, C. Zekios, A.-S. Kaddour, *et al.*, “Origami antennas,” *IEEE Open Journal of Antennas and Propagation*, vol. PP, pp. 1–1, Oct. 2021. DOI: 10.1109/OJAP.2021.3121102.

[26] N. Chahat, M. Arya, J. Sauder, E. Thiel, M. Zhou, and T. Cwik, “One meter reflectarray antenna: Omera,” in *CubeSat Antenna Design*. Hoboken, New Jersey: John Wiley & Sons, Inc., 2021, pp. 139–162. DOI: 10.1002/9781119692720.ch4.

[27] A. Russo, B. Barakali, K. I. Kitsu, L. Baudet, J. Yang, and Y. Zhong, “Origami-inspired self-deployable reflectarray antenna,” *Acta Astronautica*, vol. 213, pp. 240–251, 2023, ISSN: 0094-5765. DOI: https://doi.org/10.1016/j.actaastro.2023.08.007. [Online]. Available: https://www.sciencedirect.com/science/article/pii/S0094576523004058.

[28] A. J. Rubio, A.-S. Kaddour, C. Ynchausti, S. Magleby, L. L. Howell, and S. V. Georgakopoulos, “A foldable reflectarray on a hexagonal twist origami structure,” *IEEE Open Journal of Antennas and Propagation*, vol. 2, pp. 1108–1119, 2021. DOI: 10.1109/OJAP.2021.3127312.

[29] A.-S. Kaddour, C. A. Velez, and S. V. Georgakopoulos, “A deployable and reconfigurable origami reflectarray based on the miura-ori pattern,” in *2020 IEEE International Symposium on Antennas and Propagation and North American Radio Science Meeting*, 2020, pp. 91–92. DOI: 10.1109/IEEECONF35879.2020.9329994.

[30] A. J. Rubio, A.-S. Kaddour, H. Pruett, S. Magleby, L. L. Howell, and S. V. Georgakopoulos, “A deployable volume-efficient miura-ori reflectarray antenna for small satellite applications,” *IEEE Access*, vol. 11, pp. 119 313–119 329, 2023. DOI: 10.1109/ACCESS.2023.3327057.

[31] H. T. Pruett, N. M. Coleman, and S. P. Magleby, “Preliminary concepts for magnetic actuation and stabilization of origami-based space arrays,” in *Utah Space Grant Consortium Conference*, Space Dynamics Laboratory, Auditorium Rm B, May 2022. [Online]. Available: https://digitalcommons.usu.edu/spacegrant/2022/all2022/8.

[32] N. Miguélez-Gómez, J. M. Parkhurst, K. Pepin, *et al.*, “Thickness-accommodation in x-band origami-based reflectarray antenna for small satellites applications,” in *2020 IEEE International Conference on Wireless for Space and Extreme Environments (WiSEE)*, 2020, pp. 54–59. DOI: 10.1109/WiSEE44079.2020.9262670.

[33] N. Chahat, J. Sauder, R. Hodges, M. Thomson, Y. R. Samii, and E. Peral, “Ka-band high-gain mesh deployable reflector antenna enabling the first radar in a cubesat: Raincube,” in *2016 10th European Conference on Antennas and Propagation (EuCAP)*, 2016, pp. 1–4. DOI: 10.1109/EuCAP.2016.7481692.

[34] N. Chahat, J. Sauder, M. Mitchell, N. Beidleman, and G. Freebury, “One-meter deployable mesh reflector for deep space network telecommunication at x- and ka-band,” in *2019 13th European Conference on Antennas and Propagation (EuCAP)*, 2019, pp. 1–4.

[35] T. LLC. “Products.” (2025), [Online]. Available: https://www.tendeg.com/products. Accessed: 23-Jan-2025.

[36] J. Huang, “The development of inflatable array antennas,” *IEEE Antennas and Propagation Magazine*, vol. 43, no. 4, pp. 44–50, 2001. DOI: 10.1109/74.951558.

[37] Z.-Q. Liu, H. Qiu, X. Li, and S.-L. Yang, “Review of large spacecraft deployable membrane antenna structures,” *Chinese Journal of Mechanical Engineering*, vol. 30, no. 6, pp. 1447–1459, Nov. 2017, ISSN: 2192-8258. DOI: 10.1007/s10033-017-0198-x. [Online]. Available: https://doi.org/10.1007/s10033-017-0198-x.

[38] P. K. Kelly, “A scalable deployable high gain antenna - dahgr,” in *Proceedings of the Small Satellite Conference*, Logan, Utah, USA, Aug. 2016. [Online]. Available: https://digitalcommons.usu.edu/smallsat/2016/TS7Communication/6/.

[39] M. Arya, J. Sauder, and R. E. Hodges, “Large-area deployable reflectarray antenna for cubesats,” in *Proceedings of the AIAA Scitech 2019 Forum*, San Diego, CA, USA, Jan. 2019. [Online]. Available: https://digitalcommons.usu.edu/smallsat/2016/TS7Communication/6/.

[40] A.-S. Kaddour, C. A. Velez, M. Hamza, *et al.*, “A foldable and reconfigurable monolithic reflectarray for space applications,” *IEEE Access*, vol. 8, pp. 219 355–219 366, 2020. DOI: 10.1109/ACCESS.2020.3042949.

[41] A. J. Rubio, A.-S. Kaddour, and S. V. Georgakopoulos, “A mechanically rollable reflectarray with beam-scanning capabilities,” *IEEE Open Journal of Antennas and Propagation*, vol. 3, pp. 1180–1190, 2022. DOI: 10.1109/OJAP.2022.3214273.

[42] M. Machida, T. Tomura, H. Sakamoto, and T. Fukao, “Stretchable-substrate-impregnated fabric: Deployable reflectarray antennas for cubesats,” *IEEE Access*, vol. PP, pp. 1–1, Jan. 2024. DOI: 10.1109/ACCESS.2024.3392562.

[43] M. Finckenor and K. de Groh, *A researcher’s guide to: Space environmental effects*, A. Rai, Ed., *NASA ISS Program Science Office*, Sep. 2020.

[44] Y. Tang, *Lecture 5: Material degradation in space – uv, ao, and mmod*, 2024, [Powerpoint slides] (TU Delft course code: AE4ASM525).

[45] NASA. “Van allen probes spot impenetrable barrier in space.” (Nov. 2014), [Online]. Available: https://web.archive.org/web/20200306135737/https://www.nasa.gov/content/goddard/van-allen-probes-spot-impenetrable-barrier-in-space. Accessed: 26-Aug-2025.

[46] E. S. Agency. “Earth’s plasmasphere and the van allen belts.” (Sep. 2013), [Online]. Available: https://sci.esa.int/web/cluster/-/52831-earth-plasmasphere-and-the-van-allen-belts. Accessed: 26-Aug-2025.

[47] B. Banks, S. Miller, and K. de Groh, “Low earth orbital atomic oxygen interactions with materials,” *NASA TM-220042213233*, vol. 2, Aug. 2004. DOI: 10.2514/6.2004-5638.

[48] K. Nock, K. Aaron, and D. McKnight, “Removing orbital debris with less risk,” *Journal of Spacecraft and Rockets*, vol. 50, pp. 365–379, Mar. 2013. DOI: 10.2514/1.A32286.

[49] J. Sauder, C. Gebara, N. H. Reddy, and C. J. García-Mora, “A framework for small satellite deployable structures and how to deploy them reliably,” *Communications Engineering*, vol. 3, no. 1, p. 72, May 2024, ISSN: 2731-3395. DOI: 10.1038/s44172-024-00210-7. [Online]. Available: https://doi.org/10.1038/s44172-024-00210-7.

[50] FreeCAD Community. “Freecad: Your own 3d parametric modeler.” (2025), [Online]. Available: https://www.freecad.org/.

[51] ATG Europe, *Introduction to space thermal control*, 2024, [Powerpoint slides] (TU Delft course code: AE4ASM524).

[52] O. M. Slides, *Tu delft opencourseware*, https://ocw.tudelft.nl/wp-content/uploads/AE2104-Orbital-Mechanics-Slides_8.pdf, 2024, [Powerpoint slides] (TU Delft course code: AE2104).

[53] Multiphysics, COMSOL. "COMSOL Multiphysics V6.3." (2024), [Online]. Available: https://www.comsol.com.

[54] Online Metals. "0.002" copper foil 110 annealed - 1200" length." (2025), [Online]. Available: https://www.onlinemetals.com/en/buy/copper/0-002-copper-foil-110-annealed-1200-length/pid/24361. Accessed: 22-Aug-2025.

[55] Aerospace Metals. "Aluminum 6063-t83 technical datasheet." (2023), [Online]. Available: https://www.aerospacemetals.com/wp-content/uploads/2023/06/Aluminum-6063-T83.pdf. Accessed: 22-Aug-2025.

[56] MatWeb, LLC. "Polyimide - summary of properties." (2025), [Online]. Available: https://www.matweb.com/search/DataSheet.aspx?MatGUID=ab35b368ab9c40848f545c35bdf1a672. Accessed: 22-Aug-2025.

[57] R. Hibbeler, *Mechanics of Materials*, 10th. Pearson, 2017, SI Units, ISBN: 978-1-292-17820-2.

[58] R. Hibbeler, *Engineering Mecahnics Dynamics*, 14th. Pearson, 2017, SI Units, ISBN: 978-1-292-08872-3.

[59] Lee Spring. "Torsion springs." (2025), [Online]. Available: https://www.leespring.com/torsion-springs. Accessed: 2025-07-31.

[60] SCIA Engineer. "Harmonic damping type - rayleigh damping." (2025), [Online]. Available: https://help.scia.net/25.0/en/analysis/modal_analysis_and_dynamics_and_seismicity/dynamics_basics/harmonic_damping_rayleigh.htm. Accessed: 31-Jul-2025.

Appendix A

Full trade-off table

Table A.1: Extended trade-off data – Part 1.

				Product feasibility		Spacecraft constraints	
			Trade-off parameters	Manufacturablitiy	Flight heritage	Packing efficiency	Expected mass
				1 = hard to manufacture	1 = no flight heritage	1 = low packing eff	1 = high expected mass
Deployment type	Reflectarray type	Kind of deployment actuation		5 = easy to manufacture	5 = flight heritage	5 = high packing eff	5 = low expected mass
			Weight counts	3	1	5	3
			Weight	10.71%	3.57%	17.86%	10.71%
Configuration A							
Flasher	Solid	Rotation		3	3	3	2.5
Panels	Solid	Springs		5	5	1.5	1
Miura-ori	Solid	Strain energy/motors		4	3	3	3
Inflatable	Membrane	Gas pump		2	3	1	2.5
Pully/tensegrity	Membrane	Motor		2	5	2	1.5
LADeR	Membrane	Motor/BI-STEM		2	3	5	4
Configuration B							
Inflatable	Membrane	Gas pump		1.5	3	1	2.5
Configuration C							
Flasher	Solid	Rotation		3	2	3	3
Panels	Solid	Springs		4.5	4	1.5	1
Miura-ori	Solid	Strain energy/motor		3.5	2	3	3
Inflatable	Membrane	Gas pump		2	2	1	2.5
Pully/tensegrity	Membrane	Motor		2	4	2	1.5
LADeR	Membrane	Motor		2	2	5	5

Table A.2: Extended trade-off data – Part 2.

Complexity			Antenna performance			
Modularity	Interconnectivity	Integration effort	Expected thermal stability	Patch grid intactness	Feed influence	Final weighted score
1 = low modularity	1 = high interconnectivity	1 = high integration effort	1 = low thermal stability	5 = array shape remains very good	5 = no/little influence	
5 = high modularity	5 = low interconnectivity	5 = low integration effort	5 = high thermal stability	1 = array shape is disrupted badly	1 = lot of influence	
3	1	2	5	3	2	
10.71%	3.57%	7.14%	17.86%	10.71%	7.14%	
2	1	2	3	1	4	2.55
5	3	5	4	4	4	3.52
4	1	2	3.5	2	4	3.13
1	3	4	3	5	4	2.63
4	1	2	1	5	4	2.52
3	4	3	2	4	4	3.39
1	3	2	2.5	5	3	2.27
2	1	2	3.5	1	2	2.52
5	3.5	4	4.5	4	2	3.32
4	1.5	1	4	2	2	2.93
2	3	4	3	5	2	2.55
4	1.5	2	1.5	3	2	2.23
2	4	3	2	4	2	3.21

Appendix B

Additional results of thermal parametric studies

In this appendix additional results are given for the thermal parametric studies performed in Section 5.2.

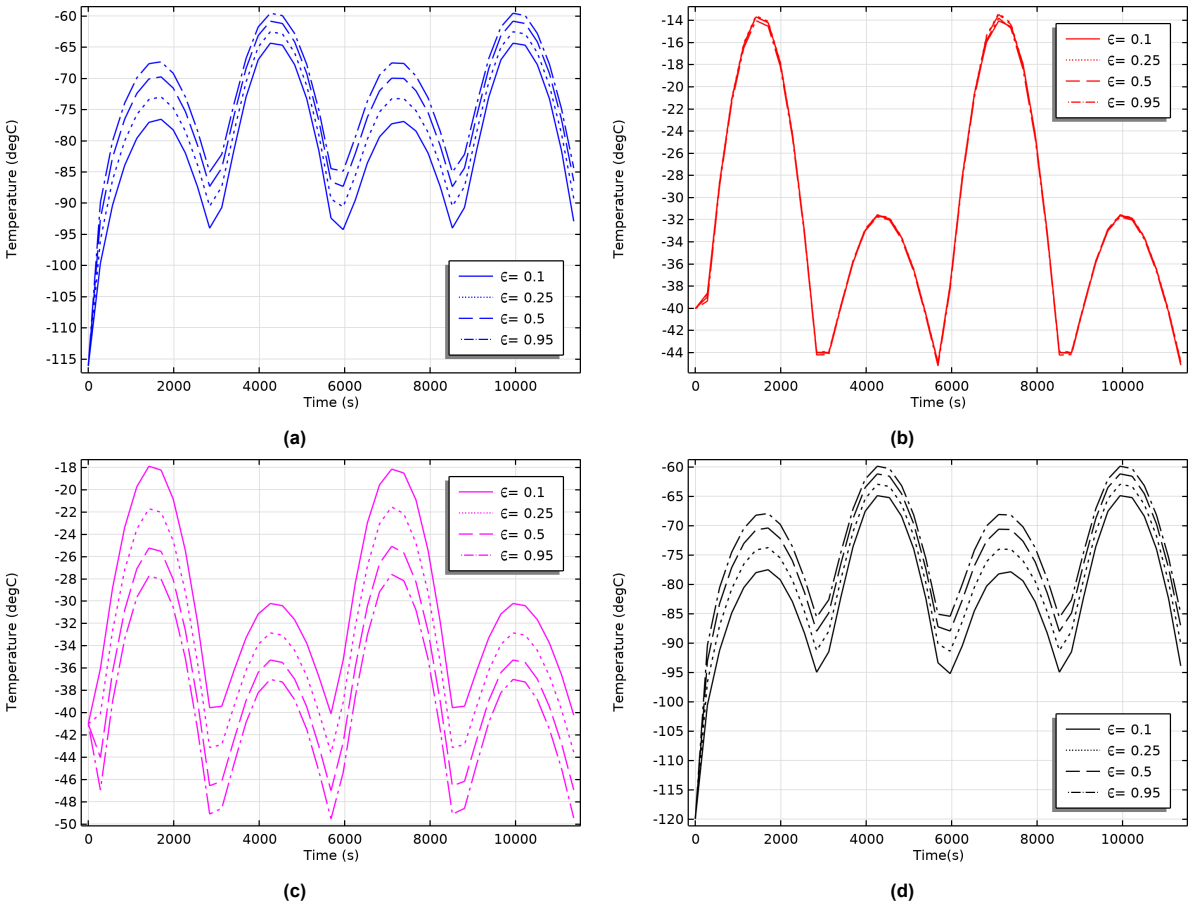

Figure B.1: Simulated impact of altered emissivity of the top membrane on the inside on average temperature distribution across panel components: (a) frame, (b) patches, (c) top membrane, and (d) bottom membrane.

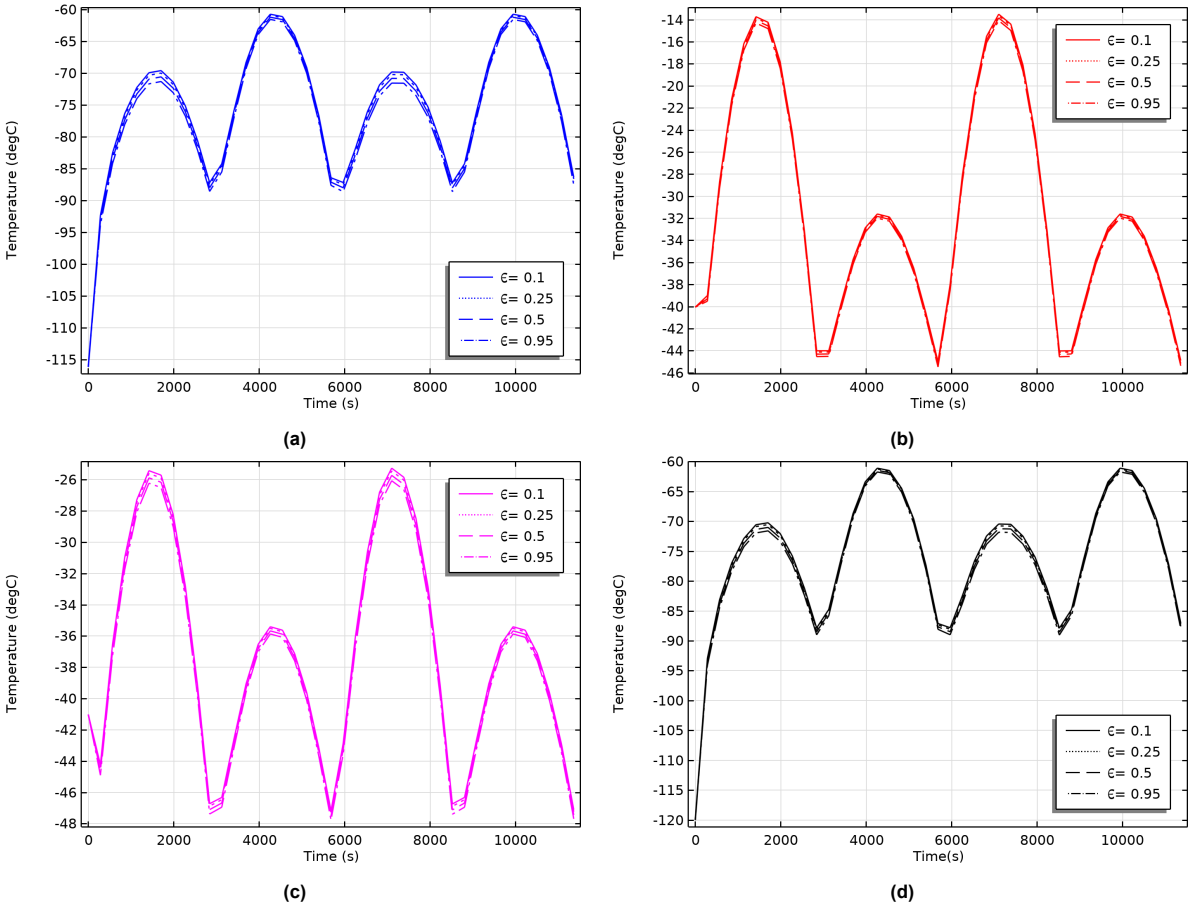

Figure B.2: Simulated impact of altered emissivity on the inside and outside of the frame on average temperature distribution across panel components: (a) frame, (b) patches, (c) top membrane, and (d) bottom membrane.

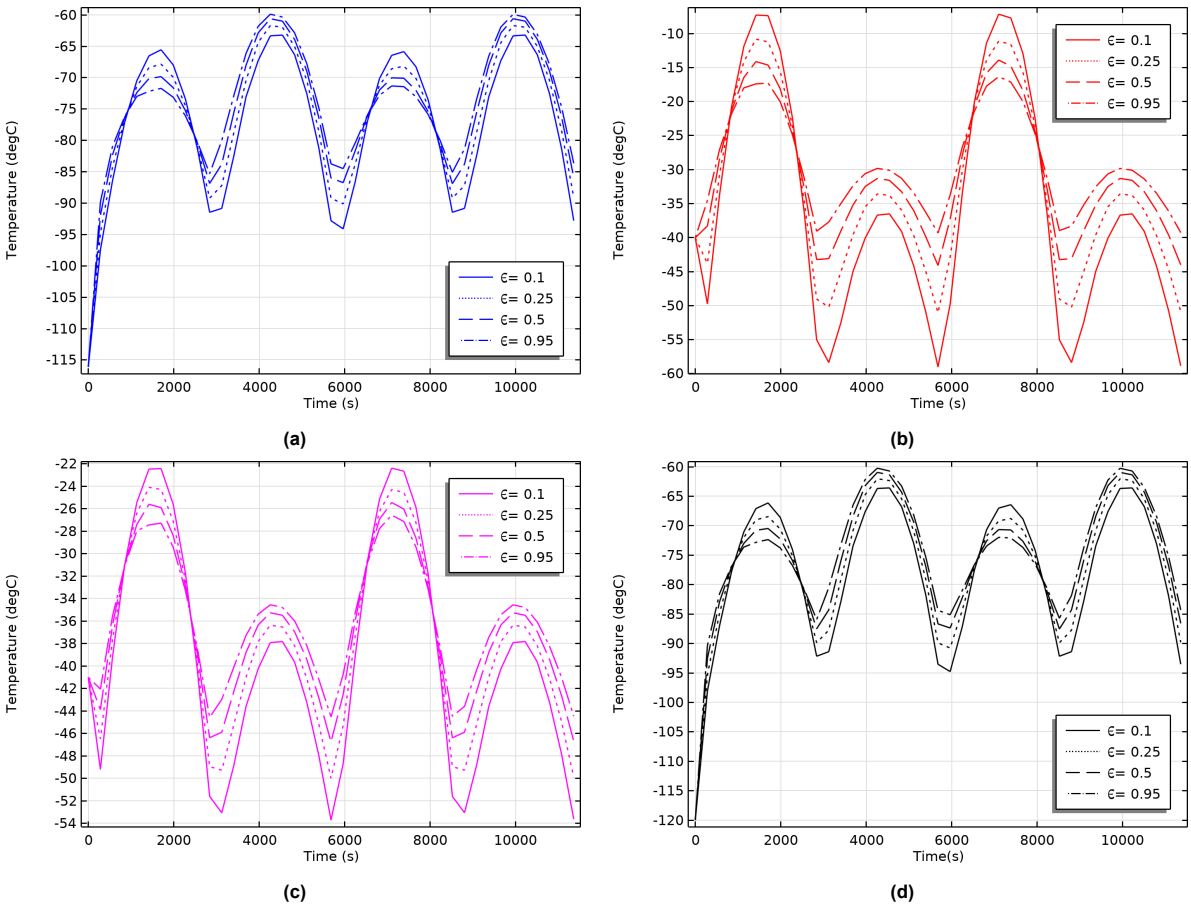

Figure B.3: Simulated impact of altered emissivity on the outside of the patches on average temperature distribution across panel components: (a) frame, (b) patches, (c) top membrane, and (d) bottom membrane.

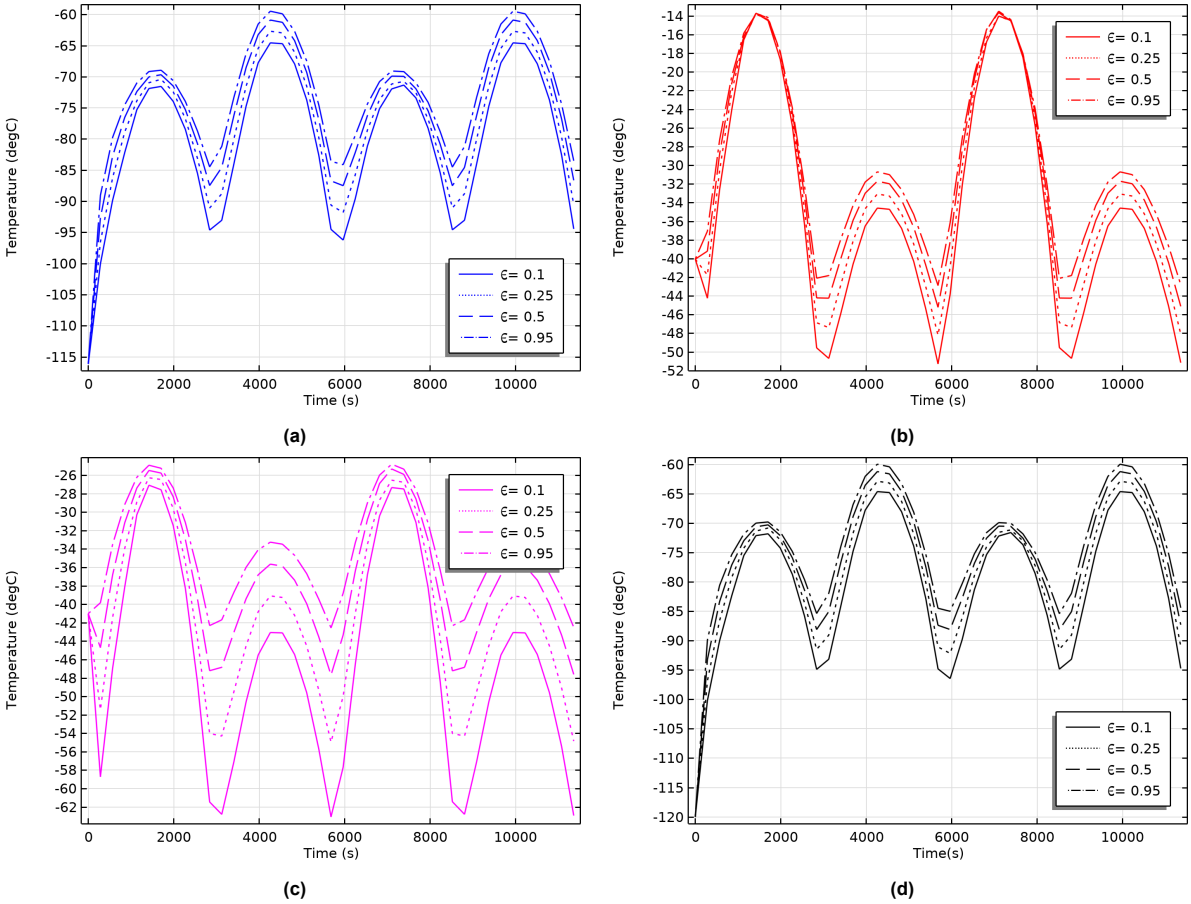

Figure B.4: Simulated impact of altered emissivity on the outside of the top membrane on average temperature distribution across panel components: (a) frame, (b) patches, (c) top membrane, and (d) bottom membrane.

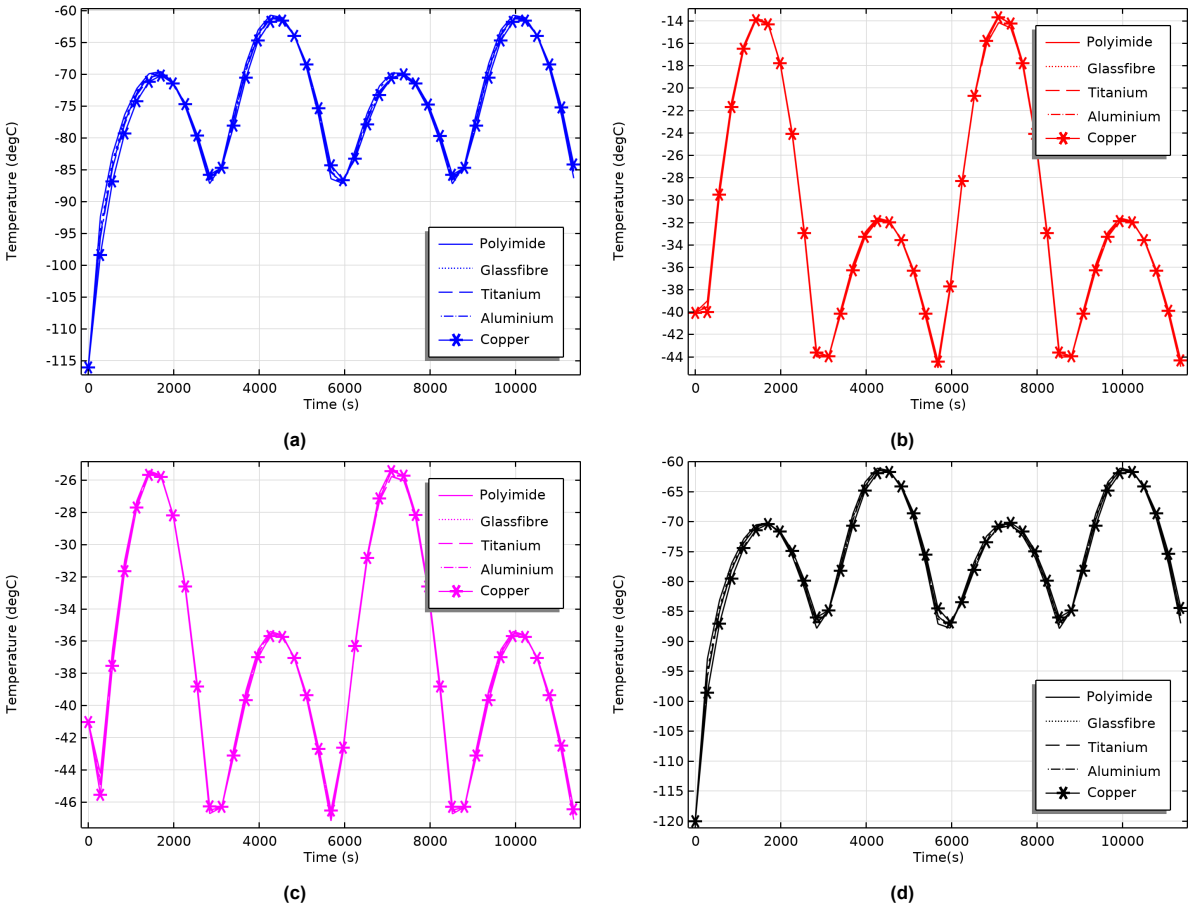

Figure B.5: Simulated impact of altered material conductivity of the bottom membrane on average temperature distribution across panel components: (a) frame, (b) patches, (c) top membrane, and (d) bottom membrane.

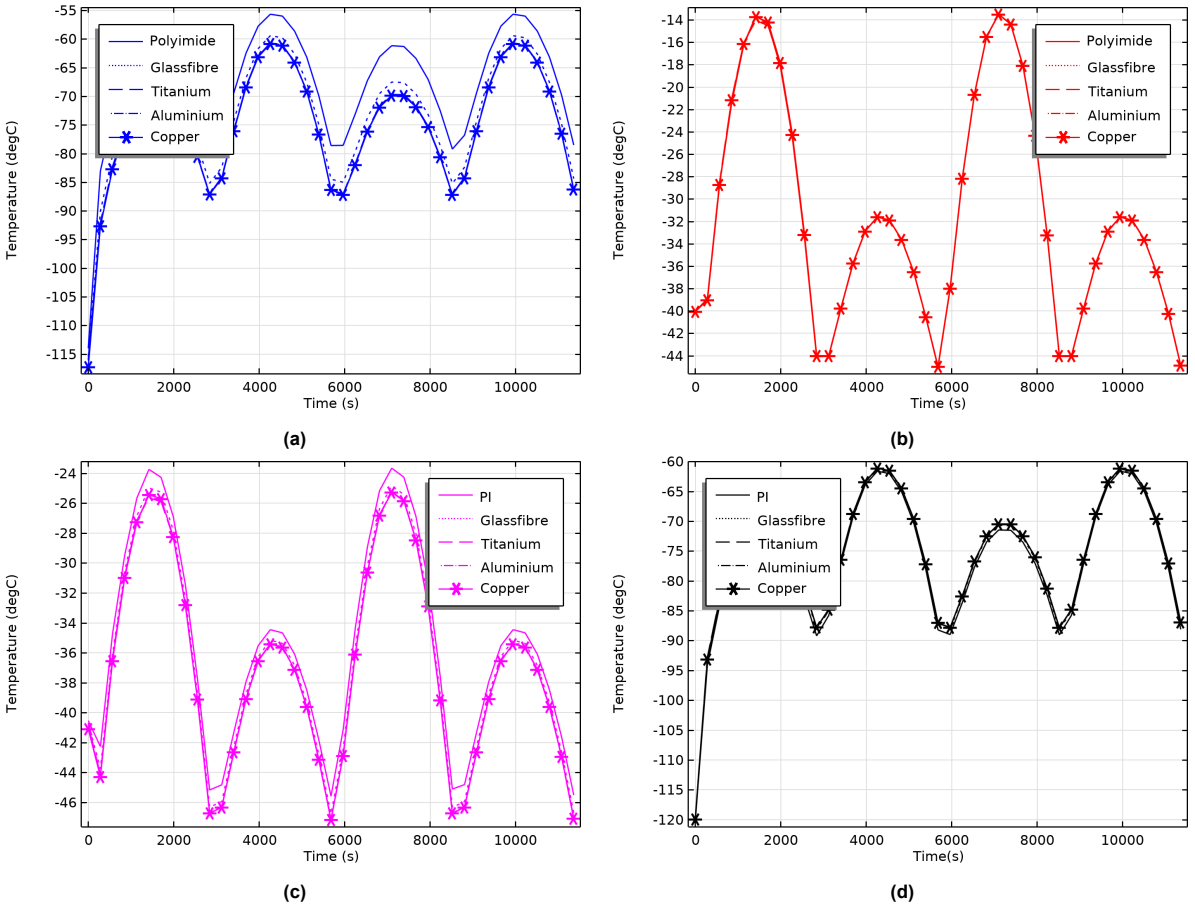

Figure B.6: Simulated impact of altered material conductivity of the frame on average temperature distribution across panel components: (a) frame, (b) patches, (c) top membrane, and (d) bottom membrane.

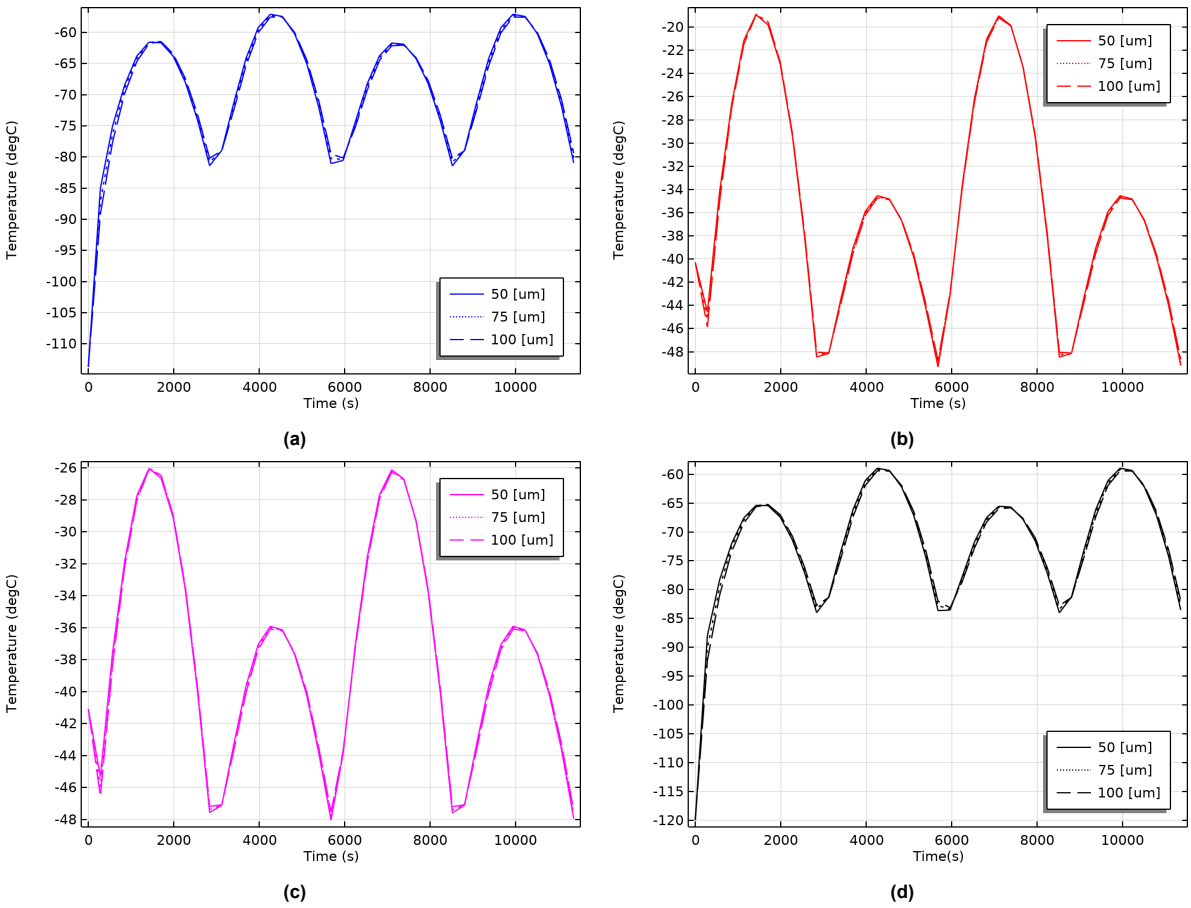

Figure B.7: Simulated impact of altered material thickness of the bottom membrane on average temperature distribution across panel components: (a) frame, (b) patches, (c) top membrane, and (d) bottom membrane.

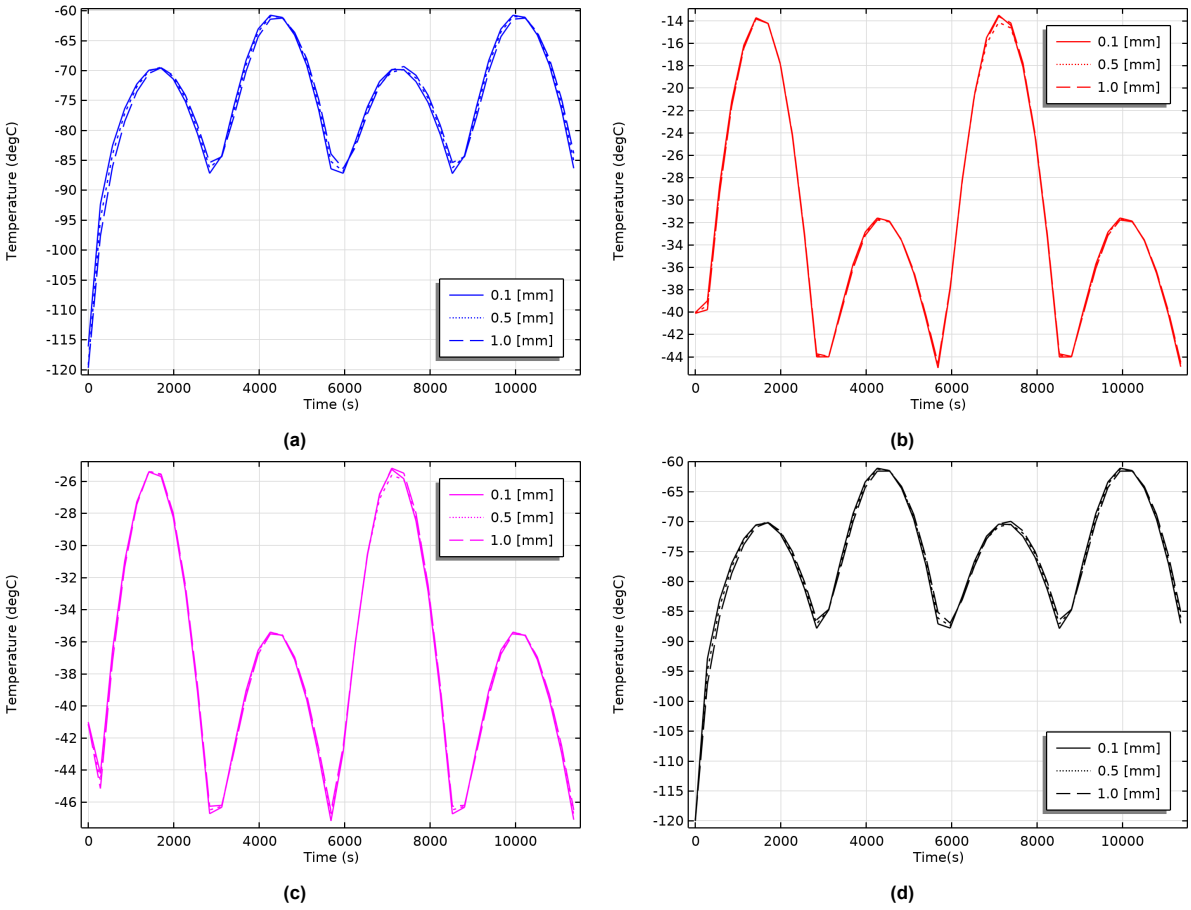

Figure B.8: Simulated impact of altered material thickness of the frame on average temperature distribution across panel components: (a) frame, (b) patches, (c) top membrane, and (d) bottom membrane.

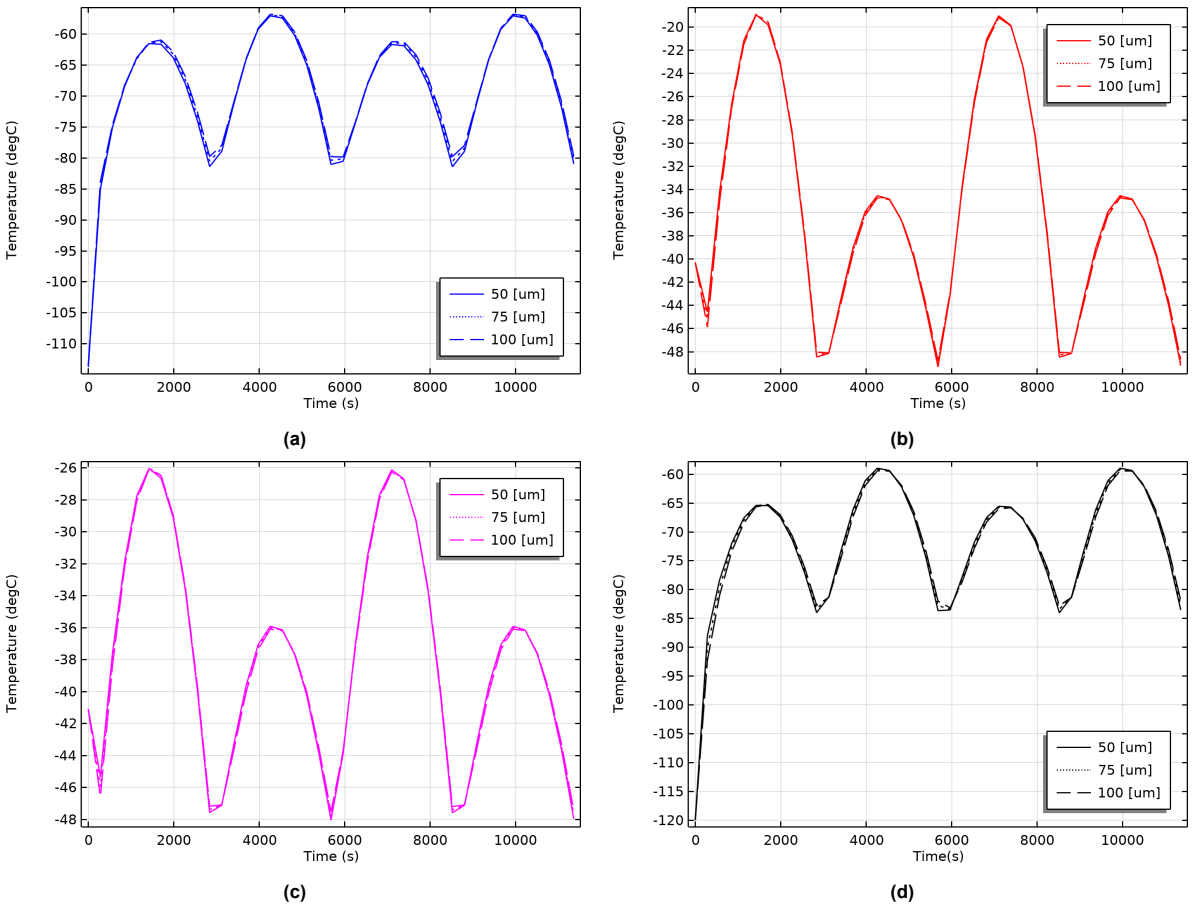

Figure B.9: Simulated impact of altered material thickness of the top membrane including the patches on average temperature distribution across panel components: (a) frame, (b) patches, (c) top membrane, and (d) bottom membrane.

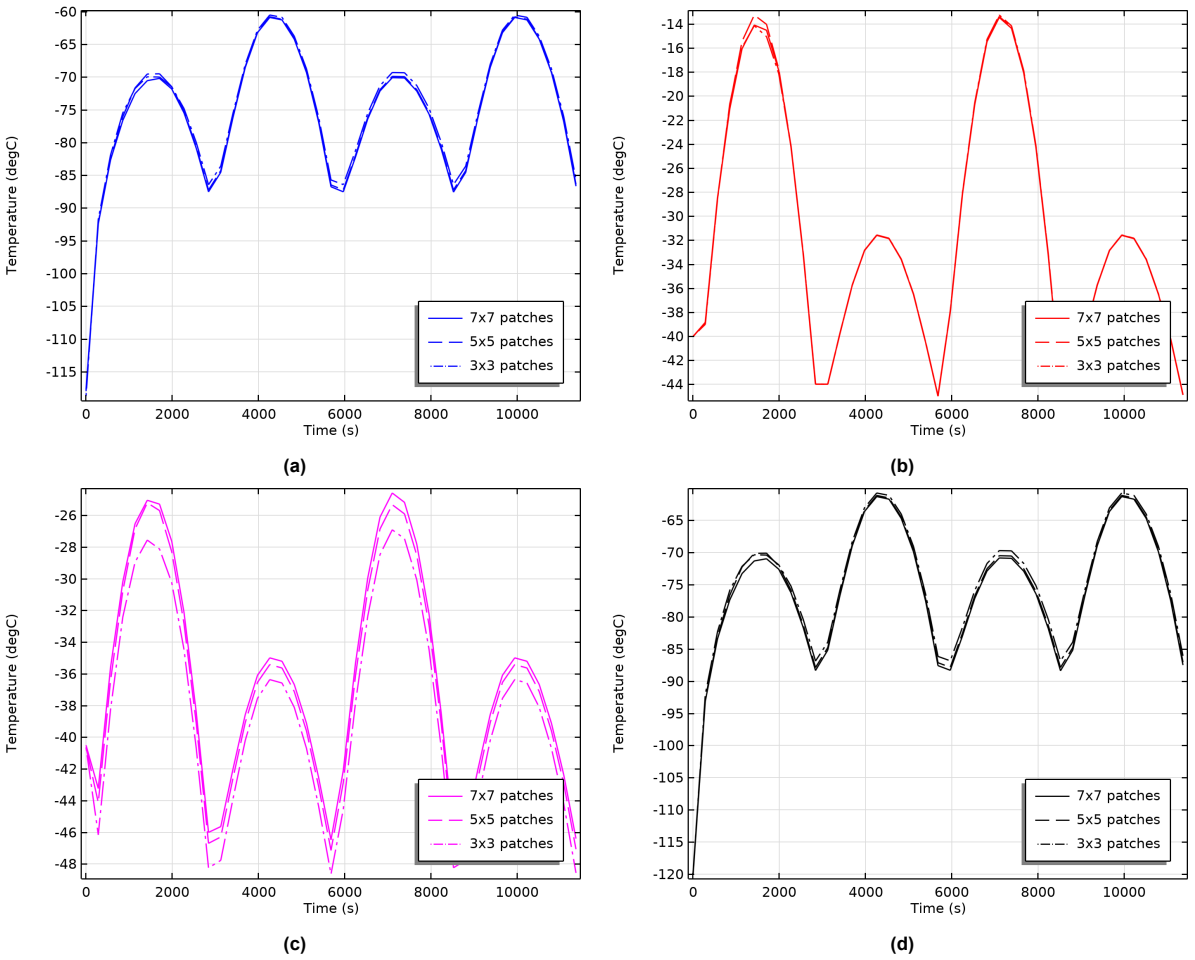

Figure B.10: Simulated impact of altered panel size: (a) frame, (b) patches, (c) top membrane, and (d) bottom membrane.

Appendix C

Results of phase one of deployment

This appendix include the results of phase one of deployment for both the normal supported panel, see Figure C.1 and additional supported panel, see Figure C.2. Both results present the position of the stresses and a zoomed in version. This is done for both the frame as well as the membranes.

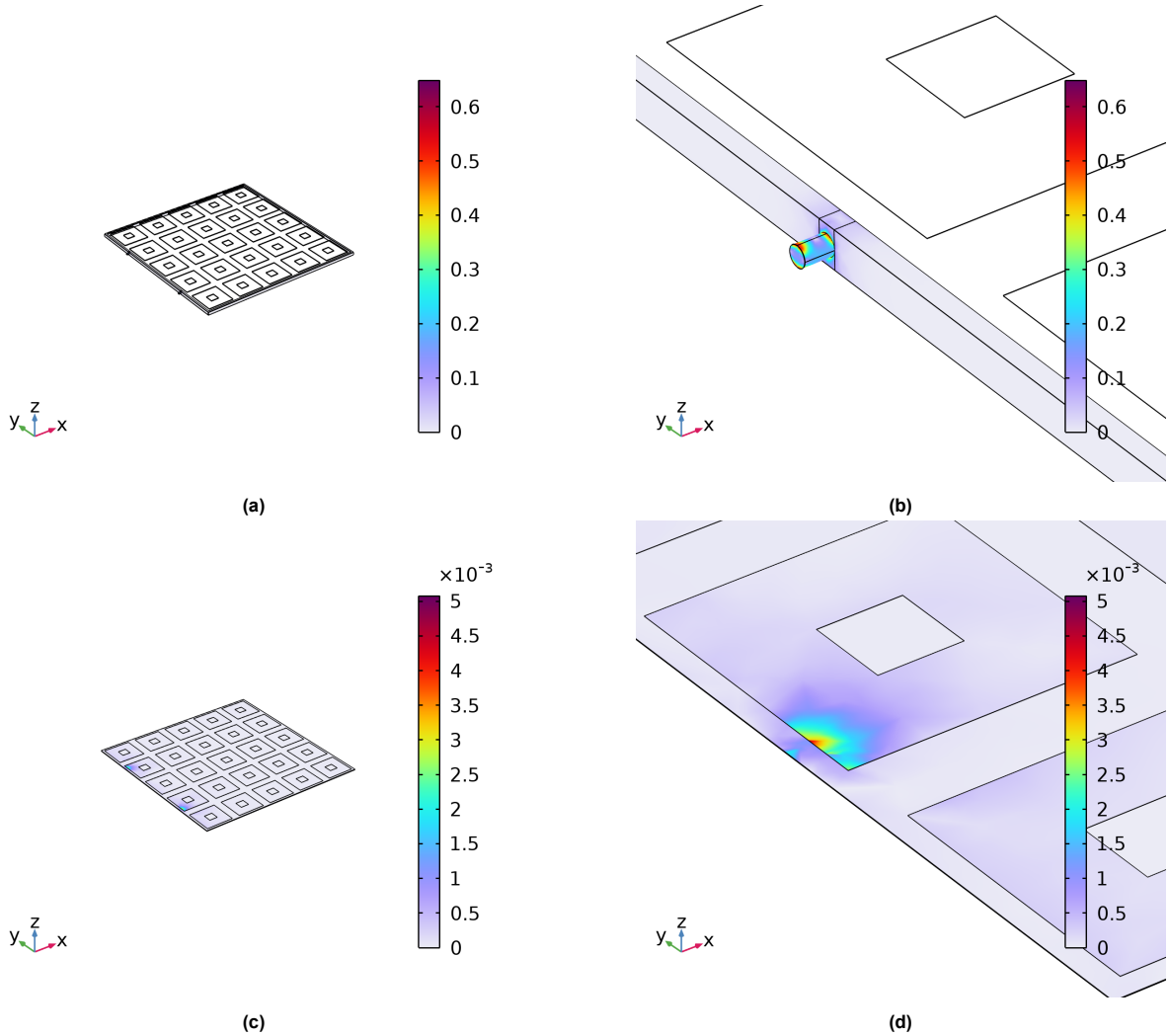

Figure C.1: Start deployment stresses with normal support, stresses are in MPa. (a) observed stresses in solid. (b) zoomed in on relevant part of solid. (c) observed stresses in membranes. (d) zoomed in on relevant part of membrane.

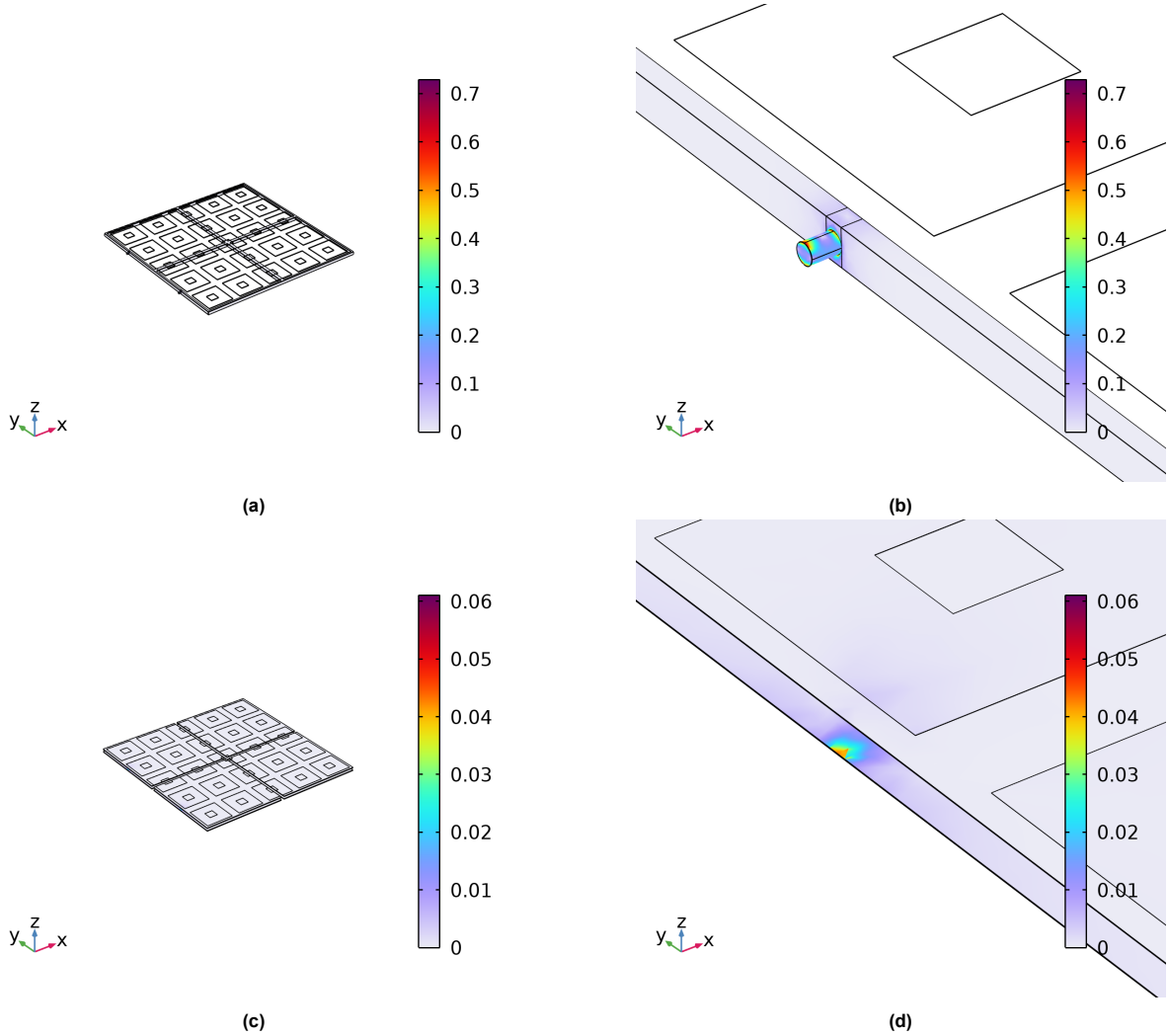

Figure C.2: Start deployment stresses with additional support, stresses are in MPa. (a) observed stresses in solid. (b) zoomed in on relevant part of solid. (c) observed stresses in membranes. (d) zoomed in on relevant part of membrane.